# The DA + dM Eclipsing Binary:
# EC13471-1258

By
**Michael R. Brownstone**
B.Sc. Honours (UCT)

This dissertation is submitted in accordance with the requirement for the

**Degree of Master of Science**

in Astrophysics and Space Science
at the University of Cape Town

in association with the
South African Astronomical Observatory

Supervised by:

**Dr. Darragh O'Donoghue**

and

**Dr. Dave Kilkenny**

April 24, 2008

# Acknowledgement

I wish to extend my sincere gratitude and deepest appreciation to my supervisors Dr. Darragh O'Donoghue for his ideas and direction and from Dr. Dave Kilkenny for his unyielding support and advice.

I am also grateful for the creation of the NASSP[1] program without which I wouldn't have done this study and Prof. Peter Dunsby, the NASSP coordinator, for his advice and encouragement.

I also extend my heartfelt respect and deepest love to my family and friends for their continued support and encouragement throughout my studies.

---

[1] National Astrophysics and Space Science Program, (UCT) Cape Town, RSA.

# Abstract

EC13471-1258 is an eclipsing binary star system. It is composed of a hydrogen-rich DA white dwarf, (WD), and a dMe red dwarf, (RD). With an orbital period of $3^h$ $37^m$, the system is located at a distance of $48 \pm 5$ parsecs.

Having a surface gravity field with log g = 8.34, the WD is on the cool side for its class, with a $T_{eff}$ of $14220^{\circ} \pm 300^{\circ}$ K and a mass and radius of $0.78 \pm 0.04\, M_{\Theta}$ and $0.011 \pm 0.01\, R_{\Theta}$, respectively.

The RD is of spectral type M3.5. It shows chromospheric activity and flaring events which are characteristic of this type of star. With a surface temperature, $T_{eff}$, of $3100^{\circ} \pm 75^{\circ}$ K and a radius of $0.42 \pm 0.02\, R_{\Theta}$, the star is less than half the mass of our Sun, at $0.43 \pm 0.04\, M_{\Theta}$.

At $400 \pm 100$km/sec, the rapid rotation of the WD shows that it is spun up, presumably from accretion during its past. Although there is no observable disc structure, its rapid rotation implies that there was once a viscous disc supported by the transfer of matter from the RD. The system, therefore, can conceivably be considered to be a cataclysmic variable for which mass-transfer has either ceased or reduced to a trickle.

The separation distance between the WD and the RD is $\sim 10^6$ km. At only 2½ times the distance between Earth and Moon and with a size of half the radius of our Sun, from the perspective of the hemisphere of the WD facing the RD, the RD would occupy most of the 'sky'. With mass ejections, occasional flaring observed, a stellar wind and other chromospheric activity, the region of the WD Roche lobe is filled with matter injected by the RD, adding an element of randomness or variability to the emission patterns. This is supported by observation.

New spectroscopic observations have yielded trailed spectral emission plots in $H\alpha$ with greater detail. These confirm the chromospheric activity of the RD and further indicate the presence of emission within the WD Roche lobe region. The semi-amplitude of the observed emission motion has been found to be < 300km/sec.

There is further evidence provided for the existence of intervening gas within the WD Roche lobe region. This could be responsible for the obscuration or reduction of emission intensity levels, and could account for the lack of corroborating evidence for observed emission from multiple orbital phase angles.

A model of the mass-transfer stream in the absence of a disk shows that there are a number of areas within the WD Roche lobe where mass-transfer in the trajectory path would intersect itself. This is where one would expect collision and associated emission and the search for signs of this emission is the approach taken in this thesis.

# Table of Contents

Chapter One: General Characteristics of a Cataclysmic Variable Star System

Chapter Two: What we know about EC13471-1258

Chapter Three: Data Acquisition, Reduction and the Production of Higher Resolution Trailed Spectral Plots

## Chapter Four: Modeling the Mass-Transfer Stream Trajectory

## Chapter Five: Motion in the Frame of the Binary

## Chapter Six: Motion in the Frame of the Observer

## Chapter Seven: Interpretation of the Data

## Chapter Eight: Uncertainties and Error

## Chapter Nine: Conclusion

# Introduction

Binary star systems represent a large and diverse class of astronomical objects. These star systems are found in many combinations and evolutionary stages.

Most binaries revolve in wide orbits, with little or no interaction between the stars. As one moves to shorter orbital periods binary systems can interact via tidal forces and other effects such as angular momentum/mass exchange, irradiation or stellar winds.

In the closest binaries, the stars begin to fill their Roche lobes (section 1.1), allowing for the direct exchange of matter through Roche lobe overflow. If both stars fill their Roche lobes they share a common envelope but if only one of the stars fills its Roche lobe then mass-transfer can proceed from donor to recipient and this type of binary system is termed ‘semi-detached’.

Subclasses of semi-detached binary star systems range in type depending on the nature of the compact object: From white dwarfs to neutron star systems to black holes such as in “micro-quasars”.

In this study we look at a binary closely related to the subclass of semi-detached binary star systems comprising a white dwarf (WD) and a late type red dwarf (RD). This type of system is called a cataclysmic variable (CV) star.

The standard model for the formation and evolution of CVs was devised some decades ago (see Warner 1995; Rappaport et al. 1983; King 1988; Spruit & Ritter 1983) and is briefly described in the first chapter. Although not the focus of this thesis, more recent modifications to the Standard Model have been suggested (Sills et al. 2000; Pinsonneault et al. 2002; Schenker & King 2002; Andronov et al. 2003; Taam et al. 2003) in an attempt to address some of the inconsistencies between the predictions of the standard model and observation. These include the discrepancy between the calculated and the observed minimum orbital period, (see sec. 1.4), the prediction of a higher than observed population density of CV systems at the orbital minimum and the distribution of orbital periods (Kolb & Biraffe 1999), angular momentum loss rates (Andronov et al. 2003), as well as estimates of binary ages (Schenker & King 2002).

In this investigation we study a binary named EC13471-1258. The first study of the system (O’Donoghue et al. 2003) showed it to be a hydrogen-rich DA WD and a dM RD eclipsing binary. A very small amount of mass transfer into the Roche lobe of the WD seemed to be occurring. The amount was so small as to be difficult to detect. This is in contrast to the situation in more typical cataclysmic variables where the accretion light swamps that of the component stars. The system thus offers the potential to study in unusual detail a binary very closely related to cataclysmic variables.

We further investigate the nature of the mass-transfer by studying the velocity components of the H$\alpha$ Doppler shifted emission line as a tracer. We then model the mass-transfer trajectory in an attempt to explain the observed emission.

# Chapter One

# General Characteristics of a Cataclysmic Variable Star System

Cataclysmic variable stars generally comprise a WD and some type of late K or M dwarf, the RD. These are interacting binaries in that tidal forces play a significant role in the evolution and stability of the system, and, generally there is mass transfer taking place directly between the two stars. These systems have a short binary orbital period ranging from just over an hour to as much as twelve hours, for the longest binary systems (Hellier 2001, sec. 4.3.1).

CVs are classified based on their observational characteristics (Warner 1995, sec. 2.1), and include Classical Nova (CN), Dwarf Nova (DN), Recurrent Nova (RN), and Nova-like (NL) sub-types, although there is considerable overlap. Strong Magnetic CVs are mostly NL type but are classified according to the strength of the magnetic field of the primary, the more massive star of the pair. The strength of the field has a critical effect on disc formation and accretion flow. Polars have the strongest fields and Intermediate Polars (IP) show intermediate strength fields with characteristics common to both polars and non-magnetic CVs.

## 1.1 The Pre-Cataclysmic Evolution of Binaries

CVs begin as wide binaries separated by a few hundred solar radii (Hellier 2001, sec. 4.1). The more massive star, which is destined to become the WD, evolves faster than the other star of the binary pair. On an evolutionary timescale, the star leaves the main sequence and becomes a red giant.

As the red giant is more massive and evolves on a faster time scale, it expands and fills its 'Roche lobe'. The Roche lobe is a region around the secondary (or primary) whose limit is defined by a contour around the star which represents an equipotential gravitational surface (see Figure 1, p.10). Any matter with enough momentum to cross this surface will no longer be gravitationally bound by the secondary (or primary) and can therefore cross over to the other star ( Hellier 2001, sec. 2.3) or be ejected into space.

Mass transfer begins with a ratio of masses ($q=M_1/M_2$) greater than 1 where the more massive star, the red giant, is $M_1$. This has important implications in the response of the binary to mass transfer described below. As matter is transferred the Roche lobe begins to shrink.

The binary response to mass transfer results in the reduction of the red giant's Roche lobe size as well as the orbital period. In addition, as the red giant is initially closer to the centre-of-mass of the system material transferred to the less massive companion star therefore moves further from the centre-of-mass, resulting in an increase of angular momentum of the material being transferred. Conserving the overall binary angular momentum requires a decrease in the angular momentum of the binary and the binary separation, which further decreases the size of the red giant's Roche lobe (Hellier 2001, sec. 4.1).

The orbital period is, therefore, reduced through the two mechanisms, donor mass loss and binary angular momentum loss. In addition, mass transfer also reduces the Roche lobe size. There is, though, no reduction in the radius, as the radius of a giant does not depend on its total mass, only its degenerate core (Ritter 1976). These combined effects then cause the Roche lobe to overflow, resulting in a feedback loop which produces a runaway situation as the whole envelope of the red giant is transferred onto its companion star, at a rate which is limited only by the speed at which the material can flow.

The companion star is unable to adjust to the arriving mass. Thus as the material fills and overflows the Roche lobe of the primary it grows forming an extended cloud surrounding the two stars. This is the "common envelope" or CE phase in which the pre-cataclysmic variable is effectively orbiting within a red giant envelope. As the binary system is now orbiting within a common envelope of material, the interaction generates viscosity producing a drag on its motion. This drag drains the orbital energy causing the two stars to spiral inwards towards each other reducing their orbital separation and causing heat within the envelope. When this energy exceeds the binding energy, the envelope is ejected and propelled outwards into interstellar space, forming a planetary nebula (Warner 1995, sec. 9.2.1.3).

The binary that emerges as a result of this event is a main sequence secondary, $M_2$, and a hot sub-dwarf primary, $M_1$ (Hellier 2001, sec. 4.1).

### 1.1.1 Evolution into Contact

The system is gravitationally bound, but there is no mass transfer at first as the separation is still too large for such interaction. For cataclysmic variable star systems to be observable there has to be some means of orbital angular momentum loss to reduce the orbital period thereby maintaining mass transfer from the RD to the WD.

Reduction of the orbital period is now governed either by gravitational radiation generated through the orbital cycle, over a timescale of $10^{9-10}$ years, or through "magnetic braking" (Weber & Davis 1967), coupling the field to ionized particles from a stellar wind, over a timescale of $10^7$ to $10^8$ years, for typical systems.

Gravitational Radiation arises from the orbital motion of a binary star which produces a ripple or warping of space, according to General Relativity. This rippling moves radially outwards in the form of a periodic wave (Hellier 2001, sec. 4.2.1). The energy for this 'gravitational radiation' comes at the expense of the binary orbit causing the two stars to move closer to each other.

Alternatively, Magnetic Braking describes a process in which the magnetic field lines of a star couple with the stellar wind or ionized plasma forcing the particles to co-rotate with it. As the particles move off into interstellar space they are accelerated to high speeds from the rotation of the star and the extended magnetic field lines, taking with them substantial angular momentum. This causes a drag on the spin rotation of the star thereby reducing its rotational velocity. Yet, as the secondary is tidally locked to the primary, as described below, the angular momentum loss is at the expense of the binary orbit.

When the two stars become close enough for tidal forces to have effect, the strong gravitational field of the primary acts to distort the shape of the secondary by raising a bulge. This bulge would point to the WD but as the secondary rotates its envelope passes through this bulge. Vicious interaction then causes the tidal bulge to be either lagging or leading depending on whether the period of rotation of the secondary is greater or less than the orbital period. In this manner, the bulge synchronizes the rotation of the secondary with the binary orbit (Zahn 1966; Hut 1981; Warner 1995, sec. 9.1.3).

The small binary separation thus ensures that the secondary is tidally locked to the primary so that the secondary faces the primary throughout the orbital period. Tidal locking further ensures that its spin period is equal to the orbital period. The timescale for synchronous rotation, which depends on the viscosity in the envelope (Warner 1995, sec. 9.1.3), is short compared to the lifetime of a CV.

Above an orbital period of 3 hr the angular momentum loss rate is governed by magnetic braking, ($10^{-9} - 10^{-8} M_{\Theta} / yr$), while periods less than 2 hr, the angular momentum loss rate is generated mainly from gravitational radiation ($10^{-10} M_{\Theta} / yr$ for a 2 hour orbital period), as a result of the higher orbital velocities required to maintain the shorter orbital periods. (Hellier 2001 sec 4.3.2)

As the stars move even closer to one another the larger, the less dense star distorts even further from its spherical geometry due to the strong gravitational pull from the primary. If this attraction towards the primary is greater than its own binding force, material will be transferred between the two stars. The critical point where this happens is at the apex of the Roche lobes, called the Inner Lagrangian Point, $L_1$. This lies at the contact point of the Roche lobes of the two stars and is the path by which material is transferred between the two stars (Hellier 2001, sec. 2.3), see Fig. 1.

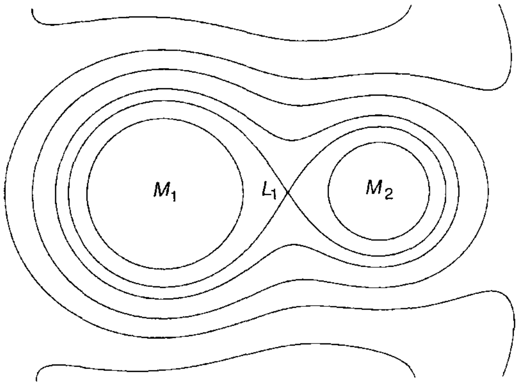

***Figure 1 - Contours of equi-potential surfaces of gravity drawn for a binary system (Adopted from Hellier 2001 p. 20).***

The inner Lagrangian point, ($L_1$), constitutes a region of zero effective gravity, allowing thermal motions to carry the gas from the outer envelope of the secondary star across $L_1$ towards the gravitational potential well of the WD.

### 1.1.2 Stable Mass Transfer

For stable long-lived mass transfer, the secondary star, labeled $M_2$, must fill its Roche lobe, either through reduction of the orbital period from gravitational radiation, magnetic braking, or through the star expanding into its Roche lobe in the course of its evolutionary development (King 1988; e.g. Frank, King & Raine 1992, p.46). It is generally believed that magnetic braking ($P_{orb} > 3^h$) and gravitational radiation ($P_{orb} < 2^h$) are responsible for the mass transfer in the majority of CVs.

## 1.2 The Mass Transfer Stream

Generally speaking, the composition of the transferred mass includes a large amount of hydrogen from the chromosphere of the RD star. Should the chromosphere of the RD fill its Roche Lobe, mass-transfer will ensue through the $L_1$, Lagrangian point, down the potential well to the vicinity of the WD. The mass will have a radial sound speed, from chromospheric pressure, of about 10km/sec through $L_1$ and rotational velocity due to the orbital motion of the system at more than 100km/sec (Hellier 2001, sec. 2.4).

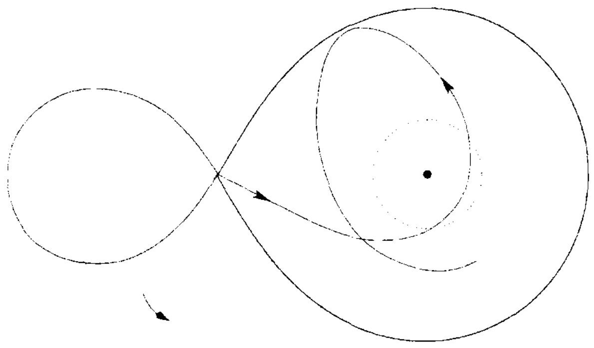

***Figure 2 - Plane view of the trajectory of a gas stream emanating from the secondary star (left). The dotted ring forms the circularization radius. (Adopted from e.g. Hellier 2001)***

The stream then follows a trajectory determined by the injection velocity and gravitational attraction of the primary star. It sweeps past a radius of closest approach, ($R_{min}$), with respect to the WD, looping around to cross its earlier path (Lubow & Shu 1975). See Fig. 2.

A continuous stream following this orbit will therefore intersect itself causing collision and loss of energy. On the other hand, if the stream has had no interaction along its trajectory path, it will maintain the angular momentum it had on leaving the $L_1$ point and it will tend to settle into the orbit of lowest energy for a given angular momentum, i.e. a circular orbit (Hellier 2001, sec. 2.4).

The stream will therefore settle in an orbit at a radius conserving its initial angular momentum at the $L_1$ point, called the circularization radius, ($R_{circ}$), (Hellier 2001, sec. 2.4). The physical radius of the orbit at $R_{circ}$ is determined by the angular momentum that the material had on leaving the $L_1$ region.

## 1.3 The Formation of an Accretion Disc

An accretion disc begins to form from an accumulation of matter at the circularization radius of the primary. The circularization radius is usually 2-3 times smaller than the Roche lobe radius of the primary star (Frank, King & Raine 1992, p.56). The stream of material, therefore, orbits the primary well inside its Roche lobe.

If the radius of the primary star, $R_1$, extends beyond the circularization radius (i.e. if $R_1 > R_{circ}$), matter will accrete directly onto the primary's surface. However, for CVs with a WD, $R_1 << R_{circ}$, and the formation of a disc can proceed given a continuous stream of mass-transfer material.

Within the ring of material orbiting at the circularization radius, material closer to the primary star will orbit faster (Kepler's law) causing friction as they slide past material further out radially (Frank, King & Raine 1992, p.57).

The matter responds to this loss of energy by moving to orbits of smaller radius, or deeper into the gravitational potential of the primary star thereby losing angular momentum. As the inner matter spreads the loss of angular momentum is balanced by a corresponding outward spreading of matter. The mechanism which describes this process, the Balbus-Hawley instability (Hawley et al. 1998), considers matter in differential rotation as being attached to magnetic field lines. The rotation stretches the field lines slowing the inner matter and reducing its angular momentum while speeding up the outer matter thereby increasing its angular momentum. This causes the matter to move outwards to larger radius until it detaches from the field line and settles at a higher angular momentum state. The net effect is to cause the ring to spread out into a thin disc. This process continues spreading the matter until the inner edge meets the WD surface. The matter then accretes onto the surface of the WD and this could lead to either a spin-up or spin-down change to the rotation of the compact star (Wang 1987).

At the outer edge of the disc there are tidal interactions with the secondary star causing the matter and its angular momentum to become assimilated into the orbit of the secondary. This limits the outward spread of the disc (Hellier 2001. sec. 2.4).

Material will continue to flow inwards towards the WD as long as there is angular momentum loss from the disc or if the primary star rotates slowly enough to allow inflow of material instead of expelling it centrifugally (Frank, King & Raine 1992, p.57).

In the case of a magnetized primary, this inner radius of the disk is where the ram pressure of the in-falling gas balances the magnetospheres' pressure. This defines the magnetospheric radius of the WD, $R_{mag}$. If the radius of the magnetosphere, $R_{mag}$, extends beyond the circularization radius, $R_{circ}$, the inner disk annulus will be prevented from forming there and direct impact onto the surface will be limited to matter which can pass through the magnetic net or matter which couples to the magnetic field lines for subsequent accretion on the poles of the WD.

## 1.3.1 The Bright Spot

When a disc has been formed, the stream of material passing through the $L_1$ point from the secondary star impacts upon the outer edge of the disc, forming a "bright spot", (Figure 3). At this spot the stream of material, falling radially towards the WD, encounters material moving almost perpendicular to its circular path in orbit around the WD.

Although the stream is slightly wider than the disc edge the dense core of the stream impacts with the disc and is gradually assimilated into the circular flow (Hellier 2001, sec. 2.4.2). Some of the material flows over the disc continuing onto the original trajectory. The kinetic energy of the stream is converted to heat and radiated away.

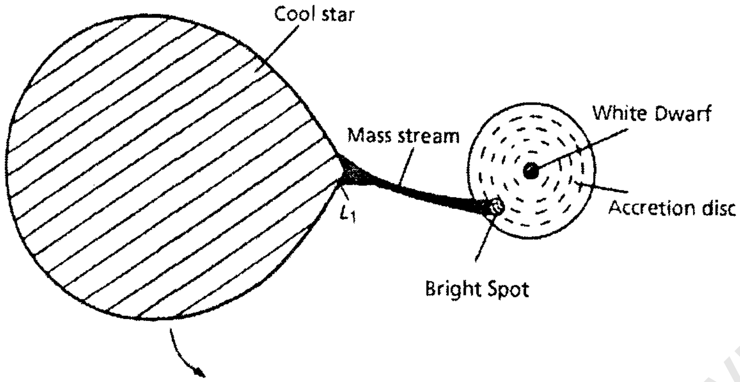

***Figure 3 - Schematic view of a cataclysmic variable star system as viewed from the pole of the orbit (Adopted from e.g. Warner 1995).***

In some CVs the bright spot emits as much as 30% of the total optical emission of the system. This can be observed directly. Known as orbital "humps", these are caused by the additional emission seen when the bright spot is on the side facing the observer where it is not obscured by a disc or other structures within the Roche lobe (Hellier 2001, sec. 2.4.2).

## 1.4 The Orbital Period

*The Minimum Orbital Period* – The Standard Model of CV evolution predicts binary systems with orbital periods as low as 65-70 min (Kolb & Baraffe 1999). Although, there is a minimum observed orbital period for CVs at ~78 min (Hellier 2001, sec. 4.3.3) there are exceptions (Augusteijn et al.1996, Uemura 2004).

At this minimum period, the red dwarf, the secondary, has expelled or transferred much of its mass to the WD primary to such an extent that it ceases to burn hydrogen. The secondary moves out of equilibrium and the attractive gravitational forces overcome the outward radiation pressure causing the star to contract to such an extent as to become degenerate, a state of matter where atoms are no longer supported by pressure but by the quantum mechanical requirement limiting the spacing between atoms (Hellier 2001, sec. 4.3.3). The degenerate secondary would show the characteristics of a hydrogen rich low mass WD (Warner 1995, sec. 9.3.2) whose mass-radius relation would be of the following form;

$$R_2 \cong 8.96\times10^{8}(1+\mathrm{X})^{\frac{5}{3}}M_2^{-\frac{1}{3}}\ \mathrm{cm} \tag{1}$$

where X is the hydrogen fraction, $R_2$ is the radius of the secondary and $M_2$ is the mass of the secondary (Chandrasekhar 1939).

Equation (1) shows the inverse relationship between the radius of the star, $R_2$, and its degenerate mass, $M_2$. Any additional mass loss causes the star to expand. The expansion of the radius in this degenerate secondary from mass loss has the effect of increasing the orbital period which further increases the extent of its Roche lobe.

Transfer of mass from the degenerate secondary will also increase the Roche lobe, $R_{L,2}$, as well as the separation between the two stars, a.

All these combined effects support an overall increase in the orbital period and the system evolves towards longer periods. Eventually, the Roche lobe detaches from the secondary star, causing mass transfer to decline sharply and the star system becomes inconspicuous and therefore rarely found in surveys (Hellier 2001, sec. 4.3.3).

Orbital periods in excess of twelve hours are not common for cataclysmic variable star systems (Hellier 2001, sec. 4.3.1) due to the necessity that the RD secondary be less massive than the WD so as to avoid runaway mass-transfer as described in section 1.1.

### 1.4.1 The Period Gap

There are a much smaller number of non-magnetic binary systems with orbital periods between 2 and 3 hours (called the "period gap") compared to the number found with either longer or shorter orbital periods. It has been postulated (Warner 1995, sec. 9.3.3) that this could be a result of the disruption of the magnetic braking mechanism caused by a temporary loss of equilibrium in the companion star. Possible causes are "disrupted braking" and "cyclic evolution".

Disrupted Braking proposes that the loss of the chromosphere of the secondary due to mass transfer can eventually cause the inner core to respond by changing its internal structure from a deeply convective envelope to total convection through the sudden mixing of He throughout the secondary, thereby causing a rearrangement of the internal magnetic field (Robinson et. al. (1981). The result is a lowered stellar wind and hence reduced magnetic braking. This restructuring also causes the star to contract as well causing the mass-transfer stream to cease. This will persist until equilibrium is established and the secondary comes in contact with its Roche lobe, at around the 2 hour orbital period. Mass transfer then starts once again, at a lower level, and is maintained through gravitational radiation and reduced magnetic braking (Warner 1995, sec. 9.3.3).

Alternatively, it has been shown (Livio and Shara 1987) that the period gap can be explained as a result of 'cyclic evolution', whereby a CV cycles between high mass-transfer of a nova-like (NL), which generally has an orbital period in excess of 3 hours, and a lower mass-transfer state characteristic of dwarf novae (DN), generally under the 2 hour orbital period. This can happen as a result of the irradiation of the secondary through nova outbursts (Hellier 2001, sec. 5.1). These can be powerful enough to cause a temporary increase in mass-transfer rate and consequently the orbital period.

As a result of mass loss this could lead, after the primary has cooled down on a timescale of 50 - 300 years (Livio et al. 1987), to the secondary being unable to refill its Roche lobe, causing the interruption or cessation of mass transfer.

This is consistent with an observed decline in novae emission intensity after outburst (Warner 1995, sec 4.4.2). This decline in the intensity led to a proposal (Shara et al. 1986a) that following a nova eruption a CV may, if unable to repeat the outburst, 'hibernate', with negligible mass-transfer, ($\dot{M}_2$), for thousands of years, as a long period of inactivity takes place. Other examples of hibernating CVs are BPM71214 (Kawka et al. 2003) and HS2237+8154 (Gaensicke et al. 2004).

Observation of the system during hibernation would be difficult as it would have a negligible mass-transfer rate during this period. Magnetic braking would eventually bring the stars close enough for mass-transfer to resume and as the rate of mass transfer slowly increases, the binary response would be to increase the orbital period and the system will move back through the DN region through the period gap and towards the NL region (Kovetz, Prialnik & Shara 1988).

## 1.5 Magnetic fields

Magnetic fields play a vital role in all aspects of star formation and evolution. In CVs they are essential for the formation of the accretion disc by facilitating the exchange of angular momentum through the accretion disc annulus.

The Balbus-Hawley instability describes the magnetic mechanism through which the necessary exchange of angular momentum takes place to produce the disc, (section 1.3). In a sense it is similar to magnetic braking except now the magnetic field lines are on small scales and are stretched from the differential rotation of adjacent annuli within the disc (Hellier 2001, sec. 5.3).

In systems with strong magnetic fields such as AM Her star systems, magnetic fields provide a channel for the transfer of material along field lines to the poles and subsequent accretion thereon (Hellier 2001, sec. 8.3) where supersonic collision near the surface generate observable x-rays.

Strong magnetic fields in the primary can cut-off the inner disc at a radius proportional to the strength of the magnetic field (Intermediate Polars), or if the field is strong enough and extending beyond the circularization radius, can eliminate the possibility of disc formation entirely (Polars -AM Her) (Hellier 2001, sec. 8.3).

# Chapter Two

## What we know about EC13471-1258[1]

### 2.1 Discovery

The discovery of EC13471-1258 came as a result of the Edinburgh-Cape Blue Object Survey (Stobie et al. 1997; Kilkenny et al. 1997). The system has been described in detail by O'Donoghue et al. 2003.

Data for the O'Donoghue et al. (2003) paper were obtained from Hubble Space Telescope for ultraviolet spectroscopy, with the SAAO 0.75 and 1.0 meter telescopes for optical photometry and with the SAAO 1.9 meter telescope for the optical spectroscopic measurements.

### 2.2 The Light Curve and Optical Spectrum

EC13471-1258 is a 16th magnitude star. The light curve below shows that it is an eclipsing binary with an orbital period of 3 hours and 37 minutes.

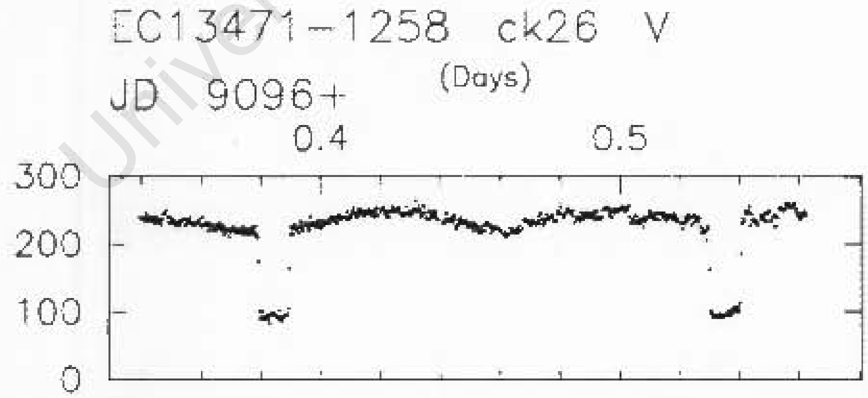

*Figure 4 - V Band Light Curve at 30s Time Resolution: Number Counts vs. Julian Day, showing the orbital period.*
*(Figure reproduced from O'Donoghue et al. 2003).*

---

[1] This chapter is a (précis) survey of the paper, O'Donoghue et al. (2003).

The system lies at an inclination angle, i = 75.5° ± 2°, with total eclipses of the WD lasting 14min reducing the luminosity by 1.5 magnitudes. The time from first to last contact is 944 sec and the duration of totality is 835 sec.

There is no secondary eclipse and its absence indicates that the secondary is much larger than the primary so that when the primary passes "in front" of the secondary it only covers a tiny fraction of the secondary surface. Also apparent is an ellipsoidal modulation. This can be explained as a result of the observer viewing the RD from differing aspects. The normally spherical RD is distorted as a result of the strong tidal forces between the two stars since the material nearest the primary experiences a stronger gravitational attraction towards WD than material at the far side of the star. The modulation shows a decrease in emission from the geometrically un-distorted star i.e., when both stars lie along line of sight. This effect accounts for the dip in the light curve at the midpoint between eclipses in Figure 4.

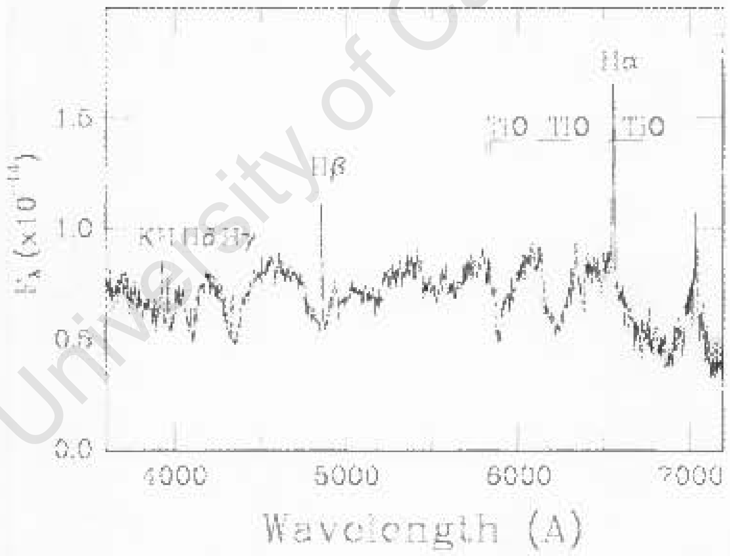

***Figure 5 – Optical Spectrum of EC13471-1258***
***(from O'Donoghue et al. 2003)***

The spectral flux distribution shows comparable contributions from each star. (see Figure 6). In the blue are the broad Balmer absorption lines expected from a WD, yet narrow emission cores. In the red region of the spectrum, the TiO molecular bands found in M stars are clearly visible.

### 2.2.1 Optical Thickness and the Balmer Decrement

The line strength ratios of $H\alpha/H\beta$, $H\gamma/H\beta$, and $H\delta/H\beta$ are 1.4, 0.67, and 0.83 (O'Donoghue et al. 2003) whereas the theoretically calculated ratios in an optically thick environment, (Case B recombination), predicts values of 2.8, 0.47 and 0.29, respectively (Ferland et al. 1982). Comparison of these ratios indicates that the Balmer decrement is flat and the relative fluxes in the Balmer emission lines, (Figure 5), indicate that there might be intervening gas absorbing some signal, in support of the notion that there is substantial hydrogen gas within the Roche lobe of the WD.

### 2.2.2 The Ephemeris

Using the data from the light curves, a linear fit (i.e. assuming a constant period) was used to determine the ephemeris (O'Donoghue et al. 2003).

The parameters are listed in Table 1.

| **Parameter** | **Mid-Eclipse (2440000+)** |
|---|---|
| **Epoch (HJD)** | **8689.64062**<br>**± 0.00001** |
| **Period (d)** | **0.150757525**<br>**± 0.000000001** |

***Table 1: Ephemeris for EC13471-1258***
***(From O'Donoghue et al. 2003)***

The error estimates are based on the accuracy of the eclipse timings of about 1sec and observations over 24000 cycles (O'Donoghue et al. 2003). There were, though, systematic variations of up to 12sec. It has been subsequently shown (Koen 1996) that these variations were due to a random walk in the binary period.

## 2.3 The UV Spectrum and the Parameters of the White Dwarf

O'Donoghue et al. (2003) also obtained HST/STIS observations. The resulting summed spectra are shown in Figure 6.

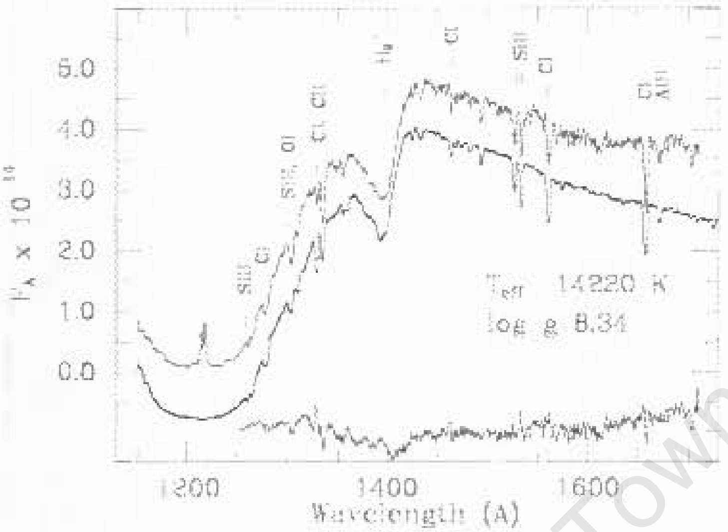

***Figure 6- UV Spectrum and Best-fit Model.***
***Top curve is sum of the Spectra for EC13471-1258. Middle curve is the best model fit. Bottom curve shows the residuals. The lower two curves have been shifted downwards for clarity. The units for the ordinate are in erg $sec^{-1}$-$cm^{-2}$-$Å^{-1}$.***
***(O'Donoghue et al. 2003)***

The UV spectrum in Figure 6 shows very strong $Ly\alpha$ absorption arising in the WD photosphere. In addition, there are narrow metal absorption lines, mostly due to CI and Si II.

The presence of the quasi-molecular $H_2^+$ feature at 1400 Å (Allard & Koester 1992) indicates that the WD is cool, (well under 20000°K), and the virtual absence of the $H_2$ feature at 1600 Å enable the setting of upper and lower bounds to the temperature range. The atmospheric parameters were determined by fitting a synthetic spectrum to the HST data. This provided values of **$T_{eff}$ = 14220°K and log g = 8.34**. (O'Donoghue et al. 2003).

The width of the metal lines indicated that the WD was rotating rapidly. Subsequent investigation, see O'Donoghue et al. (2003), showed that the WD was indeed rotating rapidly with a rotational velocity calculated to be, $V_{rot,1} \sin i = 400 + 100$ km/sec, where, 'i', is the inclination angle between the orbital plane and the line of sight, discussed in section 2.5.1.

HST ultraviolet spectroscopy was further used to measure the radial velocity variations of the WD arising from the binary motion using the quasi-molecular $H_2^+$ feature at 1400 Å with corroborating velocity information coming from the metal absorption lines.

The best fit curve to the velocity data yielded a radial velocity curve with a semi-amplitude of $K_1 \sin i = 138 \pm 10$ km/sec, where $K_1$ is the orbital semi-amplitude of the

WD. When compared to the model template, (middle curve in Figure 6), the model gave a $\gamma_1$-velocity of 61 +/-10km/sec, an indication of the gravitational redshift. (see sec 2.4)

Finally, modeling the spectrum using solar metal abundance absorption lines resulted in metal lines far too strong compared to the observations. An abundance of 1/100 produced lines of insufficient strength, allowing for the setting of upper and lower bounds for the metallicity. The 'best fit' model giving a reasonable overall best fit was selected with 1/30 solar abundances.

## 2.4 Parameters of the Red Dwarf

A sensitive indicator of spectral type and temperature in mid M dwarfs is V - I colour. Colours for the M dwarf were calculated from CCD photometry and after subtraction of the WD contribution, yielded a mean value of 2.86 and a range from 2.95 to 2.75 (O'Donoghue et al. 2003). The spectral class chosen for the M dwarf in EC13471-1258 lies between M3.5 and M4.

From Reid & Hawley (2000) the mean temperature for an M3.5 dwarf is **3100** +/- **50**°K.

The determination of the rotational velocity from the broadening and depth of the spectral lines depends both on the intrinsic rotational velocity of the star as well as on the choice of spectral classification selected (O'Donoghue et al. 2003). The rotational velocity of the M dwarf, $V_{rot,2}$, was, through inspection, chosen to be $V_{rot,2}\sin i = 125 \pm 25$ km/sec.

The radial velocity curve of the M dwarf could be tracked by the H$\alpha$ emission line, the Na D absorption lines, or by the TiO molecular bands and other weaker metal lines. The results yielded an average radial velocity value of 266 +/- 6km/sec and -2 +/- 4km/sec for the $\gamma_2$- velocity. The difference in $\gamma$ velocity of the WD and RD arises from the gravitational redshift of light emitted by the WD.

The chemical composition of M dwarfs is indicated by the increase in strength of the CaH compared to the TiO molecular bands as metal abundance decreases (Reid & Hawley 2000). The results for the system EC13471-1258 match those of similar stars, all of which are normal disc M dwarfs. The conclusion was that the M dwarf had normal solar abundance.

## 2.5 Binary Analysis: Determining the Basic Parameters

With the fundamental characteristics of the two stars in this system estimated and consolidated into Table 2, it becomes possible to estimate the parameters of the system including the inclination angle, *i*, the separation between the two stars, *a*, and the gravitational red-shift.

| **Quantity** | **Value** |
|---|---|
| $P_{orb}$ | 13025.5 +/0.9sec |
| $T_{eff,1}$ | 14220 +/- 350°K |
| $\log g$ | 8.34 +/- 0.2 |
| $\log Z$ | -1.5 +/- 0.5 |
| $K_1 \sin i$ | 137 +/- 10km/sec |
| $\gamma_1$ | 61 +/- 10km/sec |
| $V_{rot,1} \sin i$ | 400 +/- 100km/sec |
| $K_2 \sin i$ | 266 +/- 6km/sec |
| $\gamma_2$ | -2.0 +/- 5km/sec |
| $V_{rot,2} \sin i$ | 140 +/- 10km/sec |
| $T_{eff,2}$ | 3100 +/- 75°K |

***Table 2: Summary of the Parameters for the Binary System, EC13471-1258. (from O'Donoghue et al. 2003)***

Using the standard equations of spectroscopic binaries one can derive the masses and radii of the individual stars:

$$
\begin{aligned}
&a = P_{orb}(K_1 + K_2)/2\pi \\
&M = 4\pi^2 a^3 / GP_{orb}^2 \\
&q = K_1 / K_2 \\
&M_1 = M/(1+q) \\
&M_2 = qM_1 \\
&R_{L,2}/a = 0.49q^{2/3}/(0.6q^{2/3} + \ln(1+q^{1/3}))
\end{aligned}
$$

Where, $a$ is the binary separation, M is the sum of the masses of the two stars, $q$ is the mass ratio of the secondary to the primary, and $R_{L,2}$ is the volume-equivalent Roche lobe radius of the secondary (Eggleton 1983).

The gravitational redshift can be estimated from the difference in the $\gamma$ - velocities from each of the stars in the binary, which, in this case amounts to 62+/-10km/sec. No evidence for binary eccentricity was found by O'Donoghue et al (2003).

## 2.5.1 Constraining the inclination angle, *i*.

The quantities listed in Table 2 show values for $K_1 \sin i$ and $K_2 \sin i$ not $K_1$ and $K_2$. For an accurate calculation of the mass, M, it is necessary to estimate the inclination angle, *i*.

Mass-radius diagrams were constructed in which integer values of $i$ between 75° and 90° were used in the calculation for values of $K_1 \sin i$ and $K_2 \sin i$ obtained from Table 2. Then the calculations were repeated using the error estimates from the same table as the perturbations of the velocity semi-amplitude. Mass/radius diagrams showing the results of these calculations for each component star appear in Figure 7.

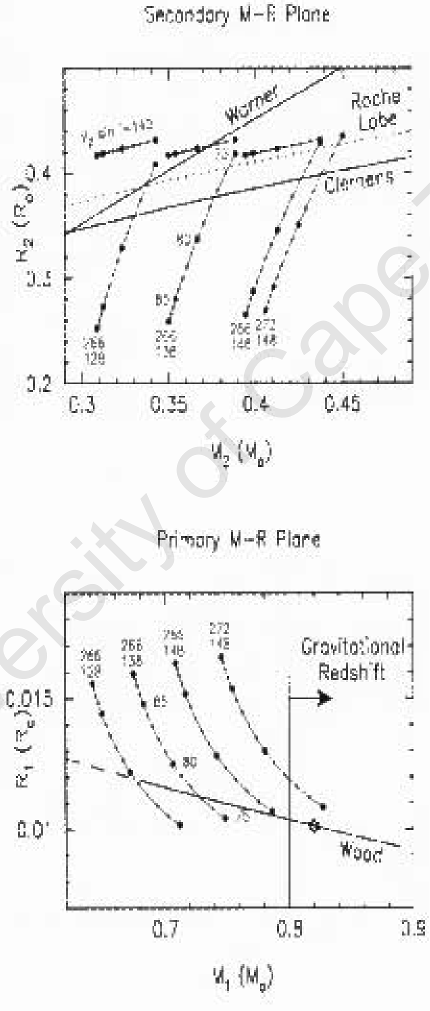

***Figure 7 - Mass-Radius Diagrams for the Primary (lower panel) and Secondary (upper panel).***
***(From O'Donoghue et al. 2003)***

***Each curve represents a solution for the binary using radial velocity semi-amplitudes. The dotted line in the upper panel represents the limit where the mean density of the M dwarf would exceed the Roche lobe, and therefore overfill. The Wood and Clemens relations further constrain the range of values.***

In order to determine an inclination angle and therefore a solution to the binary parameters, it was necessary to achieve consistency with previously determined parameters and the accepted mass radius relations of Wood (1995) and Clemens et al (1998). Assuming further that the M dwarf is just filling its Roche lobe, the best compromise between all these constraints and their errors gave a value for the inclination angle of **75.5° +/- 2°** (O'Donoghue et al. 2003).

## 2.5.2 The Binary Masses and Radii

With this inclination, the WD therefore has a mass and radius of 0.78 +/-0.04 $M_\odot$ and 0.011+/-0.01 $R_\odot$ and the M dwarf a mass and radius of 0.43 +/-0.04 $M_\odot$ and 0.42 +/- 0.02 $R_\odot$, respectively.

## 2.5.3 The Binary Separation, a, and other Parameters of the System.

Finally, with the basic parameters determined we are able to calculate the binary separation, a, the position of the center-of-mass of the system, and other binary parameters listed in Table 3.

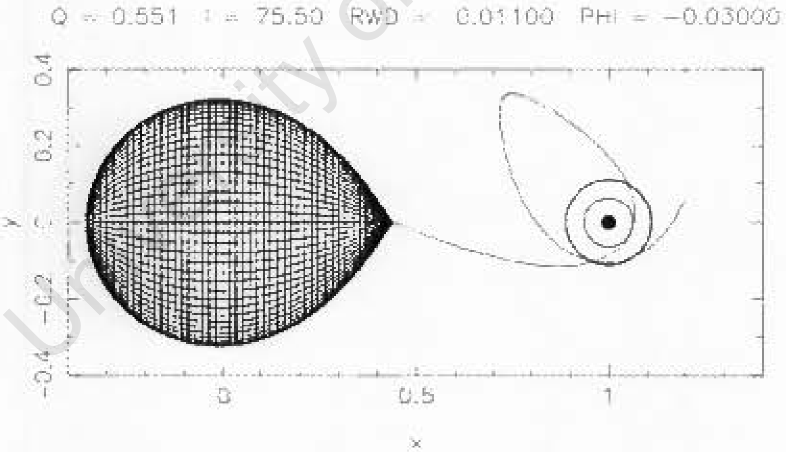

***Figure 8 - Model of the Binary System, EC13471-1258 and Trajectory Path for Mass-Transfer from the RD to the WD via $L_1$.***

***At left is the RD shown filling its Roche lobe and at the right is the WD, (No Roche lobe shown). Also shown are circles indicating the radius of minimum approach of the trajectory path, $R_{min}$ (Inner Circle), and the circularization radius, $R_{circ}$ (Outer Circle).***

| **Quantity + Value** | **Description + Formulae** |
|---|---|
| $a = 8.835x10^{8} m$ | a - Separation between the two stars, center to center<br>$a^3 = (G(M_1 + M_2)P_{orb}^2)/4\pi^2$ (2) |
| $a_1 = 3.145x10^{8} m$<br>$a_2 = 5.69x10^{8} m$ | $a_1$, $a_2$ - Distance from center-of-mass to center of primary, secondary<br>$a_1 = (M_2/M)a \quad a_2 = (M_1/M)a$ (3) |
| $R_{L,1} = 3.81x10^{8} m$ | $R_{L,1}$ - Roche lobe radius (center of primary to $L_1$)<br>$R_{L1}/a = 0.5000 - 0.227\log q$ $(0.1 < q < 10)$ (4) |
| $R_{L,2} = 2.89x10^{8} m$ | $R_{L,2}$ - Roche lobe radius of secondary<br>$R_{L,2}/a = (0.49q^{-2/3})/[0.6q^{-2/3} + \ln(1+q^{-1/3})]$ (all q) (5) |
| $R_{\min} = 5.68x10^{7} m$ | $R_{\min}$ - Radius of closest approach to primary<br>$R_{\min}/a = 0.0488q^{-0.464}$ $(0.05 < q < 1)$ (6) |
| $R_{circ} = 9.78x10^{7} m$ | $R_{circ}$ - Radius at which matter injected from $L_1$ will settle into orbit<br>$R_{circ}/a = 0.0859q^{-0.426}$ $(0.05 < q < 1)$ (7) |

***Table 3 – Binary Parameters for the system EC13471-1258***
***(Formulae from Hellier 2001, p.24)***

## 2.6 Examining the H$\alpha$ Emission Data

In an effort to examine the origin of the H$\alpha$ emission, trailed orbital spectra and a corresponding Doppler tomogram were constructed in order to locate the spatial position(s) for the origin of H$\alpha$ emission (O'Donoghue et al. 2003).

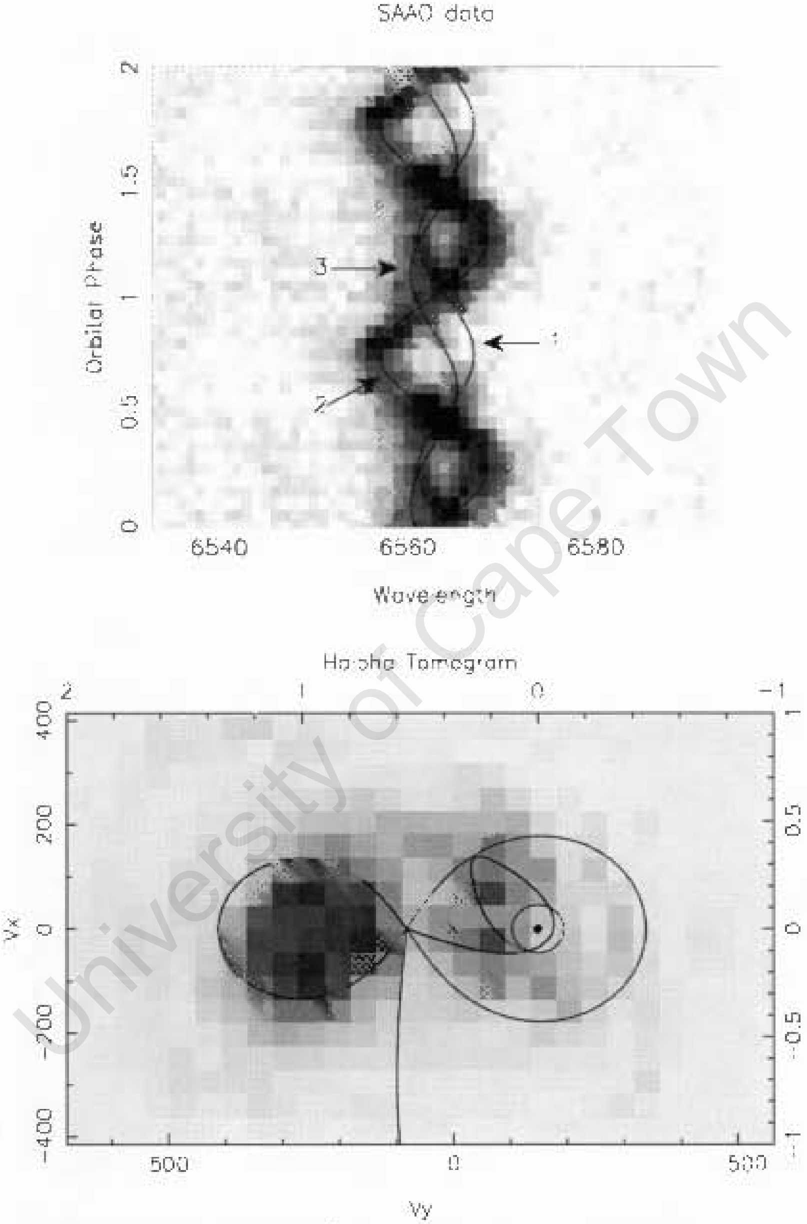

*Figures 9 - Trailed Spectra and Doppler Tomogram*
*(O'Donoghue et al. 2003)*

***Top:** A Doppler trailed spectrum plot of H$\alpha$ emission. The numbers refer to the 1) velocity path of WD, 2) velocity path of RD, and 3) Binary Orbital Motion of H$\alpha$ emission at position (0.75, -0.75) in the tomogram, bottom.*

***Bottom:** A Doppler tomogram for the H$\alpha$ emission showing axes in velocity and spatial coordinates. The centre-of-gravity of the system is marked with an x, and the circle around the WD (0,0) represents the circularization radius where matter emitted through the L1 point would orbit.*

The trailed spectrum shows unequivocal evidence for at least 2 components of the H$\alpha$ emission line moving in opposition to each other. One component is clearly attributable to the M dwarf. The other must originate in the WD's Roche lobe. In the tomogram, the orbital motion of emission generated from the RD corresponds to the path labeled (2) in the trailed spectra. The orbital motion of emission from within the WD Roche lobe concentrates within two distinct regions. These correspond to the velocity coordinates (Vx,Vy) = (-25,-75) and (75,-75) km/sec. These rotate around the center-of-mass and can therefore be converted into orbital motion. The orbital motion of the velocity coordinates, (75,-75) km/sec, correspond to the path labeled (3) in the trailed spectral plot in Figure 9 (top). As stated by O'Donoghue et al. (2003):

"The interpretation of these two distinct features in the Doppler map is not straight forward. Neither occurs at a "special" place in the binary, i.e. a natural site for emission such as the intersection of the mass transfer stream with the circularization radius. There is no obvious accretion disc in the system of the kind seen in cataclysmic variables. Yet, there may be a very weak mass transfer stream flowing from the $L_1$ point, and we would expect to see features in the Doppler map corresponding to where this stream collides with itself".

In the case of the above tomogram the two prominent emission features occur near to but not precisely in the positions of the expected emission.

In an effort to further understand the appearance of H$\alpha$ emission from the vicinity of the WD, we undertook a program of spectroscopic observation of EC13471-1258 in Sutherland, South Africa, using the SAAO 1.9 meter telescope along with the SAAO CCD Spectrograph. This took place over three separate weeks in March 2004 and March and April 2005 and forms the basis for this thesis.

The intention was to acquire higher resolution spectral images of the H$\alpha$ emission for the purpose of defining the velocity and spatial positions of the emission more precisely. This was the central scientific goal of this project.

# Chapter Three

# Data Acquisition, Reduction and the Production of Higher Resolution Trailed Spectral Plots

## 3.1 The CCD Spectrograph

The CCD Spectrograph is an instrument which is mounted on the 1.9 meter telescope in Sutherland, RSA. Its CCD has a pixel grid of 266x1798 with a pixel size of 15 $\mu$m. To reduce the dark current, the CCD is cooled to about $180^0$K with liquid nitrogen.

In order to take data for H$\alpha$ we chose "grating 5" with a first order spectral range of 6400 Å to 7200 Å, which covers the H$\alpha$ emission line of 6562.8 Å. This grating further offers 1200 line/mm, a blaze peak at 6800 Å, dispersion of 50 Å /mm and with resolution of 1 Å. We used a filter (GG495) to eliminate any blue light second order effects, and chose a grating angle of $-3^{\circ}$ to position the spectral range as close to the blazing as possible.

We chose a slit width of 250 $\mu$m corresponding to about 1.5 arcsec on the star, and used exposure times of 500 seconds to obtain the best signal/noise possible.

A CuNe arc lamp was used to calibrate the spectral lines because it gives a good number of strong lines between 6000 Å and 7000 Å, and we took arc spectra before and after each set of three 500-second exposures.

### 3.1.1 Initial Setup and Calibration

#### The Camera Focus: The Hartmann Focus Test

The Hartmann test is used to focus the spectrograph camera. It is necessary to take two successive arc exposures with the one half of the collimated beam occulted and then another exposure with the other half occulted. The mean shift between spectral lines in the two exposures indicates the distance and direction from the ideal focus. The camera focus can then be adjusted on the telescope using a micrometer on the instrument package.

#### Observational Procedure

The telescope was focused at the start of each night and regular checks on focus were made. A guide star kept the target on the slit. Access to the target limited us to obtaining one to two binary orbits per night.

### 3.1.2 Flat Fields

A set of dome flats were obtained at the start or end of every evening to correct the pixel to pixel variation that might exist on the CCD. These data were consolidated and normalized for later use on the individual spectra in the reduction process.

## 3.2 IRAF: Reduction of the CCD Spectra

The Image Reduction and Analysis Facility (IRAF)[1] is a comprehensive software reduction program. The following steps were taken to prepare the spectra for further analysis. As we were only interested in the relative flux of the binary system we did not use a reference star for calibration.

### 3.2.1 The Reduction Process

#### Converting the 'Fits' format to IRAF format

The first step in the reduction process was to convert the raw FITS data files to IRAF format, using the IRAF 'rfits' command.

#### The Dome Flats

The dome flats for each given night were then combined and normalized using the IRAF 'flat combine' task. An output file was produced for later 'flat-fielding' or the removal from the spectra of pixel to pixel sensitivity variations.

#### Cleaning and Preparing the Fields

Cleaning, using IRAF's 'ccdproc' involves removing the bias which is the systematic offset due to the readout process, trimming the edges of the image from the CCD, flatfielding, and the removal of any dark current or charge contributions generated from thermal motions.

#### Aperture centering and sizing

Using optimal extraction (Horne 1986) the spectral images were reduced to one using IRAF's 'doslit' task.

---

[1] (IRAF) Image Reduction and Analysis Facility is distributed by the National Optical Astronomy Observatories (USA), which are operated by the Association of Universities for Research in Astronomy Inc. (AURA), under cooperative agreement with the National Science foundation.

## Wavelength Calibration

In order to calibrate the spectra, the IRAF 'doslit' task selects the arc exposure taken just before a given star and uses it to identify the spectral lines. A selection of wavelengths are manually entered and fitted. All the spectra were then resampled onto the same wavelength grid.

## Extracting and Fitting

IRAF then extracts the arcs before and after each set of images and attempts to fit them with a dispersion function which can be monitored interactively to ensure the correct wavelength calibration ( to an RMS accuracy of better than 0.1 Å )

## Converting spectra to ASCII two column format

In order to prepare the data for input into the subsequent programs, the data was converted from IRAF format to ASCII code using IRAF 'wtextimage' task.

## Changing from Julian Date to Heliocentric Julian Date

Heliocentric Julian Dates were calculated and attached to all the spectra.

## 3.3 Analysis of the Spectral Images

As listed in Table 4, the total number of spectra amounted to 202 of which there were 110 spectra from March 2004 and another 92 spectra from March 2005 (April 2005 was plagued with poor seeing and equipment problems and so spectra for April have not been used).

| **Run #** | **Date** | **Time Span** | **Exposure Time (s)** | **Central Wavelength (Å)** | **No. of Spectra** |
|---|---|---|---|---|---|
| **143** | **2004/Mar24** | **10:14-17:05** | **500** | **6600** | **44** |
| | **2004/Mar25** | **09:43-16:05** | **500** | **6600** | **42** |
| | **2004/Mar28** | **10:47-17:13** | **500** | **6600** | **24** |
| **160** | **2005/Mar 8** | **10:12-15:43** | **500** | **6600** | **38** |
| | **2005/Mar11** | **10:24-14:56** | **500** | **6600** | **30** |
| | **2005/Mar14** | **11:19-15:15** | **500** | **6600** | **24** |

***Table 4: Spectroscopy Observing Log***

### 3.3.1 Producing Trailed Spectra

The analysis of the spectra is best done using spectra folded into phase bins on the orbital period.

Using programs, in g77 Fortran, provided by O'Donoghue (SAAO), the results of the reduced and extracted IRAF spectra were used to produce a trailed spectral plot (see Figure 10) whose axes are the binary orbital phase and the Doppler shifted emission frequencies around H$\alpha$.

#### Modifying programs to provide 50 orbital phase bins

The existing program provided for 20 orbital phase bins. With the improved resolution we were able to have 50 phase bins. It was, therefore, necessary to modify the existing program to accommodate the additional number of bins. These 50 phase bins were divided on the basis of the Heliocentric Julian Date mentioned above. The orbital phase was then calculated for each spectrum using the mid-eclipse timings of the ephemeris (2.2.2).

#### Folding the spectra into orbital phase bins

Each spectrum was now identifiable by its orbital phase based on the ephemeris and it was possible to allocate each spectrum to the appropriate phase bin of the 50 bins allowed for.

#### Normalizing the phase data

#### Setting the continuum to unity

The continuum for each phase bin was normalized by taking a segment of the continuum in a region away from the emission line and then dividing it into the continuum effectively recalibrating the continuum to unity.

#### Plotting the trailed spectra

The phase bins were then plotted against wavelength and stacked to form a trailed spectral plot. Intensities were selected to show the continuum as white (1.0) and the maximum emission of (2.5) in black. Intermediate intensities varied in shades of grey and there was an overall signal to noise ratio of 25.

The trailed spectra for the March 2005 observations are shown in Figure 10. The spectra for March 2004 are not included as they did not show the high resolution of the March 2005 spectra. The results, therefore, rely most heavily on the 92 spectra from March 2005.

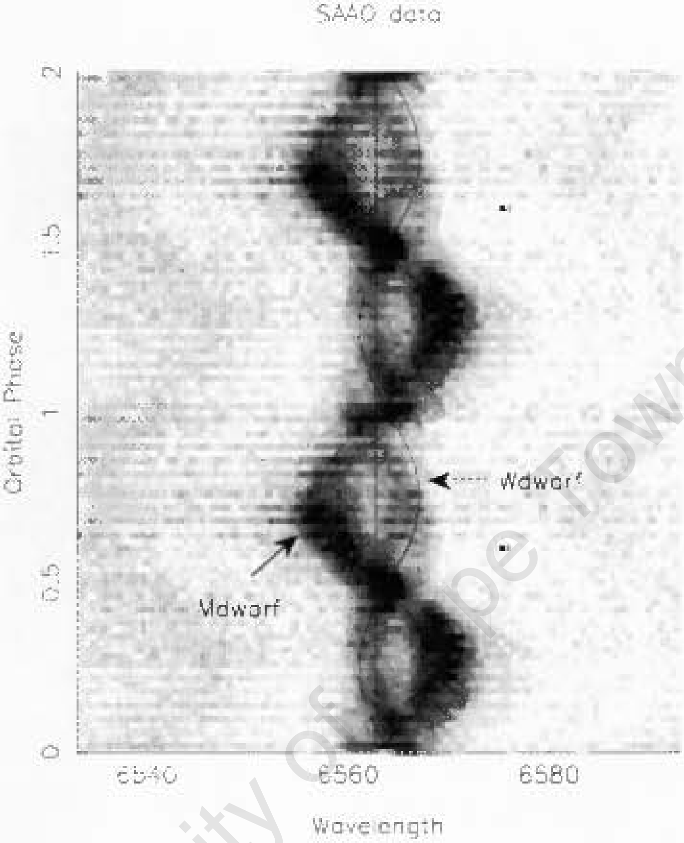

***Figure 10 - A (2005) trailed spectral plot for $H_{\alpha}$ emission, (6562.8Å) - Each orbital period is divided into 50 orbital phase bins. The plot shows one orbital cycle (0-1) repeated for clarity (1-2). White reflects the continuum and, in this case, black indicates a signal intensity of 2.2 above the continuum (1.0). Intermediate intensities are subdivided into grey scales within this range. Also indicated are the binary orbital motions of both the WD and the RD.***

## 3.3.2 Examining the Trailed Spectra

The trailed spectral plot in Figure 10 shows the $H_{\alpha}$ emission line as a function of orbital phase for the binary system. On inspection, one can see at least two sinusoidal interlacing waveforms which, in velocity space, indicate that two emission components are moving in opposite directions along the line of sight. The thin solid line labeled 'M dwarf' corresponds to the orbital motion of the RD, as determined by O'Donoghue et al. (2003). We know that the RD is chromospherically active, which is typical of this type of late red-type star (O'Donoghue et al. 2003). One component of the $H_{\alpha}$ emission line matches this solid line well.

Although the motion of one component of $H_{\alpha}$ matches that expected from the RD, there are strong intensity variations. The most obvious is the decline in strength between orbital phases 0.38-0.44. This component of the line is also stronger between orbital phases 0.5 – 0.7 than between 0.7 – 0.9.

The curve labeled 'Wdwarf' corresponds to the orbital motion of the WD, as determined by O'Donoghue et al. (2003). This path has been adjusted to account for gravitational red-shifting of the $H\alpha$ signal. This is due to the intense gravitational field of the WD which creates a potential well out of which the $H\alpha$ emission must emerge. This takes energy and an increase in wavelength is the result, hence the redshift. It has been shown (O'Donoghue et al. 2003) that the gravitational red-shift for this WD would be about 62km/sec.

There appears to be a third component of $H\alpha$ emission, (see Figure 13c, p.36 for clarity). This moves in roughly the same way as the WD but on closer inspection, the WD orbital motion does not match the motion of the second emission component as well as might be expected. In the first few orbital phases (0.0 – 0.2) the emission is well to the red of the WD's motion.

Moreover the component is obviously more complex than is consistent with a single source of emission. For example, at orbital phases close to eclipse, the component is clearly doubled into 2 sub components. Although less clear, the same seems to be true at orbital phase 0.5 (see also Figure 11 which shows it more clearly). It might be tempting to interpret these 2 sub-components as the classical doubled emission line profile of an accretion disc. However the overall impression is not that of a pair of sub-components moving in parallel but rather of two distinct sub-components reaching maximum and minimum of their wavelength range at different orbital phases.

### 3.3.3 Looking at the Emission Intensities

Figures 11 and 12 show plots of the emission in which the threshold for the highest intensity coloration has been progressively reduced. In all the plots the continuum has been normalized to 1.0 representing white.

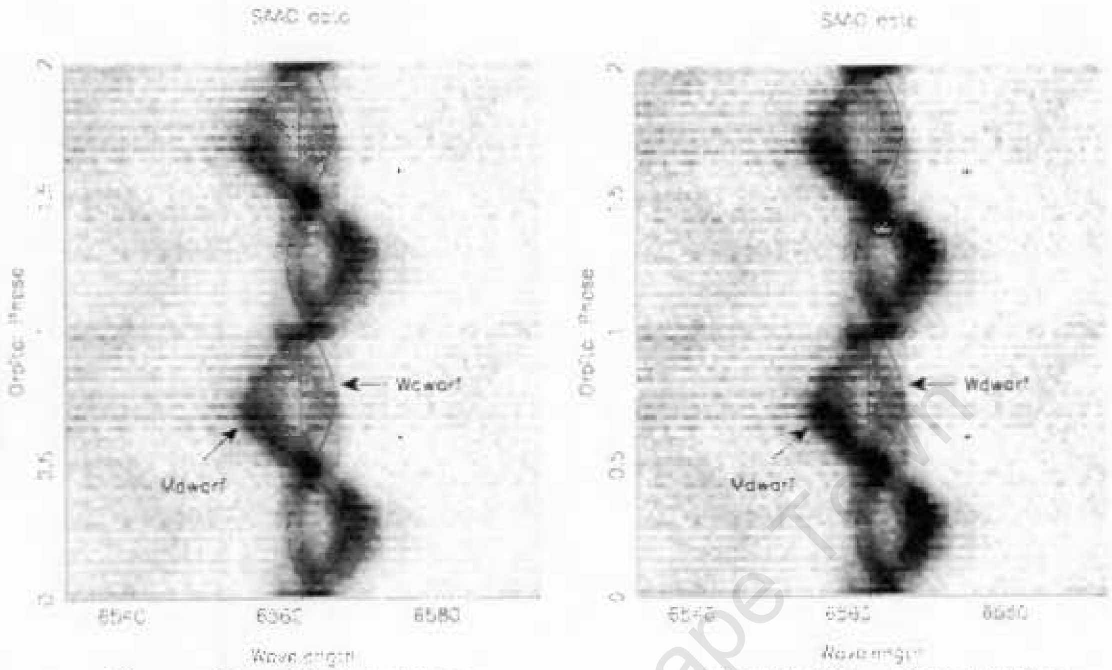

***Figure 11a - Dark regions indicates emission above 2.5***

***Figure 11b - Dark regions indicates emission above 2.2***

***Figure 11c - Dark regions indicates emission above 2.0***

***Figures 11abc - 2005 Plots of Trailed Spectra for Varying Grey Scales. The continuum is set to white and the shades of grey to black vary by plot and indicate spectral intensities above the continuum.***

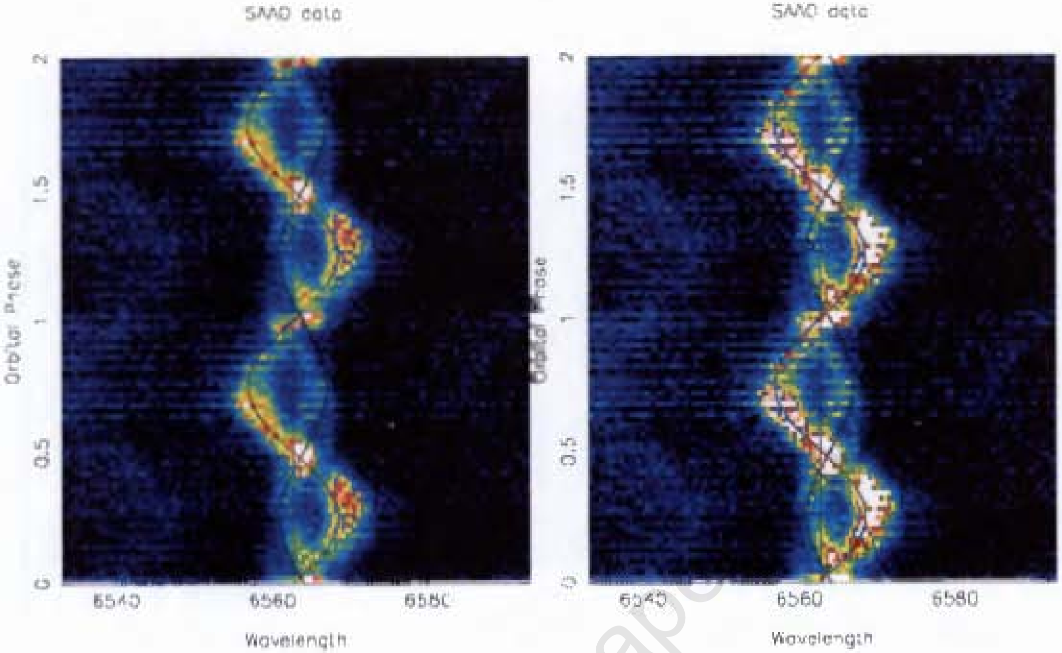

*Figure 12a – White areas indicate emission above 2.5*

*Figure 12b – White areas indicate emission above 2.2*

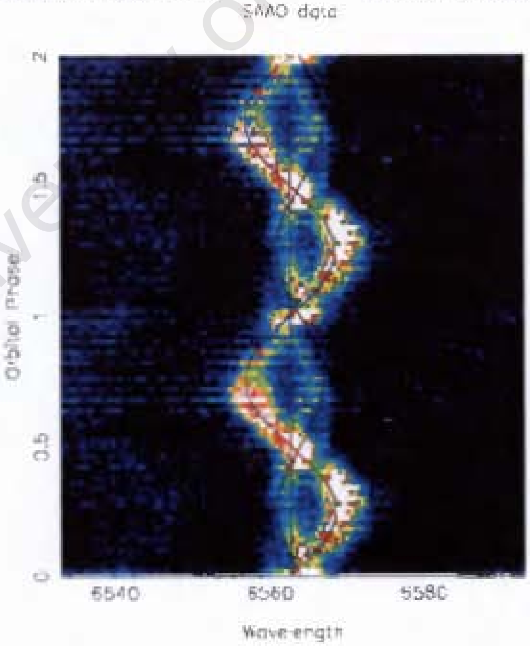

*Figure 12c – White areas indicate emission above 2.0*

***Figures 12abc - Varying Color Scales (2005 data)***
***Black reflects the continuum and white corresponds to the highest intensity emission.***

The color scales of Figs. 12 show the best contrast of intensity. They indicate that the highest amplitude emission arises near conjunction, (see phase 0.5 of Figs. 11a and 12a). The emission in this phase interval is more intense than that of the RD at other phases, showing levels above 2.5. This is easily understood as arising from the summation of the oppositely moving H$\alpha$ components.

If one follows the orbital motion of the RD, one finds that there is prominent and substantial emission at signal intensity above 2.2 along much of its orbit. There are, however, regions along its orbital motion where the signal has decreased below intensity level 2.0, for example between phases 0.7-0.9. The peak signal intensity for the RD emission was less than 2.5.

The plots in Figs. 12 further show that the emission appearing on the WD side of the center-of-mass is not as intense as that from the RD, as most of the emission is below level 2.0.

## 3.3.4 Comparing the Different Data Sets

In this section we look at the trailed spectral plots using data collected over three different years. This includes the data collected in 2002 and presented in the O'Donoghue et al. (2003) paper, data collected by D. Kilkenny (2004) and myself (2005).

The original trailed spectral plot (O'Donoghue et al. 2003) divided the orbital period into 20 phase bins whereas the orbital period in the 2004 and 2005 plots were able to be divided into 50 phase bins, allowing for the separation of phases into smaller orbital intervals, thereby improving the overall resolution.

### 3.3.4.1 Features in Common

The trailed spectral plots shown in Figures 13 are produced from the three data sets mentioned above. The plots are generally similar in appearance. They all show the motion of the RD as well as features moving in opposition. The features moving in opposition to the RD clearly originate from within the WD's Roche lobe. We shall refer to these features as "WDRL" emission.

All the trailed spectra plots show strong WDRL emission moving from red to blue in the first phases of each plot, (0.0 – 0.2) of Figs. 13. The emission is prominent not only in its intensity but also its appearance in all of three trailed spectral diagrams is similar.

The O'Donoghue et al. (2003) trailed spectra suggest this WDRL feature as matching the orbital motion of the WD. The higher resolution data show that this is not the case in that the gravitationally red-shifted orbital motion of the WD lies outside, to the blue, of this WDRL emission region.

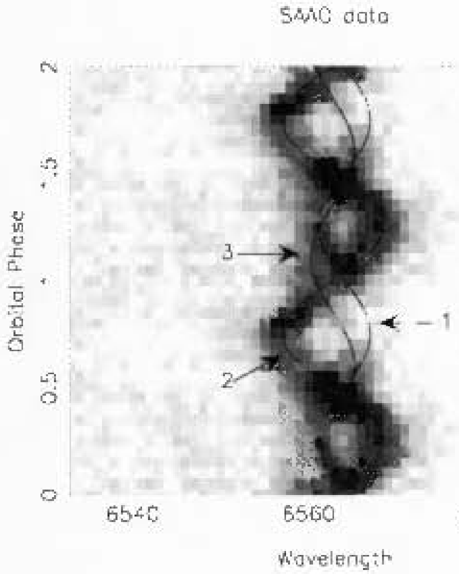

*Figure 13a - Trailed Spectral Plot of O'Donoghue et al. 2003 Data*

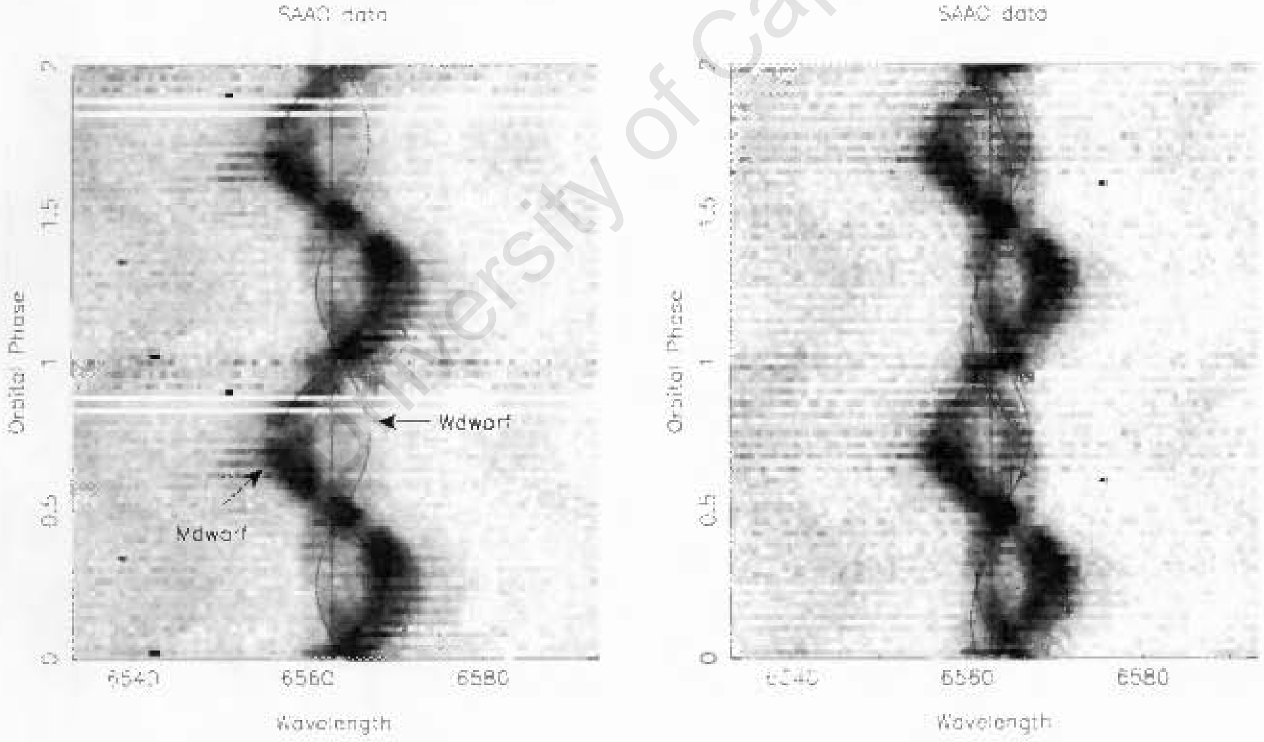

*Figure 13b - Trailed Spectral Plot of 2004*

*Figure 13c - Trailed Spectral Plot of 2005*

*Figure 13 - Trailed Spectral Plots from O'Donoghue et al. (2003), 2004, and 2005 spectra. The curve labeled 3 in Figure 13a is reproduced in Figure 13c as is the sinusoid showing the motion of the WD, labeled 1 in Figure 13a.*

### 3.3.4.2 Differing Features

The phase intervals of reduced RD emission clearly differ on the O'Donoghue et al. (2003) and 2005 plots, indicating its transient nature.

In the O'Donoghue et al. (2003) spectra, there is a clear reduction of RD emission strength on the blue side during phases 0.6 and 0.75 whereas in the 2005 spectra this is not the case. The 2005 spectra show a reduction in signal from phases 0.75 and 0.95.

In addition, the O'Donoghue et al. (2003) spectra do not show the reduction in the RD emission during phases 0.38 and 0.44, which is clearly visible in the 2005 spectra, although this might be due to the lower resolution of the O'Donoghue et al. (2003) data.

Curiously, the March 2004 spectra show weaker and more diffuse emission on the WD side of the system. There is no apparent reason for this. The signal to noise is similar to the 2005 data and the telescope and spectrograph used were the same. Identical settings on the spectrograph were used, save for a narrower slit opening...200 $\mu$m(2004) vs. 250 $\mu$m (2005).

In order to further understand the rather large difference between the 2004 and 2005 plots we examined individual phase bins for each observation period.

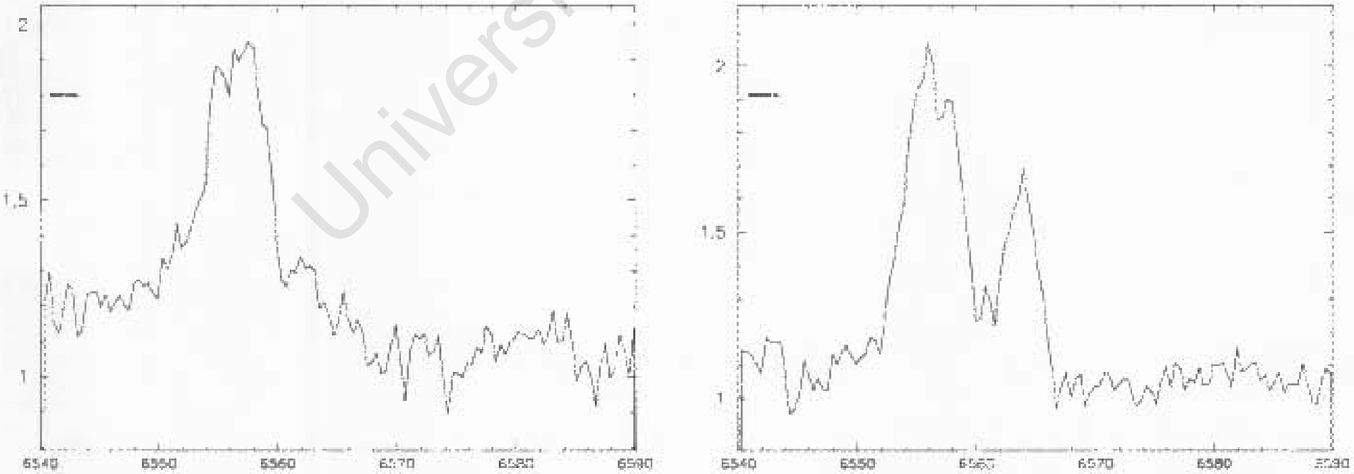

***Figure 14- Plot of Normalized Intensity (ordinate) vs. Wavelength (Å) (abscissa) Spectra from 2004(left) and 2005(right) for the same Orbital Phase (0.75 or Second Quadrature) as an example of the high degree of Variability in the Signal.***

Inspection of the two plots in Figure 14 shows the varied if not transient nature of the emission signal. The plots represent the normalized sum of the spectra for the same orbital phase. This perspective is from the second quadrature, at orbital phase 0.75, where we would expect two peaks on either side of the rest frequency, indicating the Doppler shifted emission from the regions of each of the two stars.

The plot on the right from 2005 shows these with a peak at 6556 Å for the approaching RD emission and a peak at 6565 Å for the receding emission from the WD Roche lobe region. Of significance is the complete lack of red-shifted emission from the WD Roche lobe region in the 2004 data. This is indicated in the range 6562 Å through 6567 Å.

The overall intensity for the RD emission is similar for the two data samples although slightly lower for 2004 at just under 1.9 compared to the 2005 data peaking at 2.1.

This shows evidence for the variable nature of the emission over a timescale of one year.

# Chapter Four

# Modeling the Mass-Transfer Stream Trajectory[3]

In an effort to further understand the origins of the emission, and considering that there are some regularly observed features to some of the emission, it seemed most likely that there might be some form of low mass-transfer taking place between the stars in this system (O'Donoghue et al. 2003).

To this end, it became necessary to investigate and understand the trajectory and velocities of such a stream in an effort to locate the most likely sources of emission and then to compare their expected emission velocities with those observed in the trailed spectral plots.

## 4.1 The Mass-Transfer Trajectory Model

The trajectories were modeled according to the two-dimensional restricted three-body model which assumes that the two stars are spherical and can be represented by point masses, that all three bodies rotate in a plane, and that the third body is taken to be a particle along the trajectory path with negligible gravitational effect. Justification for this approach has been established by Lubow & Shu (1975).

The coordinate system was chosen to rotate with the binary system, (in the frame of the binary), with the secondary located at coordinate point (X=0,Y=0) and the primary located at point (1.0), see Figures 15 or 16.

The equations of motion (Warner and Peters 1972; Flannery 1975) describe the trajectory of a particle (massless) within a system of two gravitationally bound masses.

$$\ddot{X} = 2\dot{Y} - {}^{\mu X}\!\big/_{r_2^3} + (1-\mu)\,{}^{(1-X)}\!\big/_{r_1^3} + X + \mu - 1 \qquad (8)$$

and

$$\ddot{Y} = -2\dot{X} - \mu\,{}^{Y}\!\big/_{r_2^3} - (1-\mu)\,{}^{Y}\!\big/_{r_1^3} + Y \qquad (9)$$

where

$$\mu = {}^{M_2}\!\big/_{(M_1 + M_2)} \qquad (10)$$

---

[3]The initial Fortran program code provided by D. O'Donoghue (SAAO)

In equations 8 - 12, X and Y are the x and y coordinates, velocities and accelerations of the particle, $M_1$ is the WD mass, $M_2$ is the RD mass and $\mu$ is the mass fraction.

This is a dimensionless form of the equation of motion and $r_1$ and $r_2$ reflect the distances to the primary and secondary, respectively from the mass being transferred.

The Jacobi Energy (E) is an integral of the motion and is constant for all time, for a given trajectory. So, a particle with a certain Jacobi Energy cannot go to regions of space that require larger values of *E* and cannot transfer to orbits of another Jacobi Energy without some sort of non-conservative interaction.

The Jacobi Energy is therefore conserved,

$$E = \dot{\mathrm{X}}^2 + \dot{\mathrm{Y}}^2 - 2\Omega(\mathrm{X},\mathrm{Y}) \tag{11}$$

where,

$$\Omega(\mathrm{X},\mathrm{Y}) = {}^{1}\!/_{2}[\mu r_2^2 + (1-\mu)r_1^2] + M\,{}^{\mathrm{Y}}\!/_{r_2} + {}^{(1-\mu)}\!/_{r_1}\,, \tag{12}$$

and

$$M = M_1 + M_2\,.$$

In the mass transfer model, the particle begins its trajectory at $L_1$ with a small initial velocity generated from thermal motions (10km/sec - see also Lubow & Shu 1975). Following the approach of Warner and Peters (1972), we used a 4th-order predictor-corrector scheme and a 5th order Runge-Kutta formula to determine the velocity and position of the test particle.

The code was then iterated and the step size was adjusted in order to keep the Jacobi Energy within tight limits between the predicted and calculated positions of each step of 1 part in $10^4$ over the entire trajectory. The resulting plot of the trajectory is shown in Figure 15.

## 4.2 Examining the Trajectory Stream

A plot of the path of the trajectory stream is presented in Figure 15 which shows the mass transfer leaving the $L_1$ point at the tip of the RD's Roche lobe and its subsequent motion in the vicinity of the WD.

The path of the matter crosses the circularization radius which is shown as the outer ring around the WD on the right in Figure 15. It then reaches its radius of closest approach, shown as the inner ring around the WD. Its momentum carries it away from the WD until the intense gravitational field of the WD causes its motion to loop back and return to again swing around the WD. Provided there are no collisions and no loss of energy, this process will continue indefinitely.

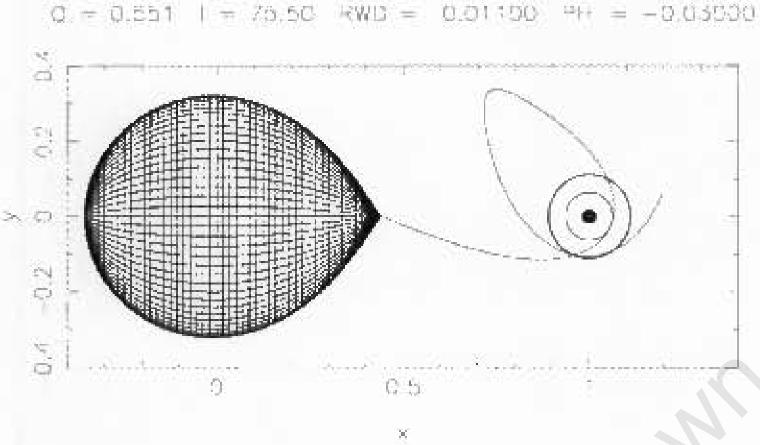

*Figure 15 – Model Trajectory path for Mass-Transfer from $L_1$ for EC13471-1258*

If there is no dissipation of energy through viscous interaction, matter that arrives in the vicinity of the WD Roche lobe via the $L_1$ point would, via collisions, end up in a circular orbit at $R_{circ}$, the circularization radius. Matter injected via other methods, (e.g. a wind), would also settle in an orbit comparable to its initial angular momentum. It is reasonable to assert that if there is matter in at least a semi-continuous flow injected into the WD Roche lobe, there must be an accumulation of matter somewhere within the Roche lobe and that this accumulation would most probably develop into some sort of radial thickening or disc structure orbiting around the WD.

If the mass-transfer flow is low or intermittent, the density of matter circulating at $R_{circ}$ might be too low for any significant (viscous) interaction and therefore matter there might orbit in an inviscid or dissipation-less ring at very low luminosity.

In this case, regular accretion onto the surface of the WD is unlikely considering that it is the formation of a viscous disc that allows the exchange of angular momentum necessary to move matter towards the WD surface.

Accretion could possibly occur from ballistic trajectories from such events as flaring of the RD, but these events are not particularly frequent (O'Donoghue et al. 2003) and could only account for irregular or perhaps random emission, should the gas be able to impact directly onto the surface of the WD.

## 4.2.1 Expected Regions of Enhanced $H_\alpha$ Emission

Assuming the system parameters in Table 3 (p.24), the circularization radius around the WD in EC13471-1258 is at a radial distance of 98000km from its center. Spatially, and assuming a planar topography, the transfer stream will intersect at this radius if there is no disc structure and continue on its trajectory if the matter interaction is collisionless. The position at the point of intersection is located at the coordinate-x position value of 0.96 in Figure 16, (see the arrow labeled 3). If the interaction between mass-transfer and matter circulating were of sufficient density, there might be collisions and some sort of measurable emission here.

Due to the planar topology of the binary system, and after the mass transfer has passed the point of closest approach to the WD, ($R_{min}$), there is a second possible impact point (at coordinates: 1.05, 0.09 or arrow 4 in Figure 16), where the trajectory path intersects the circularization radius a second time on its way towards the Roche lobe equi-potential surface (Hellier 2001). Here, the mass transfer velocity starts to decrease as the gas must climb out of the potential well of the WD's gravity field.

Another possible region of impact would be in the area of maximum displacement from the WD or near its Roche lobe surface where the gas swings around back towards the WD. At this point, the streaming velocities would approach zero (see arrow 5 in Figure 16). It is conceivable that there would be a buildup of matter in this region, as the mass must reverse direction and the low velocities would lengthen the crossing time.

A further potential impact point could be the return of the mass to the circularization radius (joining arrow #3) after first looping around the WD and returning from the first petal apex, arrow #5. This area is in the vicinity of the junction of three streams. The returning matter could impact with either the matter rotating in Keplerian orbit around the WD at $R_{circ}$ or it could impact with the initial mass transfer stream which crosses in this vicinity on its initial approach to the WD. The two returning streams could also potentially interact with each other. This, therefore, seems a highly probable area to find a source of the $H\alpha$ emission.

Finally, there is a finite possibility that some of the mass stream might be able to reach the second petal of the rosette trajectory, (see arrow 6 in Figure 16). Here again might be a source of emission.

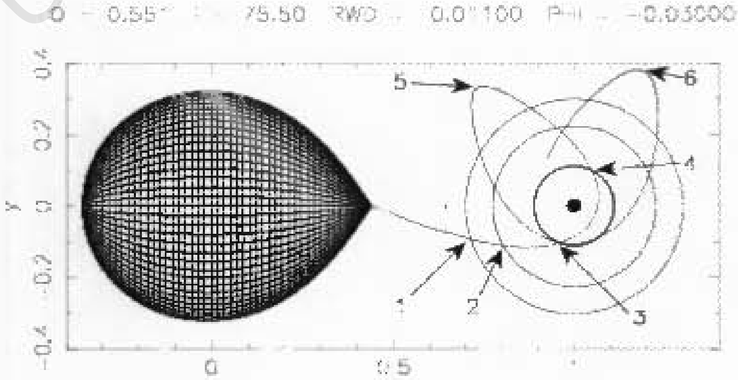

*Figure 16 - Most likely Regions of Collision. Two possible disc locations are drawn, with 'bright spots' expected in locations indicated by arrows 1 and 2.*

If matter were to accumulate at the circularization radius to such an extent as to become dense enough to interact viscously, there would most likely be the formation of a disc.

The point of interaction with a mass-transfer stream, the 'bright spot', would show emission generated from the outer radius of this structure.

As the size of the disc can vary, two circles have been drawn in Figure 17 as examples of possible outer disc rings and are marked for the two impact regions. The location of the 'bright spot' would depend on the extent of the disc. The arrows marked 1 and 2 in Figure 16 identify some possible regions of impact with a disc.

## 4.3 Curve Fitting of the Binary Motion

To further isolate the spatial positions for the WDRL emission, we constructed and overlaid sinusoidal curves onto the trailed spectral diagram (Figs.17) covering the regions where, on the trajectory plot of Fig. 16, there was a high probability of collision.

To this end we first chose to plot the radial velocity curves of the arrowed regions in Fig. 16 arising simply from orbital motion. This neglects any streaming or ballistic motions.

In this model, the arrowed regions 1-6 will produce classical S-waves arising only from their location in the binary reference frame w.r.t. the binary centre-of-mass. The emission is assumed to be from optically thin gas, and therefore isotropically emitted, equally visible at all orbital phases.

***Figure 17a – Orbital Motion for a 'Bright Spot' at Location 1 in Figure 16 2005 data***

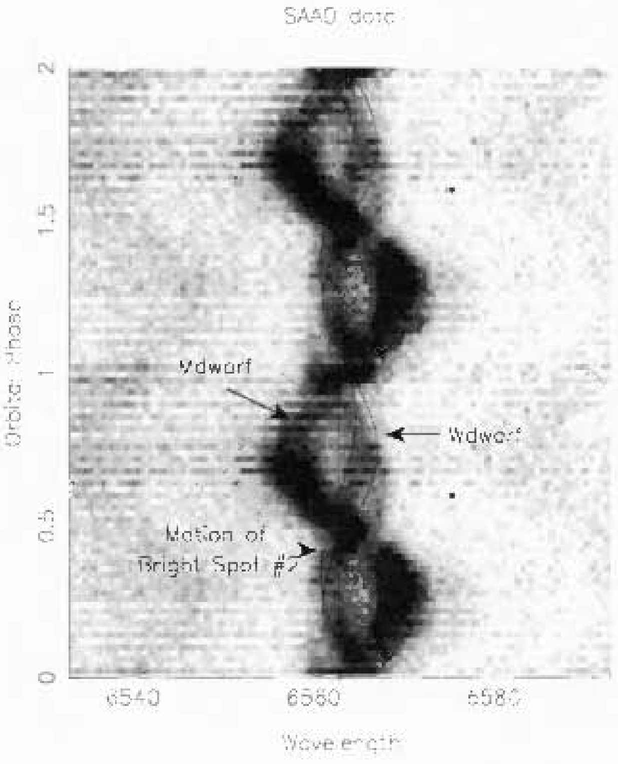

***Figure 17b – Orbital Motion for a 'Bright Spot' at Location 2 in Figure 16 2005 data***

The solid line labeled "Motion of Bright Spot #1" in Figure 17a represents the orbital radial velocity curve of the region indicated by arrow #1 in Figure 16. It shows very small amplitude due to the proximity of the region to the binary centre-of-mass. It does not explain any of the $H_{\alpha}$ emission observed.

The solid line labeled "Motion of Bright Spot #2", in Figure 17b, represents the orbital radial velocity curve of arrowed region #2 in Figure 16. This has larger amplitude and might be considered a match to some of the observed emission over orbital phases 0.1 to 0.4. It is an unacceptable match over 0.6 to 1.0.

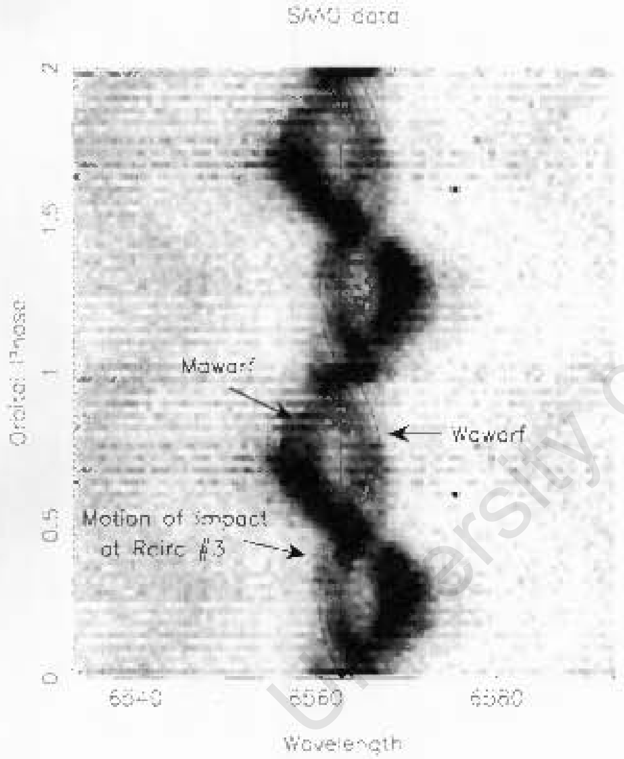

***Figure 17c – Orbital Motion for the Impact of the Trajectory Path with $R_{circ}$ in Location 3 of Figure 16a***
***2005 data***

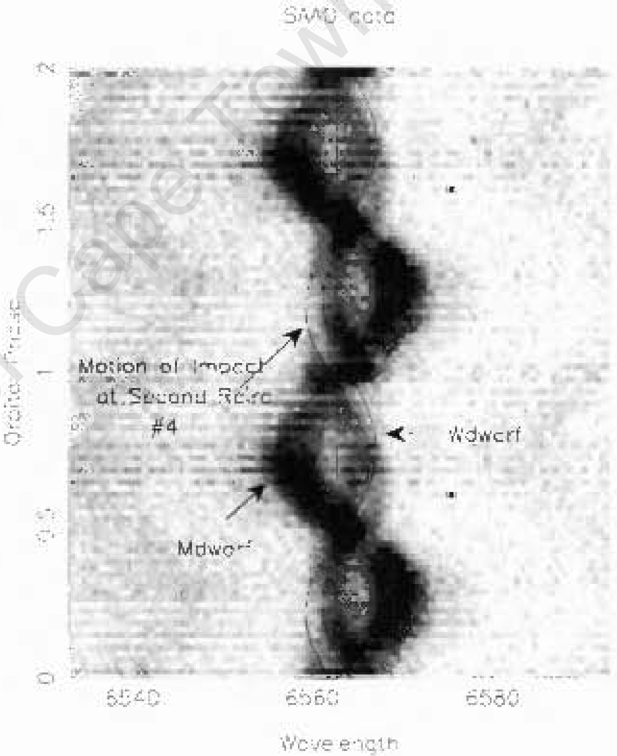

***Figure 17d – Orbital Motion for Emission from Impact at the second Junction of the Trajectory Stream with $R_{circ}$ in Location 4***
***2005 data***

Arrowed regions #3 and #4 of Figure 16 give rise to the orbital radial velocity curves shown in Figs. 17c and 17d. These radial velocity curves are generally similar to that of the WD, though there are small differences in amplitude and phase. We judge curve #3 to be a good match in phases 0.3 to 0.8 but less so in 0.8 to 1.3. Curve #4 is not as good a match as #3.

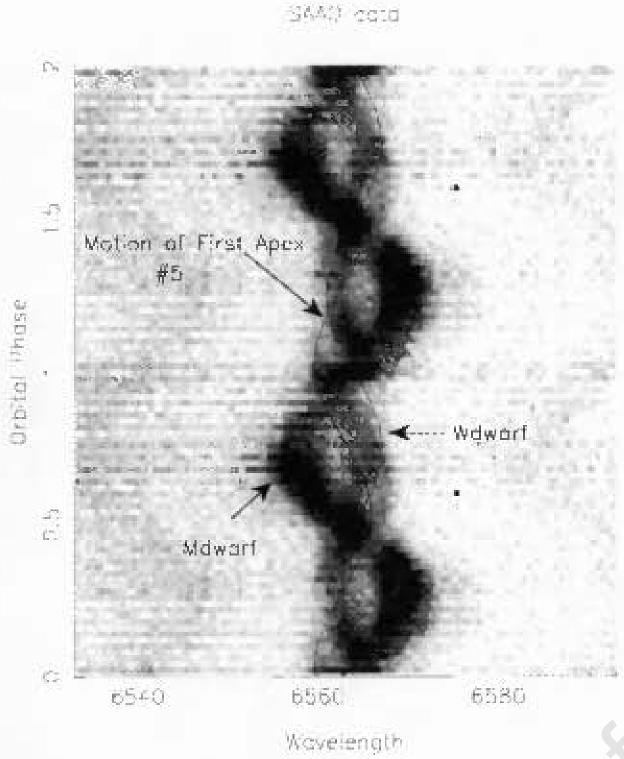

***Figure 17e – Orbital Motion for any Emission from Impact at the First Apex of the Rosette Petal at Location 5 of Figs. 16 2005 data***

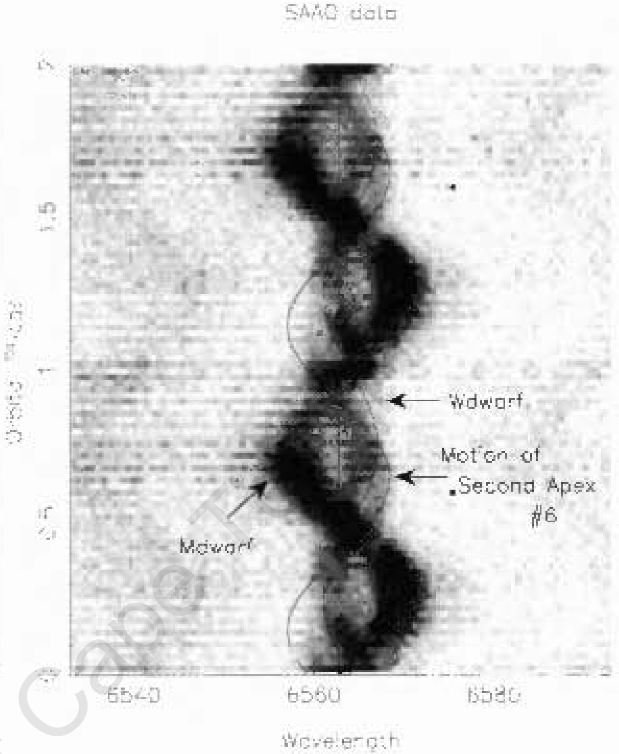

***Figure 17f – Orbital Motion for any Emission from Impact at the Second Apex of the Rosette Petal at Location 6 of Figs. 16 2005 data***

The arrowed regions labeled #5 and #6 of Figure 16 give rise to the orbital velocity curves of Figs. 17e and 17f, respectively. As mentioned in section 4.2.1, these correspond to the motion of emission from the apex of the first and second petal of the rosette where velocities in the frame of the binary would near zero, and the motion of the emission region should have, essentially, only one component, the orbital motion due to its position in the binary relative to the center-of-mass. There could, though, also be some low velocity, (under 100km/sec), streaming component as the location of zero relative velocity at the apex is a point, and we are considering the region around this point.

The motion of the curve labeled #5 in Figure 17e shows velocities which are of similar values to those observed from the emission. Although the overall 'fit' is not good, it does show some characteristics which coincide with the observed emission. This is particularly evident at orbital phase of 1.0 where the curve could account for the extended velocities of emission observed at eclipse.

This can be better understood by comparing the range of emission velocities at eclipse with those at orbital phase 0.5, which are distinctly dissimilar. The physical location of region #5 is not blocked during eclipse, at phase 1.0. Therefore, any emission from this region might account for the extended emission observed at eclipse.

The motion of the curve labeled #6 in Figure 17f shows higher velocity amplitudes than that of curve #5, again, due to its proximity in relation to the binary centre-of-mass. It does not appear to account for any observed emission between phases 0.0 to 0.3. Yet, between phases 0.3 and 1.0, the rest of the cycle, although, again, not a good curve 'fit', it could account for some of the emission. Similar to curve #5, the motion of curve #6 could also account for the extended velocities observed at eclipse.

Finally, between phases 0.5 and 0.6 the velocity distribution appears to divide into two separate streams. This could be as a result of more than one component contributing to the emission. Should this be the case, the motion of curve #6 could account for the emission observed in the second or outer path between phases 0.5 and 0.7.

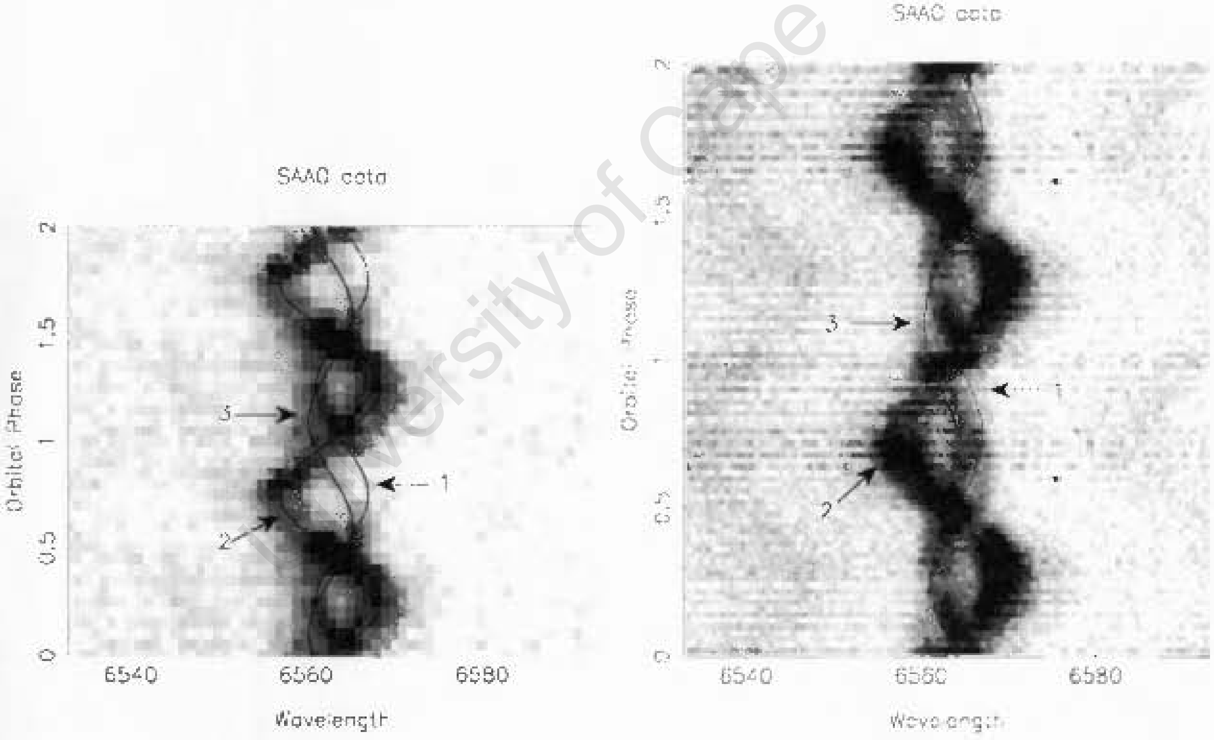

***Figure 17g***

***Figure 17h***

***Left - Orbital Radial Velocity Curves for the Motion of the most Likely Emission region given in the O'Donoghue et al. (2003) paper (see Arrow 3).***

***Right – A Similar Curve fitted over the 2005 data. Arrows 1 and 2 represent the motion of the WD and RD, respectively.***

The fitted curve in Figure 17g represents the orbital motion for the region (0.75,-0.75) in the tomogram shown at the bottom in Figure 9, (p. 25). The two plots overlay this orbital radial velocity curve over the trailed spectra from the original data set, O'Donoghue et al. (2003) on the left, and the 2005 data on the right.

The curve fitted to describe the orbital motion of the region (0.75,-0.75 in Figure 9) does not show the same emission characteristics along its path in the original data, Figure 17g, as in the more recent data, right in Figure 17h.

The WD orbital curve at the top of Figure 9 traces the curious feature described in section 3.3.4.1. It does not show the same fit as in the newer data of Figure 17g which shows the WD orbital radial velocity curve clearly adjacent, to the blue, of this feature at slightly higher velocities.

# Chapter Five

## Motion in the Frame of the Binary

In the previous chapter, the various possible emission sites were modeled as regions stationary in the binary reference frame, with the emitting gas having no streaming motions. Streaming motions were assumed to be converted to an isotropic velocity distribution, thereby broadening the observed emission but not influencing the orbital radial velocity curve. In this chapter, we consider the case where this is not true and allow for the streaming velocity of the gas.

### 5.1 Examining the Trajectory Stream Velocities

We used an initial velocity for mass ejected from the $L_1$ point of 0.03 using standard dimensionless thermal velocity units, ${}^{V}\!/_{V_o}$ ,

Where:

$$V_o = {}^{2\pi(a_1 + a_2)}\!/_{P} \qquad (13)$$

is the scale factor for velocity and *P* is the orbital period, (see Figure 1).

This equates to an initial velocity for V of 12km/sec. The results for this model are shown in Appendix (A), which displays a list of coordinate positions and velocities with reference to the line-of-sight observer to the system, for a particle moving along a trajectory, as shown in Figure17a.

In a high mass transfer stream the matter initially ejected through $L_1$ does so at a variety of angular trajectories. It appears that the higher the rate of transfer, the higher the density of the material. Therefore matter or gas injected at oblique angles will, through collision, eventually be caught up in the stream (Warner and Peters 1972).

### 5.1.1 The Ballistic Velocities of the Trajectory Stream

In this section we have used the Mass-Transfer Model of Chapter 4 to determine the velocities of the trajectory stream at the various most probable impact regions 1-6, identified in Figure 16. These are tabulated in the reference frame of the binary and listed in Table 5.

| **Region** | **1** | **2** | **3** | **4** | **5** | **6** |
|---|---|---|---|---|---|---|
| **$V_R$ (km/sec)** | **472** | **648** | **1167** | **1149** | **105** | **126** |
| **$V_X$ (km/sec)** | **459** | **642** | **1125** | **-522** | **-99** | **-133** |
| **$V_Y$ (km/sec)** | **-109** | **-85** | **312** | **1024** | **-36** | **3** |

***Table 5: Summary based on the Mass-Transfer Model quantified in Appendix A for the Expected Velocities, in the binary reference frame, of the Trajectory Stream at the Identified Impact Regions of Figure17. The trajectory stream returning from region #5 and impacting at region #3 would potentially form a three-stream impact. The velocity components of this returning third stream would be, according to step 1370 in Appendix A, (1142,-276).***

### 5.1.2 Identifying the Impact Velocities of Converging Gas Streams

With the ballistic velocities of the mass-transfer stream in hand, we can proceed to identify and estimate, for each region, the velocities of the two, or as in one case, three streams converging.

The regions defined by arrows #1 and #2 assume the existence of a disc and that the mass-transfer stream would interact or even collide with the outer edge of this disc. This disc rotates around the WD and in the frame of the binary its velocity relative to the centre-of-mass would be determined from its radial distance from the WD.

The velocities could then be calculated using basic principles e.g., Newton's 2nd Law and the Centripetal Force of Acceleration.

Arrows #3 and #4 refer to regions where the mass-transfer stream intersects the circularization radius on its approach towards the WD and then again as it swings around and moves away from it. As before, the velocities of the matter rotating in $R_{circ}$ can be determined from fundamental principles.

Regions indicated by the arrows #5 and #6 do not represent areas of impact collision with a second stream as do regions #1 to #4. Yet, there is a likelihood of emission through impact collision as these represent turning points where matter would slow to low velocities and therefore be available for collision over a longer period of time compared to other regions, thereby increasing the likelihood for collision.

The data in Table 6 lists the radial orbital velocities, again in the frame of the binary, for the circulating matter/gas streams into which the mass-transfer would cross or impact.

This, therefore, considers the velocities at the estimated location of impact, for matter in orbit defined by the three circles in Figure 16 and at the points labeled with arrows 1 to 4.

| **Region of Impact** | **1** | **2** | **3** | **4** |
|---|---|---|---|---|
| $V_{Orbital}$ (km/sec) | 620 | 709 | 1028 | 1028 |
| $V_X$ (km/sec) | 204 | 336 | 904 | -904 |
| $V_Y$ (km/sec) | -585 | -625 | -488 | 488 |

***Table 6: Summary of the Radial Orbital Velocities for matter/gas in Keplerian orbit around the WD at various radii. The component velocities (Vx, Vy) are given for the specific locations of impact where the circulating matter/gas and the trajectory stream meet, in the binary reference frame. The coordinate origin is located at the centre-of-mass of the binary system.***

### 5.1.2.1 Velocities of Emission from the Impact of a Gas Stream at Supersonic Velocities with the Outer Edge of a Disc.

After leaving $L_1$, the gas particles fall towards the primary, which increases their original sonic velocities to highly supersonic. If the stream is dense enough, it expands transversely at the velocity of sound. In any case, pressure forces are soon negligible and the stream trajectory is well described by following the orbit of single particles ejected from $L_1$ (Warner and Peters (1972).

If there is an established disc structure, the trajectory stream will impact its outer edge. Among other effects, two shocks may form, with the stream material passing through one and the disc material through the other. The two shock faces form a triangular shaped region with an opening angle ~M-1, where M is the Mach number of the converged downstream flow (Warner 1995 p. 39).

HST observations confirm that the maximum emission is roughly midway between the stream and the disc flow (Horne et al. 1994). From Doppler imaging of U gem, Marsh et al. (1990) found that the bright spot emission is a mixture of disc and stream material, each of which has passed through a shock. *The velocity of the bright spot emission lines is an average of the disc and the stream velocities.* Thus the emission comes from the region between the two shock fronts.

In addition, there is no reason to think that the mass transfer rate is constant. It would be conceivable that the ejection of matter or gas through the $L_1$ point occurs in blobs rather that in a continuous stream. This could depend on the extent and magnitude of the magnetic field of the RD. This could impart an element of randomness or perhaps periodicity to the emission characteristics.

## 5.1.2.2 Impact Emission Velocities considering the Stream/Disk Impact Model

In this subsection, we take velocities, in the frame of the binary, for the disk/stream impacting regions which have been identified as most probable locations and apply the results of Marsh et al. (1990) to calculate the velocities of the emission generated from these regions. These results have shown that the final emission velocity is the average of the stream and disk velocities. The values which are listed in Table 7 have been obtained by adding the individual velocity streams at point of impact vectorially using the values from Tables 5 and 6, then halving the resulting magnitude consistent with Marsh et al. (1990).

Strictly speaking, the application of the results of Marsh et al. (1990) would apply only to regions 1 and 2 where we assume a disk structure. It would be more accurate to treat regions 3 and 4 as two streams impacting. As we do not have a model for this scenario we have treated regions 3 and 4 in the same manner as for regions 1 and 2. Finally, regions 5 and 6 are not considered to be regions where multiple streams converge so the values for these regions remain unchanged.

| **Region** | **1** | **2** | **3** | **4** | **5** | **6** |
|---|---|---|---|---|---|---|
| **$V_e$ (km/sec)** | **480** | **598** | **1019** | **1039** | **105** | **133** |
| **$V_X$ (km/sec)** | **332** | **489** | **1015** | **-713** | **-99** | **-133** |
| **$V_Y$ (km/sec)** | **-347** | **-345** | **-88** | **756** | **-36** | **3** |

***Table 7: Summary of the Expected Emission Velocities generated at the Identified Impact Regions as a result of impact of a matter/gas stream with a disc. Ve represents the resultant emission velocity for a given region and Vx and Vy are its components.***

In region #3 there is the possibility of three streams impacting, the initial trajectory stream from $L_1$, the matter stream rotating at $R_{circ}$, and the trajectory stream returning from region #5 and moving towards the WD.

The velocity of the component in the x-direction is similar in all three cases and so we would not expect significant departure from the values given in Table 7. Yet, the y-component of the returning stream, at a velocity of -276km/sec could interact with either the trajectory stream from $L_1$, at a velocity of 312km/sec, or matter rotating in $R_{circ}$, at a velocity of -489km/sec. This could generate two different emission velocity components of **18km/sec** and **-212km/sec**, respectively.

This would result in emission velocities greater than 1000km/sec in all three cases and no such velocities were seen in any of the data sets.

# Chapter Six

## Motion in the Frame of the Observer

In this chapter we change our perspective from the rest frame of the binary system at its centre-of-mass to that of a stationary observer on Earth. From this view point any emission from a fixed position in the frame of the binary will appear as a sinusoidal waveform, an S-wave as a result of the binary motion.

We will account for not only the radial velocity curves generated from the orbital motion but also the emission velocities due to the streaming motions. The observed velocity, $\vec{V}observed$, is therefore composed of these two components, the velocity due to the orbital motion of the binary, $\vec{V}orbital$, and the streaming velocity of the emitting gas, $\vec{V}streaming$, relative to the binary centre-of-mass.

$$\vec{V}observed = \vec{V}orbital + \vec{V}streaming \qquad (14)$$

### 6.1 Expected versus Detected Motion in the Frame of the Observer

In this section we show trailed spectral plots of the observed emission overlaid with S-waves, generated from the information in Table 8. These account for the motion of the binary, Vo, as well as the motion of the predicted impact emission, Ve, due to the confluence of matter/gas streams in the regions #1 to #6, discussed. We then combine the two waveforms according to Equation 18 and plot the resultant.

Figures 18a and 18b represent the motion for each independent velocity component, left, which combine according to Equation 18 to yield the expected emission motion, right.
There does not appear to be any correlation between the observed emission and the expected motion of this emission in region #1. In fact, there does not appear to be any observed emission matching the motions expected for any of the regions #1 to #4.

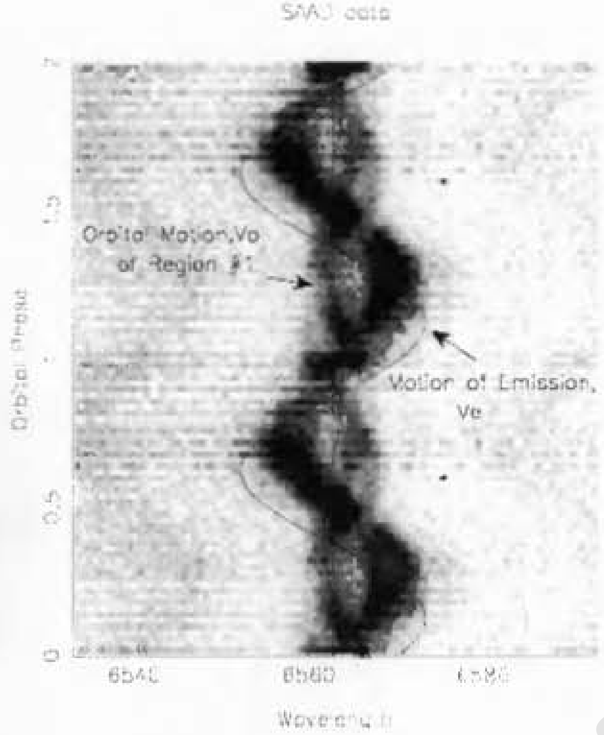

**Figure 18a**

**2005 data**

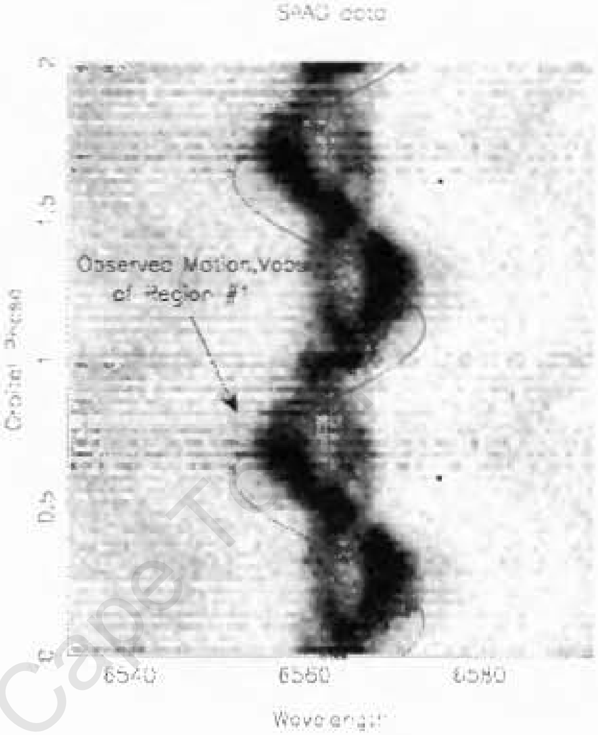

**Figure 18b**

**Figure 18c**

**2005 data**

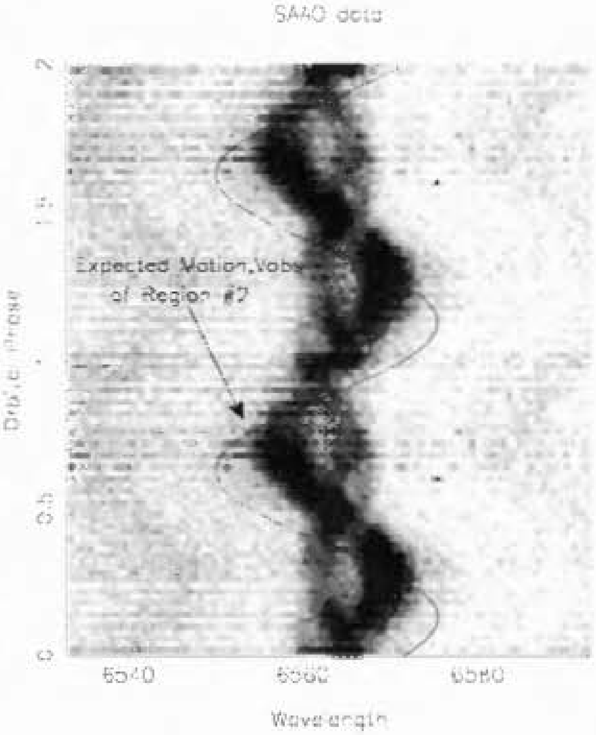

**Figure 18d**

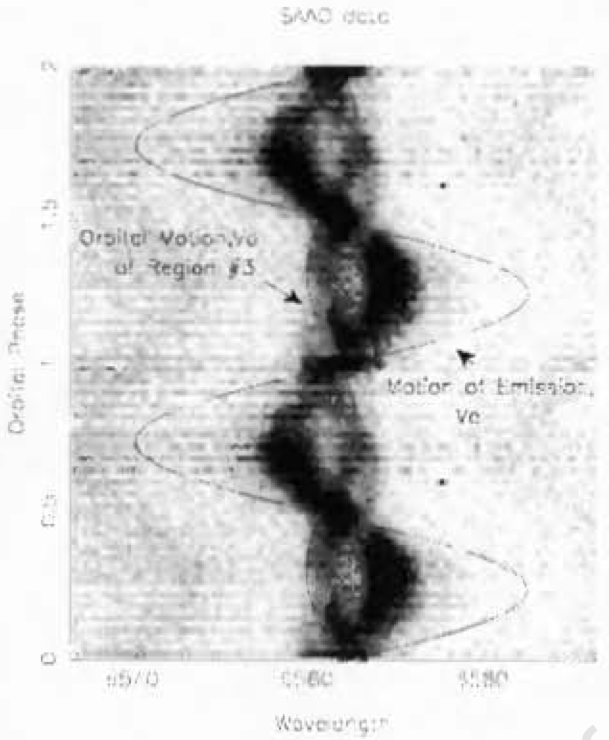

**Figure 18e**

**2005 data**

**Figure 18f**

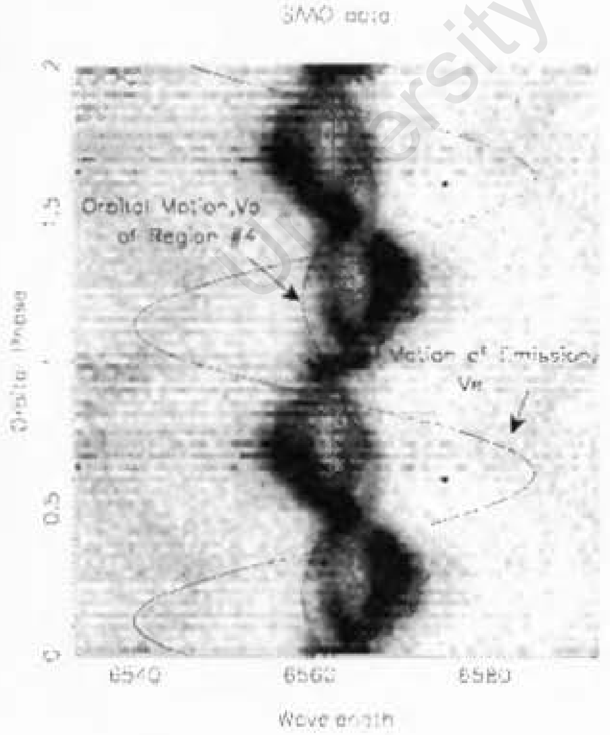

**Figure 18g**

**2005 data**

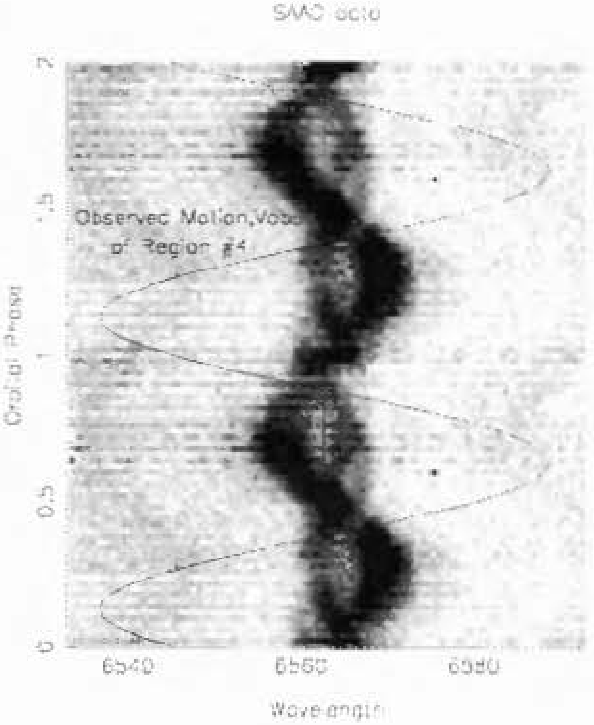

**Figure 18h**

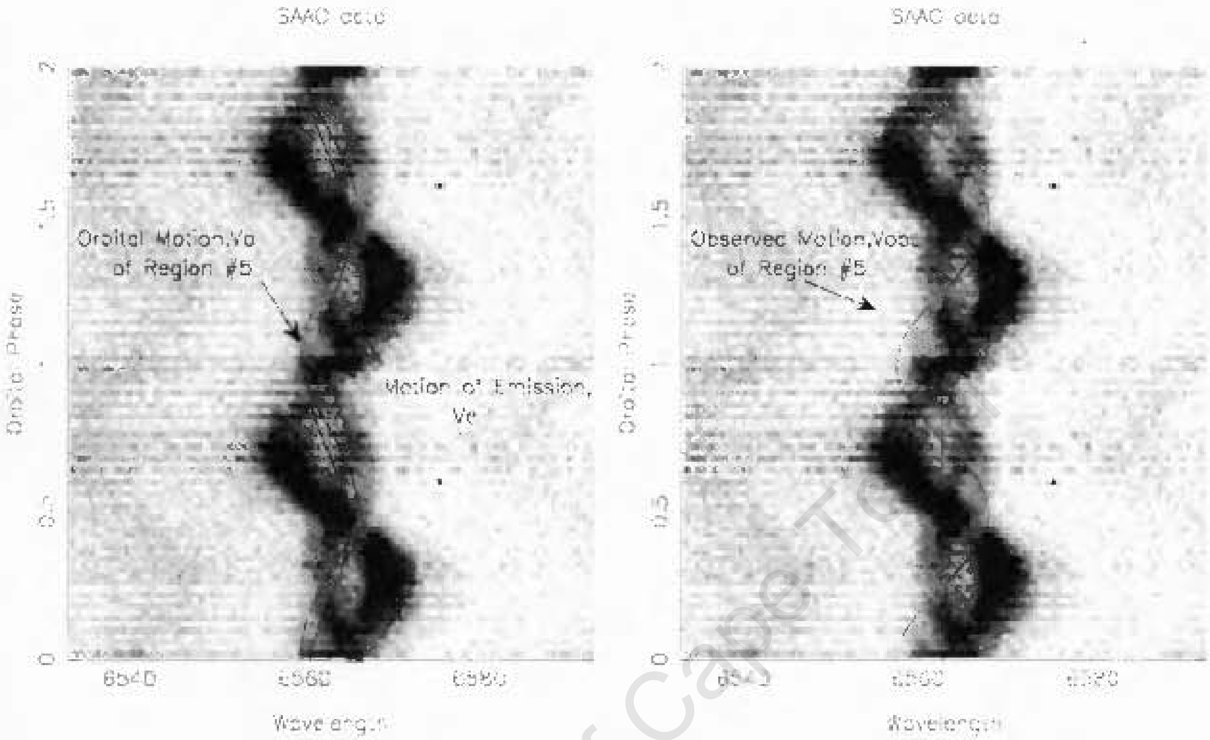

**Figure 18i** 2005 data **Figure 18j**

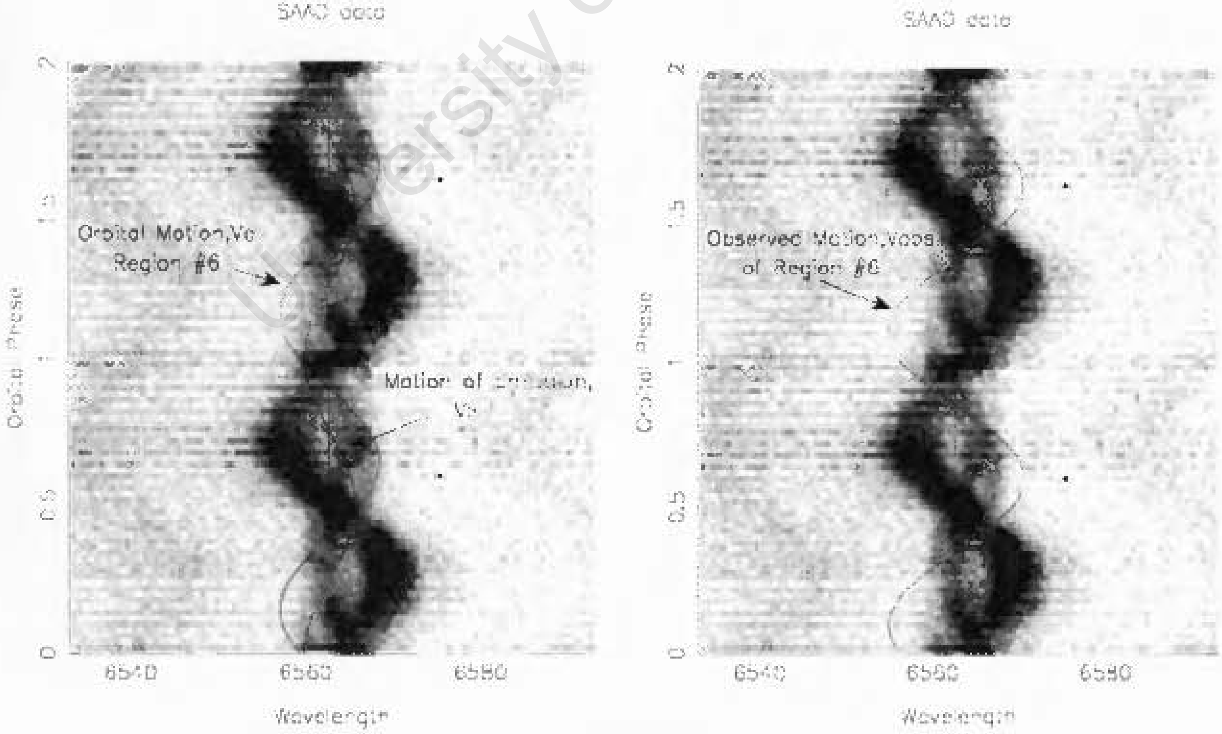

**Figure 18k** 2005 data **Figure 18l**

***Figures 18 – Expected Velocity Curves for Regions 1-6 considering the Binary Orbital Motion and the Motion of any Emission due to Impact from a Ballistic Trajectory, left, and on the right is the Sum of the two giving the motion expected from Observation.***

The interpretation of motion of emission from regions #5 and #6 needs a careful look as these are the only regions whose expected emission velocities are within the range of observed velocities.

As these regions represent peaks, or turning points of the path of the trajectory stream, there is a range of velocities which must be considered around this apex. This variation in velocities can amount to as much as 50km/sec in region #5, and, as their direction is rapidly changing, the velocity of maximum displacement, $K_e$, would also be shifted, thereby affecting the phase.

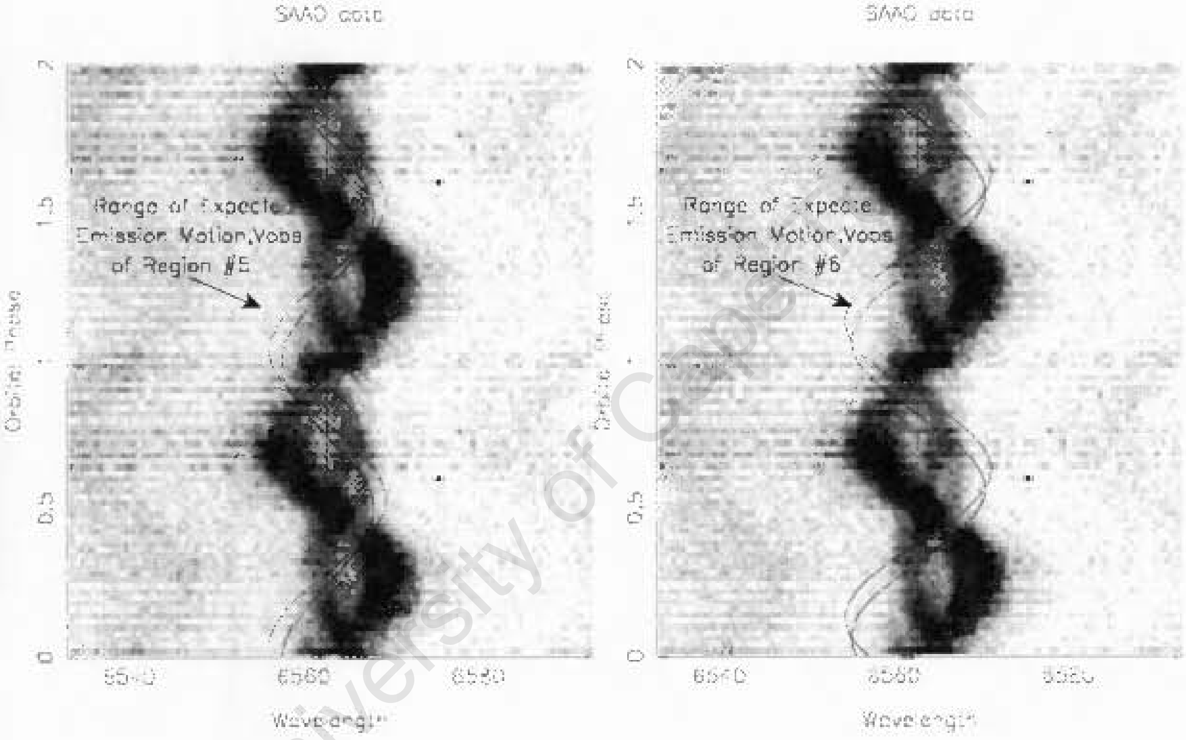

***Figure 19a*** **2005 data** ***Figure 19b***

***Figures 19 – Represent the Binary Motion for a Range of Expected Emission Velocities emanating from Regions #5 and #6.***

In the plots in Figure 19, we have considered the range of velocities around the peak of the trajectory path for regions #5 and #6. We chose this range to coincide with the change in velocity around a limited region surrounding the peak where the ordinate value is at a coordinate maximum and constant. In other words, we hold the y-axis constant at its highest value and look at the change in velocity around this constant value, (see Appendix A, step numbers 755 to 840 for the range for region #5).

There does not appear to be a match between the observed emission and the emission expected from the assumptions expressed in Equ. 18.

# Chapter Seven

## Interpretation of the Data

### 7.1 Results and Discussion

In this chapter we look at all the data that has been obtained so far comparing the observed information with calculations or predictions from modeling of the system.

### 7.1.1 Overlaying the Binary Motions

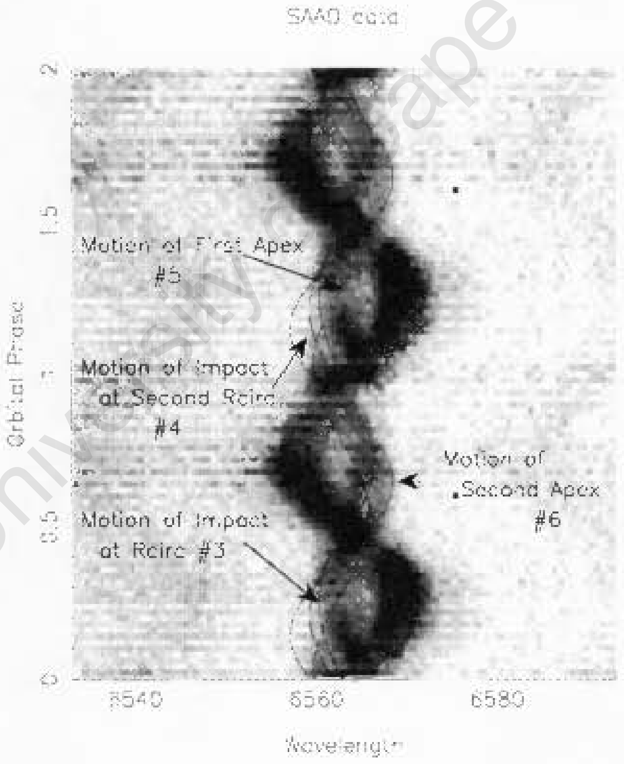

***Figure 20 - Overlay of the paths for Orbital Motion of the most likely Impact Regions 2005 data***

By overlaying the orbital motion of four of the emission regions we can account for much of the observed emission between phases 0.25 and 1.0. Although there is no satisfactory fit to the observed data, it does allow for an explanation for some of the emission, such as the extended emission in the blue at eclipse or phase 1.0, (see section 4.3 p. 43).

There are, though, at least two regions which have not been accounted for. The most obvious is the curious feature discussed again in section 7.1.3, which appears in the first few phases after eclipse. The second appears during the first quarter of the orbital cycle, phase 0.0 to 0.25, where the motion of the second apex regions #6 does not appear to match with any of the observed emission, and indeed looks like a sore thumb to the overall fit.

Although the orbital motion of the emission regions appear to correspond generally to the observed emission, the plots in Figure 20 do not satisfactorily explain the observed motion of the emission. Aside from a generally poor detailed fit, there is no account taken of the streaming motions, which, when considered and plotted as in Figures 19, show little similarity to the observed emission velocities.

### 7.1.2 Velocities

The velocities expected from observation for a variety of the selected impact points are in the range of 500km/sec to over 1000km/sec, yet the range of the observed emission is less than 300km/sec.

The observed motion of some of the emitting gas is consistent with the orbital motion of the most likely impact regions about the centre-of-mass, for instance region #3, but NOT consistent with any additional motion generated from streaming or ballistic velocities as predicted from modeling of the mass-transfer trajectory stream.

The data does help to explain some of the observed emission, yet the curve 'fit' is not unique. Variations of Keplerian motion, unrelated to the likely emission regions #1 to 6, could also account for much of the observed motion, (for example see Figures 21a and 22b).

The absence of higher intensity emission at critical points, e.g. regions #3 to #6, when compared to other less likely emission regions of the trajectory path, indicate that the mass -transfer, if any, is either of low density, intermittent, obscured, or perhaps not emitting in H$\alpha$.

In this system, the lack of an observable 'bright spot' or double peaked Doppler spectra indicates that it is unlikely that there is a viscous disc.

The disc-stream velocity impact model does not help to explain the observed velocities.

If there is mass-transfer following a trajectory path and if there is emission from one or more of the most likely impact regions #1 to #6, then what causes the emission regions to have an observed Keplerian motion around the binary center-of-mass yet no evidence for higher velocities arising from the ballistic motion?

### 7.1.3 "Force Fitting" the Emission Feature

In this subsection we attempt to answer the question "What location in the binary has an orbital velocity curve consistent with the observed emission?"

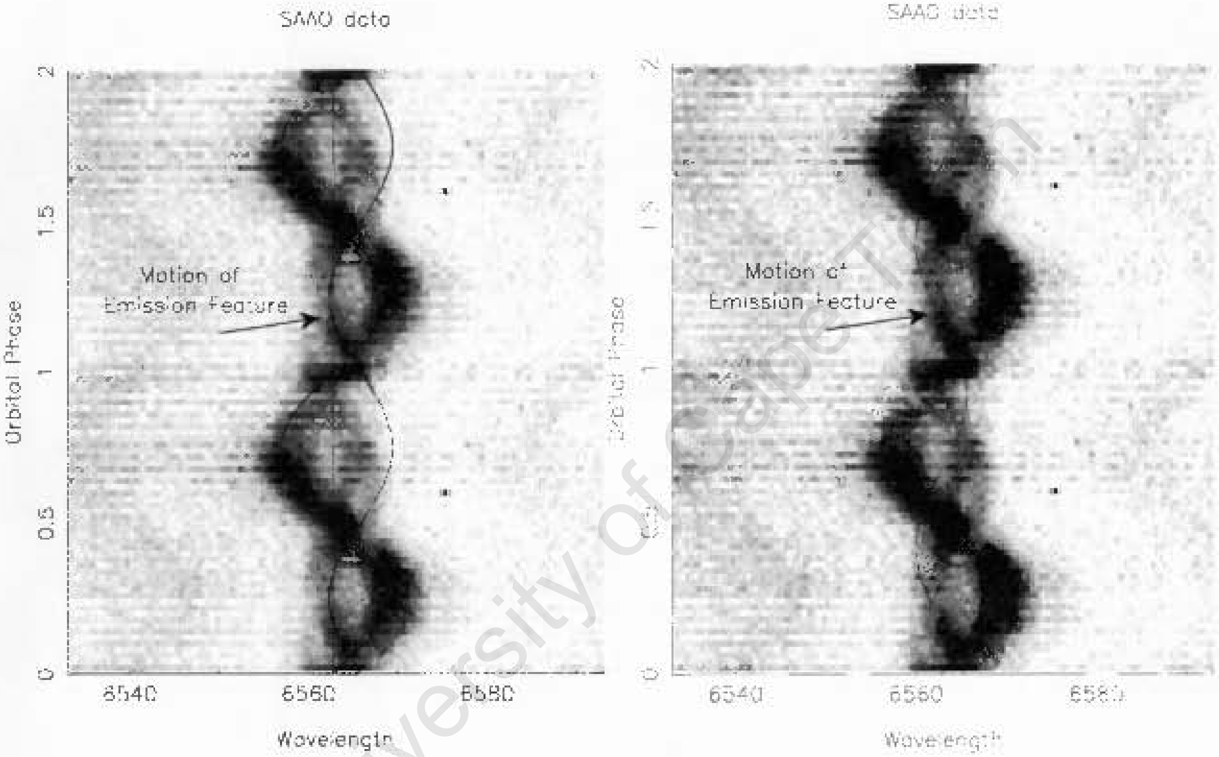

***Figure 21a*** ***Figure 21b***

***Figures 21a and 21b – Possible Motion of the 'Curious Emission Feature (2005 data)***

Curves showing two possible scenarios of binary motion for the emission observed during the phase interval (0.0-0.25) and again repeated between (1.0-1.25) are shown in Figure 21.

It is difficult to ascribe a fixed spatial position in the binary for the curves in Figure 21.

For instance, much of the motion in Figure 21a appears in the red. This translates into almost zero relative motion at phase 0.25 and over 200km/sec at phase 0.75. It is difficult to find a position in the binary where the emission begins in the red, shows near zero relative motion for much of the first half phase and then climbing emission velocities again in the red, in the second half of the phase cycle, 0.5-1.0.

The motion in Figure 21b, although fitting to the curious emission feature, doesn't match well with the data at other orbital phase angles. As the emission begins in the red and moves to the blue it might be generated in the region shown by the 'x' in Fig 21c. There is no plausible physical explanation as to why there might be emission from this region.

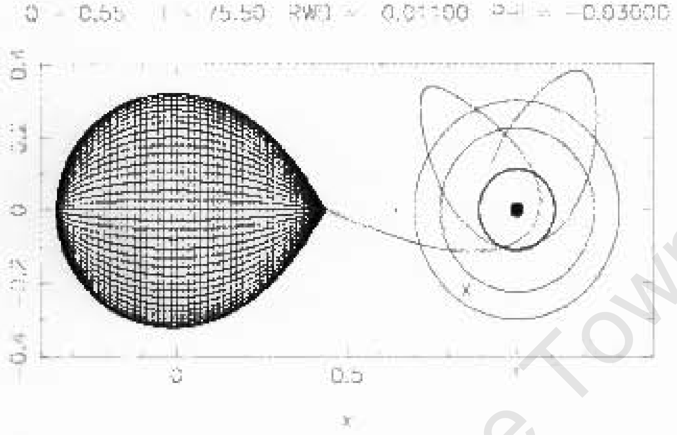

*Figure 21c: Possible position for the Emission Curve referred to in Figure 21b*

Without an explanation as to how there might be emission from this region one must consider the possibility that the emission has some streaming motion relative to the binary. This could place its spatial location in any number of regions within the WDRL.

### 7.1.4 Regularly Observed Features

Comparing the trailed spectral plots from different observation periods indicate that there can be a high degree of variability of emission characteristics. There are, though, a number of regular features apparent in the spectral plots including:

1. The curious but strong WDRL emission feature in the orbital phase interval after eclipse, 0.0 to 0.25.
2. The highest intensity emission of the binary system occurring at orbital phase 0.5.
3. Lower overall WDRL emission intensities in the first half of the orbital cycle
4. Reduction of RD emission during phases 0.38 to 0.44 and 0.02 to 0.08

#### 7.1.4.1 The Emission Feature in the Interval 0.0 to 0.25

The curious emission feature in this phase interval presents a problem in understanding and describing the origin and nature of the observed emission sources. Its source is not obvious and does not appear to originate from any likely emission regions.

It is a region of high relative intensity comparable to that of the RD although less than the brightest emission in the system, that of the emission during orbital phase 0.5.

Looking at the binary path of region 6, there are very low levels of observed emission after eclipse and in the phase interval 0.0 to 0.3. This is in contrast to the phase interval 0.3 to 1.0 or until the next eclipse where the motion of region 6 can account and is consistent with some of the emission. For this initial phase interval there appear to be no emission at these velocities or perhaps the emission is there but obscured by some form of intervening gas.

Yet, if there were intervening gas then the emission from the "curious emission feature" during phase interval 0.0 to 0.25 would also be somewhat obscured.

The existence of this anomaly needs explanation or else the model for the emission of this system could be missing a vital component which could turn the current lack of understanding further on its head.

### 7.1.4.2 The Emission Intensity at Orbital Phase 0.5

The most intense emission occurs at orbital phase 0.5, see Figure 22. This emission is more intense than during eclipse and shows up, in H$\alpha$, as the strongest emission of the system.

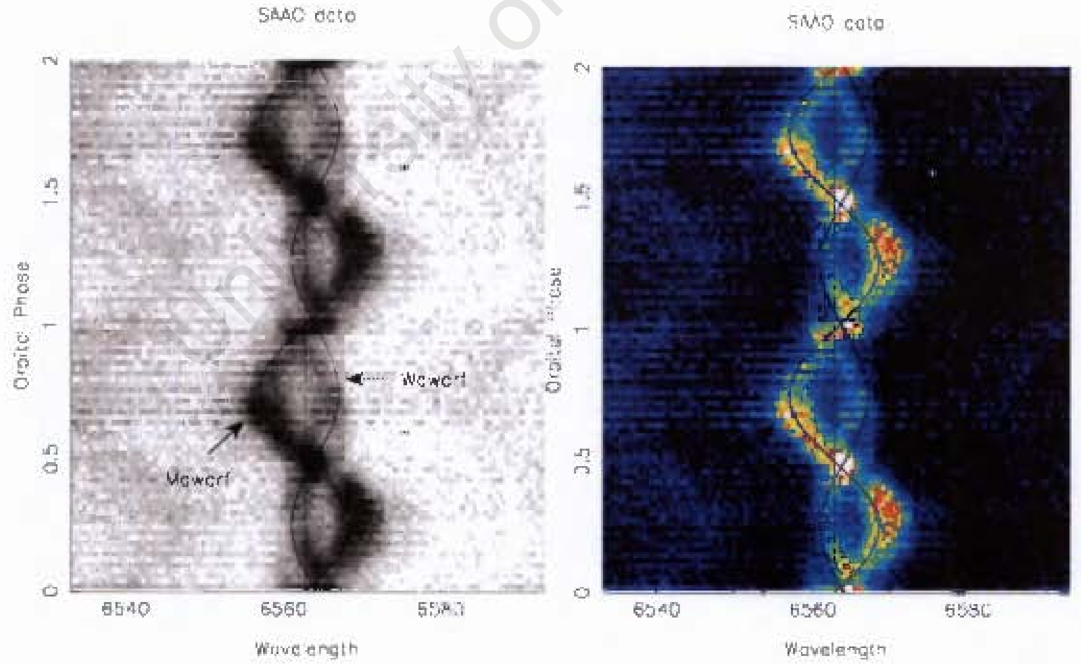

***Figure 22 - Illustration of the high intensity emission region at phase 0.5. Both plots show the highest intensity region emitting above 2.5 relative to the continuum at 1.0. These are shown in black on the left and white in the colour plot. (2005 data)***

This higher relative intensity at phase 0.5 most probably arises from the combination of emission from both the RD and the WD.

The WD is too small in comparison to the RD to cause much obstruction to its signal, but the WD Roche lobe has regions of intervening gas and as the lobe is larger than that of the RD one might expect some absorption of the signal.

In order to confirm the absorption of signal we look at four spectra. Figure 23a shows the cumulative and normalized spectrum at phase 0.5 when both the RD and WD are along the line-of-sight. Figure 23b shows the cumulative and normalized spectrum for eclipse or phase 1.0. Similarly, Figures 23c and 23d show the same cumulative and normalized spectra for the two quadratures, or orbital phases 0.25 and 0.75, respectively. These show the expected double peaked profile showing the Doppler shifted emission from the Roche lobes of each star.

Based on the summation of the two signal levels at orbital phases 0.25 and 0.75, we would expect to observe intensity levels in excess of 2.8 at orbital phase 0.5. Yet, at these phases the overall RD emission intensity is reduced when compared to that at eclipse.

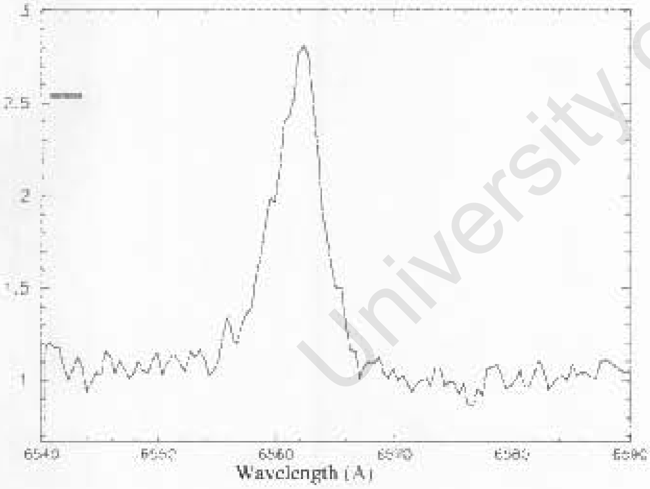

*Figure 23a – Orbital Phase 0.5*

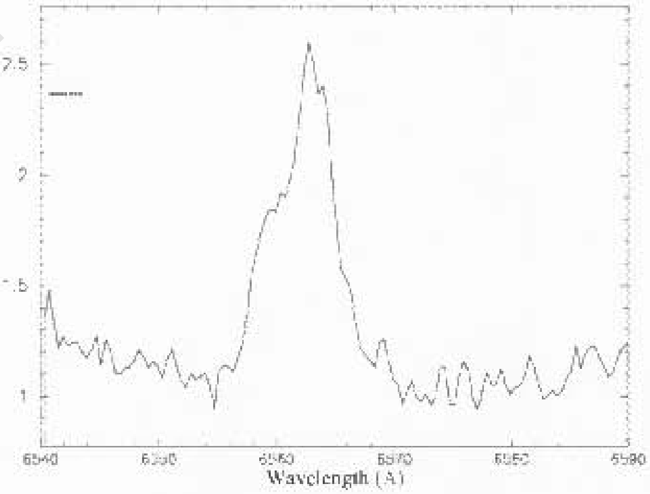

*Figure 23b- Orbital Phase 1.0*

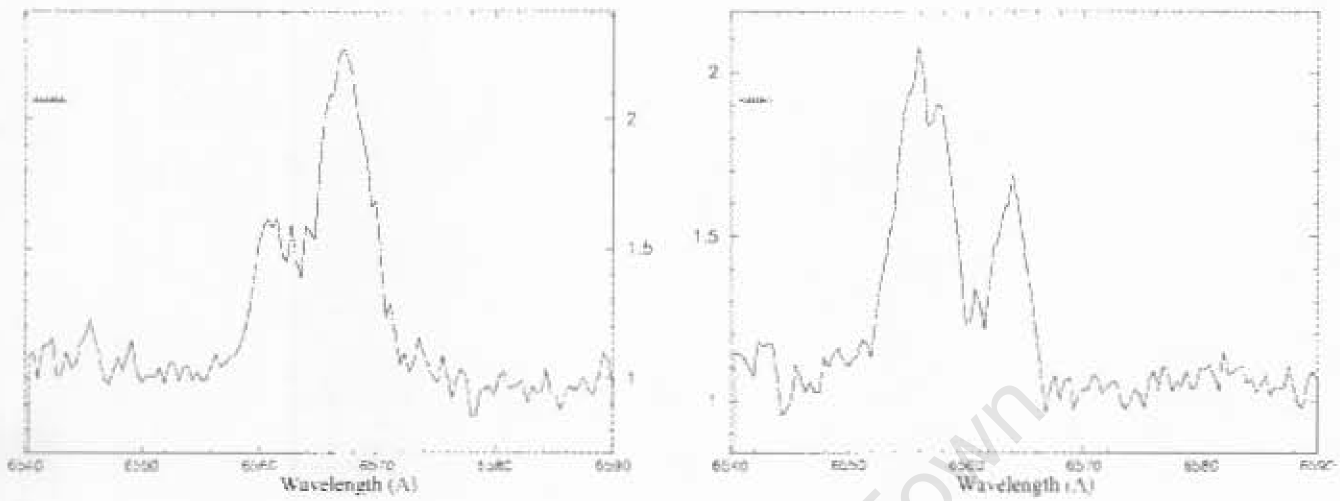

*Figure 23c – Orbital Phase 0.25*

*Figure 23d – Orbital Phase 0.75*

***Figures 23 – Spectra which Highlight the Relative Intensities of the two Stars. Eclipse, shown in 23b, gives an indication of the RD emission intensity, the two Quatratures, 23c and 23d, give the emission intensity for both Stars, and second Conjunction, 23a, gives the Total combined emission for the two Stars. (The Ordinate represents the intensity normalized to the continuum and the Abscissa represents the wavelength range.)***

The 0.2 difference in intensity between eclipse (phase 1.0) and the second conjunction (phase 0.5) is lower than expected. The drop in signal strength during both quadratures when compared to eclipse is perhaps another indication of signal absorption. This is consistent with absorption of signal from intervening gas and further supports that there is absorbing gas in the WD Roche lobe.

### 7.1.4.3 The Lower Velocities of the first half of the Orbital Cycle and Phase Independent Emission

There is a clear reduction in the observed WDRL emission velocities in the first half of the orbital cycle of between 50 and 75km/sec compared to those in the second half of the cycle.

**Low Intensity Phase Independent Emission**

There is another apparent feature in the trailed spectral plots which only shows up at lower contrasts.

At the tip of the arrow pointing to the WD, in Figure 24, there appears an almost vertical straight line of low emission. It forms a clear boundary to the emission in the second half of the orbital cycle at about 6568 Å. The first half of the orbital cycle also shows a vertical line at about 6559.5 Å.

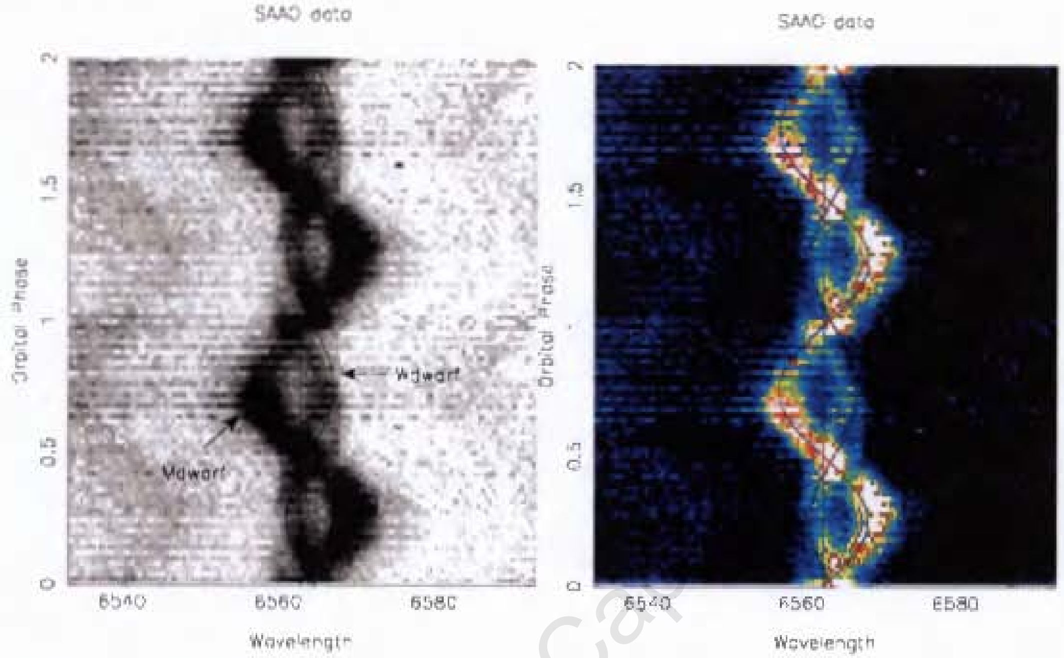

*Figure 24a - Low Contrast Trailed Plots highlighting an Emission Band of Velocities (2005 data)*

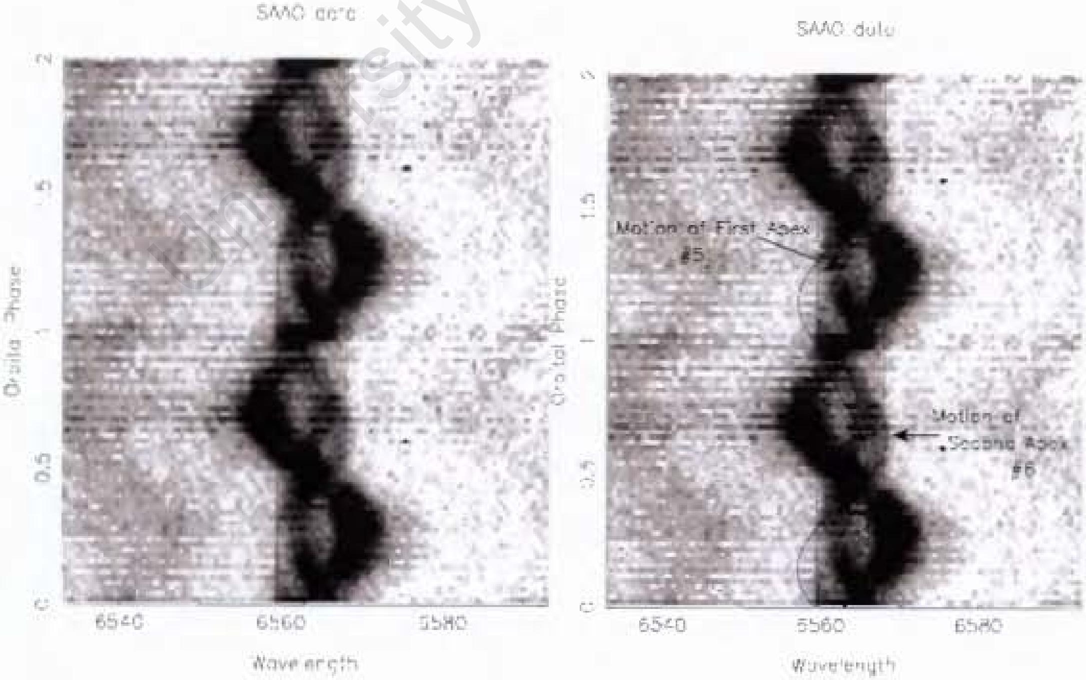

*Figure 24b - Borders delineating Low Intensity Phase Independent Emission Features Central line denotes the H$\alpha$ rest wavelength, 6562.8 Å. (2005 data)*

There is an asymmetry to the velocities on either side of the rest wavelength. The approaching blue emission has a maximum velocity of around 175km/sec and the receding red emission, a maximum velocity of 225km/sec.

I have been unable to identify any location in the individual spectra which might be responsible for this anomaly.

The existence of emission along a straight line, in this space, indicates that there is either emission which is independent of orbital angle when viewed by an observer, or perhaps this is not an observed phenomenon and it relates to noise or some other reason related to equipment.

#### 7.1.4.4 Reduction in the H$\alpha$ Emission from the Red Dwarf

**The H$\alpha$ gap in emission from the red dwarf between phases 0.38 to 0.44, Figure 25**

The distance of the $L_1$ point or chromosphere of the RD to the WD is about 550,000 kilometers or less than 1.5 times the distance between Earth and Moon. Yet, the RD is almost half the size of our Sun (O'Donoghue et al. 2003). From the perspective of the WD, the RD would almost occupy the whole sky. If the emission from the RD has no preferred direction or origin, it is unlikely that the WD, any trajectory stream, a large disc, or any planar structure could entirely block this emission.

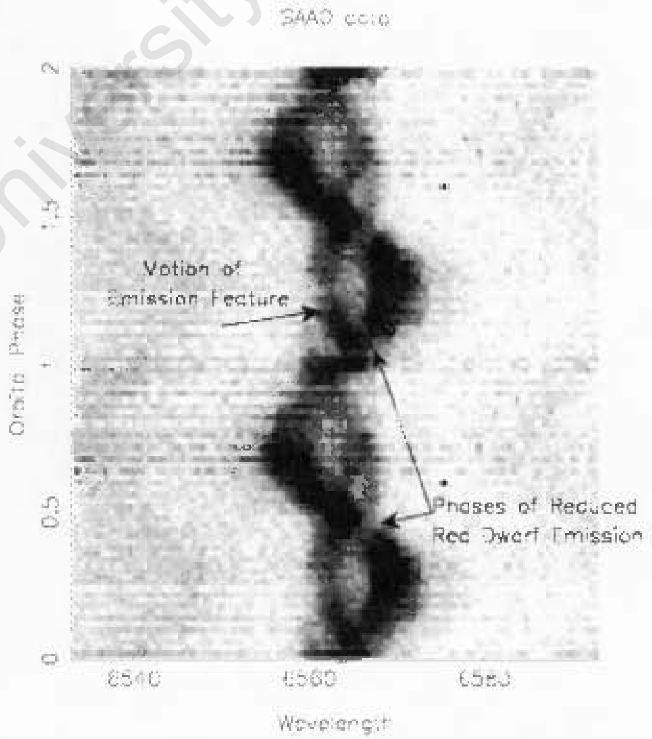

*Figure 25: Spectral Plot showing Regular Features (2005 data)*

The evidence for the existence of such a structure is lacking, and if there were such obscuration, we would expect to observe a reduction in M dwarf emission from other orbital angles.

There is a further possibility that there might be some accumulation of gas or an over-dense region within the WD Roche lobe, and that this region is responsible for the reduction in the observed RD emission. Region #6 is in a position which is, during the phase interval 0.38-0.44, almost in between the observer and the RD along the line-of-sight. If there were an accumulation of gas here it could account for this obscuration.

Yet, there is little evidence for emission from this region and we still would expect such a substantial obscuration of the signal to be detectable from other orbital angles. In addition, this region would have to cover a large expanse of the Roche lobe. It would have to be much larger than the WD, in order to be able to significantly obscure the emission from the RD.

There is also the matter of explaining a similar reduction observed in the RD emission in the early phases after eclipse. From this observation angle the RD is closer to the observer then the WD so there would be little chance of any physical interference.

This lends to the notion that there might be gas diffusing throughout the entire WD's Roche lobe, and that its extent is not limited to a planar topology. Yet, this diffuse but optically thick gas could not be evenly distributed around the Roche lobe as the obscuration is limited to orbital phases 0.38 to 0.44, (see Figure 25), as well as the early phases after eclipse, 0.02 to 0.08, and these do not show any symmetrical equivalent as one would expect , for instance, around phase 0.6.

For completeness, it should be mentioned that the 2004 data does show some reduction in RD emission between phase 0.5 to 0.55, Figure 13b, (p.36), indicating that there might be two phase intervals for reduced RD emission of H$\alpha$. The lack of similar phases of reduced emission in the 2005 data is perhaps an indication of the degree of variability in the optical thickness within the WD Roche lobe.

# Chapter Eight

## Uncertainties and Error

In this chapter we look at the methods used for obtaining the data in an effort to understand its limitations, uncertainties, and error.

### 8.1 Noise

As the spectra are normalized, the noise would be scaled proportionally. For peak amplitudes of 2.8 at orbital phase 0.5 and the continuum defined as unity, the noise around the continuum amounts to peak-to-peak amplitude of around 0.2. Its magnitude is relatively flat around the emission frequency with some excursions outside of this range.

### 8.2 Uncertainty in the Modeled Velocities

The model trajectory shows a steep velocity gradient as matter/gas approaches the WD. This makes it difficult to allocate a velocity to a specific location. The velocity in a single time-step of the trajectory program can change by as much as 200km/sec. This especially applies to regions closer to the WD. For example at $R_{circ}$ the step change nears 100km/sec.

Yet this large uncertainty in the velocity is limited to the high velocity regime so the lower relative velocities away from the WD would be more accurate.

### 8.3 Uncertainty in the Phase Binning of the Data

Ideally we would have liked to have exposure times for each spectrum timed to coincide with the time it takes for the binary system to rotate by 1/50 of a revolution, so that one exposure or spectrum coincides with one phase bin. Unfortunately, this is an ideal and was not attainable in practice.

### 8.3.1 Overlapping of the Phases Bins

In order to collect enough light to maximize the signal-to-noise ratio, each exposure was chosen to last 500 sec, ($8^{m}20^{s}$).

The 500 second exposure time per spectrum would receive light over an angle of 13.82 degrees of the orbital cycle. Yet each orbital phase bin contains data from 7.2 degrees of orbital cycle. This means that each spectrum contains portions of two or even three orbital phase bins of data depending on starting point.

For example, the eclipse lasts about 14 minutes and the procedure by which the software allocates a spectrum to a phase bin is based on the starting time of the exposure.

If, on any given evening, data collection begins, by chance, just after the start of the eclipse then the first 500 second exposure would contain only the eclipse data. The second exposure though would contain six minutes of eclipse and two minutes out of eclipse and into the subsequent phase bin.

Conversely, if data collection began at mid-eclipse the first phase bin would contain 7 minutes of eclipse and 1 minute of data past eclipse, again in the next phase bin. So observations through eclipse could contain various amounts of either eclipse data, data intended for the next phase bin or even the data intended for the previous phase in the cycle.

The process, therefore, takes data and then separates the spectrum into orbital phase bins. As each spectrum covers two phase bins, one orbital revolution of the system would result in only 25 bins being allocated. Therefore, only every second orbital phase would be binned.

On another evening the spectra could again contain data for more than one orbital phase and the binning would proceed as before. This might, though, generate a different set of orbital phase bins than the previous night, say even phases versus odd phases. Then, when combined on the trailed spectral plot the odd set of phase bins would be from one evening and the even set of phase bins could be data from a subsequent evening.

This is clearly not ideal as it would reduce the 50 bin division of the orbital cycle to, effectively, only 25 bins for each revolution within the observation period, and we would have blurring or overlap of each phase bin to the extent of almost one full phase.

### 8.3.2 Allocation of the Phase Bins

Closer inspection of the software used to divide the spectra into orbital phase bins, shows that the bin selection also contributes a mentionable amount of error by the process through which it selects a bin for a given spectrum.

The HJD is read off each spectrum header and allocated to a bin. To do this the program uses the HJD of the mid-eclipse ephemeris divided by the orbital period and then subtracts the result from the HJD from each spectrum. This establishes the bin number to the nearest tenth decimal place. To establish the final bin number, the remainder is rounded up or down to the nearest integer.

This is a problem in that it means that the allocation of each spectrum to a bin can be as much as half a bin out of phase with another spectrum allocated to the same bin.

The total possible error here is essentially one full bin or an overlap covering 7.2° of the orbital cycle. A listing of some of the measured errors is shown in Table 9. It compares a series of two different spectra which have been allocated to the same bin, and then lists the amount of displacement from a perfect overlap of the two spectra. This then establishes the overlap error due to the bin selection.

| Spectrum# | Orbital Phase Angle | Bin (Calculated) | Final Bin Allocation | Overlap Error | Degrees Overlap |
|---|---|---|---|---|---|
| 1 | 0.37785 | 18.89 | 20 | 0.3% | +0.35 |
| 62 | 0.37687 | 18.84 | 20 | | |
| 2 | 0.41785 | 20.89 | 22 | 0.2% | +0.32 |
| 63 | 0.41695 | 20.85 | 22 | | |
| 3 | 0.45793 | 22.89 | 24 | 0.2% | +0.37 |
| 64 | 0.45691 | 22.85 | 24 | | |
| 7 | 0.63951 | 31.98 | 33 | 0.9% | -2.03 |
| 26 | 0.64515 | 32.26 | 33 | | |
| 36 | 0.58423 | 29.21 | 30 | 0.9% | -1.94 |
| 67 | 0.58962 | 29.48 | 30 | | |
| 51 | 0.15493 | 7.75 | 9 | 6.2% | -3.73 |
| 78 | 0.16530 | 8.26 | 9 | | |
| 52 | 0.19493 | 9.75 | 11 | 5.0% | -3.73 |
| 79 | 0.20530 | 10.26 | 11 | | |

***Table 9 - Quantifying the Orbital Phase Overlap Error: The fifth column shows the result of the ratio of orbit angles from spectra with the same calculated bin number, in percent then converted to degrees for the final column.***

## 8.4 Crossing Time Scales

The purpose of this section is to compare the mass-transfer crossing time to the observation exposure time to understand how this might affect the quality of the collected data.

The distance of separation between the two stars is of the order of $10^6$ or 1,000,000km. The $L_1$ point lies approximately 550,000km from the WD, and it takes on the order of $10^3$sec or about 20min for matter to cross from the $L_1$ point to the WD.

The radial extent of matter circulating at $R_{circ}$ is unknown. We would expect that mass transfer would accumulate at or near this radius. If we assume no collisions, and we take the velocity initially crossing $R_{circ}$ on the order of 300km/sec in y and 1100km/sec in the x direction, (see Appendix A).

As matter emerges from the far side of the WD, it crosses $R_{circ}$ a second time. Yet, now its y-velocity is over 1000km/sec and 500km/sec for the x-velocity.

To cross between the entry and exit points of $R_{circ}$ has a distance on the order of the twice $R_{circ}$: 2.0 X $10^8$m or 200000km. With such high velocities the crossing time would be under 200sec.

Finally, if one considers that the matter in transfer takes about 200sec to enter and leave the vicinity of the WD and with the exposure times lasting 500 seconds, at most we would be able to obtain two phases, each covering a partial segment of the trajectory.

This is most limiting in that most of the collisions and hence the emission that is expected to occur near the WD and out to $R_{circ}$ could all be contained within one exposure period.

As we are limited to 92 spectra, we have an average of 2 spectra per phase bin. If the trajectory stream were not constant but rather in 'blobs', different exposures of this region might not contain emission which might further help to explain why there isn't observable emission in expected regions.

## 8.5 Summary of the Procedural Uncertainties

1. Each orbital phase bin contains data not only for next phase but also from either the subsequent and/or previous orbital phase.
2. The allocation of orbital phase bins for an evening of observation would place spectra in at least every second orbital phase bin.
3. There is a measurable time gap after every third exposure to take arc measurements, introducing additional phase bin allocation 'gaps'.
4. There is variation by the process in which the software assigns a given spectrum to a specific orbital phase bin.
5. The observation time did not produce enough spectra to establish statistical significance. Each bin is the cumulative and normalized sum of no more than four spectra with some bins having only a single spectrum and with an average of two spectra per orbital phase bin.

It is my judgment that the procedural uncertainties listed above reduce ones ability to interpret the orbital phase plots with confidence. With only an effective 25 orbital phase bins and a blurring of every phase bin through overlap of the phases, we have sacrificed some of the higher resolution capabilities available for observations.

# Chapter Nine

# Conclusions

**There is no observable high velocity H$\alpha$ emission.**

Based on the data generated from the model trajectory in Chapter 4, we would expect to measure velocities in excess of 300km/sec from a number of the impact regions. The results have been plotted in Figures 19.

The data shows that there is no observable velocity emission above 300km/sec.

In order to be consistent with the high velocities expected from the intense gravitational field of the compact star it would be necessary to have velocities well above those which have been observed. The only emission velocities observed were similar to that expected due to the binary motion of the system.

The question remains as to why there are no observed high velocity emissions. Without observing these emissions, we cannot provide further support for a mass-transfer trajectory stream. Yet, if there are high velocity impact emissions then they might be obscured from observation, or perhaps the nature of the impact collision does not generate observable emission in H$\alpha$. This is plausible in that the gas densities might be low enough to be significantly ionized. Further investigation in this direction might yield some light.

**Is there a disc?**

Any emission during the two crossing of $R_{circ}$ could be produced as a result of the tendency of matter to settle by collisions into a Keplerian orbit.

For any mass-transfer, it is reasonable to consider that any matter generated from $L_1$ and ending up circulating in $R_{circ}$ would accumulate over time. Without sufficient density for interaction, the ring of matter/gas would have no way to spread out radially or accrete onto the WD, except through random events. Whether intermittent or continuous, this accumulation would then at some timescale reach a density sufficient for viscous interaction and the formation of a viscous disc would follow from the radial spreading of matter both away from as well as towards the surface of the WD.

This would then generate the basis for impact emission as well as accretion onto the surface of the WD.

Currently, there is no viscous disc on the basis that there is no 'bright spot' or any obvious double peaked emission profile, which is the standard signature of a disc. There is no clearly observed and regular emission from the WD surface, the sign of accretion.

There is the possibility that some of the mass-transfer could impact along the edge of a diffuse outline of a ring or disc near $R_{circ}$, pass through this disc, cross over the disc, or to continue on its initial trajectory.

**Is there evidence for the existence of a mass-transfer stream?**

There is no distinctly observable impact point along the trajectory path that clearly defines a specific region of impact emission. There is no observable emission at the velocities expected from the combination of orbital as well as ballistic motions of a mass-transfer trajectory stream.

There are, though, regular emission features, so there must be regular collisions of gas or matter in regions which are constant in the frame of the binary.

Optical thickness of the intervening gas might explain how, from some angles, there could be indication of regular structure to the emission characteristics yet no confirmation for other orbital angles.

The fitted curves for the binary motion are consistent with much of the emission, yet, they are not unique and there are emission velocities which do not 'fit' with these curves. The failure to account for the curious but intense emission feature shown in Figure 26 is still an issue and no explanation has been found for its appearance.

We can neither confirm nor deny the existence of a mass-transfer stream. All we can say is that we have not observed conclusive evidence of its existence.

**Has there ever been a disc?**

What is the evolutionary history of this system? The RD is not an evolved star as it lies on the lower main sequence. The WD has a high rotational velocity which might come, to some extent, from surface accretion. For non-magnetic systems, accretion would arise from the loss of angular momentum from matter or gas in a viscous disc. As the existence of a disc requires mass transfer for its formation, is this evidence that there might have been mass transfer and a disc in the past?

If this is so, why then did the mass-transfer cease? Did it reduce slowly on an evolutionary timescale or did it stop through some more dramatic incident?

The surface temperature ($T_{eff}$) of the WD is typical of systems below the period gap, yet we find this system just above this gap.

Perhaps the RD magnetic braking mechanism changed due to some internal adjustment within the star, causing the cessation of mass-transfer. Alternatively, perhaps what we are observing is a system which released energy in powerful nova outbursts, irradiating the secondary, increasing the distance of separation of the stars and propelling the system up through the period gap to its current position….a hibernating cataclysmic variable binary star system.

The system has continued to evolve and might have already adjusted to its change of circumstances as magnetic braking or gravitational radiation might have brought it to the brink of revival. Perhaps what we are witnessing are signs of the initial stirrings of mass-transfer.

Alternatively, there is a finite possibility that this system is coming into contact for the first time and that what we are observing are the first signs of mass-transfer.

Whichever the case, the remnants of a disc could still be there

### Variation is intrinsic in this binary system.

Figure 14 shows that there has been a significant change in the WDRL emission over a period of one year. It is unclear, though, whether this clear lack of signal is due to a change in any flow of mass-transfer or a shift in the optical thickness over the region. The drop in signal is evident from other orbital phases.

We know that there are some persistent features and some variable features of the WDRL $H\alpha$ emission. There is also the possibility that the WDRL $H\alpha$ emission does not come from Roche lobe overflow through $L_1$ in the traditional way. Instead the gas might have transferred from the RD in a wind, or in flare-related jets, arising from chromospheric activity n the RD.

### Can the WDRL emission be due to chromospheric emission from the WD?

The cool magnetic white dwarf GD356 (Teff= 8 x $10^3$ K; magnetic field strength B= 1.5 x $10^6$ G) is the only apparently single magnetic white dwarf known with emission lines. It shows resolved triplets of $H\alpha$ and $H\beta$ as emission lines (Greenstein & McCarthy 1985). A non magnetic white dwarf would simply have Balmer emission which is not Zeeman split. There is no evidence for an interacting companion star: the data can be explained as emission from a thin layer of high-density ionized gas (i.e., a chromosphere). This possibility would need further investigation which is beyond the scope of this paper.

### Concluding Remarks

**1.0** Based on the accumulated information and analysis so far of EC13471-1258, one can envision a system in which matter/gas from the highly active RD is regularly and frequently crossing into the vicinity of the WD Roche lobe. With mass ejections, flaring activity, and a stellar wind with its underlying charged plasma permeating the local space, the RD has much in its arsenal.

There would also be events whereby matter from the RD embarks on a trajectory, not restricted to the orbital plane and not generated from the $L_1$ point, into or through this WD Roche lobe. Some of the debris will become trapped into the gravitational potential well of the WD and begin to orbit the star.

Over time and as a result of random collisions the gas might settle into a regular Keplerian orbit, not necessarily $R_{circ}$, or its orbit might even remain somewhat elliptical. As time progresses further and additional events take place, there might be some form of accumulation of matter/gas in a region other than those previously chosen on the basis of the existence of a mass-transfer.

**2.0** We further have to ask ourselves whether the assumption that the RD Roche lobe is filled to its capacity and whether its extent, assumed to be comparable to the radius of the star, is a valid assumption.

The results of this paper cannot provide additional support for the existence of mass-transfer and without this, the assumption that "its cup runneth over … just", O'Donoghue et al. (2003) cannot be further validated. This is quite crucial as it provides support for one of the constraints by which the mass-radius relation and inclination angle is determined for this system.

## Future Work: Improving the Observations and the Analysis

The data and analysis so far are insufficient to further clarify this binary picture and better data collection and analysis techniques are required. A higher signal-to-noise ratio would assist and more accurate binning with minimal signal overlap is necessary to further unravel the mystery of the $H\alpha$ emission sources.

### Producing a Tomogram

A tomogram is an indirect imaging method based on atomic line emission. Tomography refers to the process of constructing a spatial distribution of physical quantity given measurements that are essentially line-integrals or projections through the distribution. The line profile retains an imprint of the distribution of emission. The formation of the line profile is a form of projection, with the 2-dimensional emission distribution giving a 1-dimentional profile as a function of radial velocity (component of velocity along line-of-sight) (Marsh and Horne 1988).

Relative to the binary, the lines of projection rotate, and so by observing multiple orbital phases, we obtain the equivalent of the multiple projection angles used in medical tomography.

The tomogram uses images from different phase angles to reconstruct the spatial distribution and position of an object. One generally requires at least 20 angles to build up an accurate image.

In our case, the data contained in different bins is not only smeared by the overlap, as described previously, but there is also variability from intervening gas. In addition, a recommended signal to noise ratio of about 50 is advised (Marsh and Horne 1988) when we were only able to obtain a s/n ratio of 25. With all this in mind, attempting to reconstruct the spatial positions of the emission using this technique would still probably be useful and may provide additional information. I am rather skeptical though due to the variability of the optical thickness which would distort the emission information gathered along the orbital motions.

### Improving the Observations

The most obvious way to improve the observations is to use SALT[1] for about 4 hours per night for three or four nights... With the collecting power of its 10 meter dish, the exposure time would be reduced by at least an order of magnitude, substantially increasing temporal resolution, and the signal-to-noise would be increased to well in excess of 50.

With such short exposure times all the problems associated with the misalignment of phases and the high velocity gradients would be greatly reduced. A less than 50 second exposure time would allow for some 200 spectra per four hour session. The alignment of the phases could be carefully monitored during the session and the number of bins allocated could be doubled to improve the resolution as well as to reduce the round-off error in the bin allocations.

This would go a long way to fully understanding the locations of these emission sources.

---

[1] **South African Large Telescope**

# References

Allard N.F., Koester D. 1992, *A&A*, **258**, 464.

Andronov N., Pinsonneault M., Sills A. 2003, *ApJ*, **582**, 358

Augusteijn et al. 1996, Astronomy & Astrophysics, **311**, 889.

Chandrasekhar, S. 1939, *An Introduction to the Study of Stellar Structure*, Univ. Chicago Press, Chicago.

Clemens J.C., Reid I.N., Gizis J., O'Brian M.S. 1998, *Astrophys. J.*, **496**, 352.

Eggleton P.P. 1983, *Astrophys. J.*, **268**, 368.

Ferland, G.J., Lambert, G.L., McCall, M.L., Shields, G.A. & Slovak, M.H. 1982. *Astrophys. J.*, **260**,794.

Finley D.S., Koester D., Basri G. 1997, *Astrophys. J.* , **488**, 375.

Flannery B.P. 1975, *Mon. Not. R. Astr. Soc.*, **170**, 325-331.

Frank J., King, A.R., Raine, D. 1992 *Accretion Powers in Astrophysics*, Third edition, Cambridge University Press.

Gaensicke B.T., et al. 2004, *Astro-ph.*, 0402189

Greenstein J., McCarthy J. 1985, *Astrophys. J.*, **289**, 732.

Hawley J.F., Balbus S. A. 1998, *ASP Conf*, **137**, 273.

Hellier C. 2001, *Cataclysmic Variable Stars How and Why They Vary*, Springer-Praxis, Chichester.

Horne K. 1986., *PASP.*, **98**, 609-617.

Horne K.M., Marsh T.R., Cheng F.H., Hubeny I., Lanz T. 1994, *Astrophys. J.*, **426**, 294.

Hut P. 1981, *Astr. Astrophys.*, **99**, 126.

Kawka A., Vennes S., Koch R., Williams A. 2002, *AJ*, **124**,2853.

Kawka A., Vennes S., 2003, *AJ*, **125**, 1444-1447.

Kilkenny D., Koen C., O'Donoghue D., Stobie R.S., 1997, *MNRAS*, **285**, 640 (Paper I)

King A.R. 1988, *Quart. J. Roy. Astr. Soc.*, **29**, 1.

Kippenhahn R. 1981., *Astr. Astrophys.*, **102**, 293.

Koen C. 1996, *Mon. Not. R. Astr. Soc.*, **283**, 671.

Kolb U., Baraffe I. 1999 *MNRAS*, **309**, 1034

Kovetz A., Prialnik D., & Shara, M.M. 1988, *Astrophys. J.*, **325**, 828.

Livio M., Shara M.M., 1987, *Astrophys. J.*, **319**, 819-826.

Lubow S.H., Shu F.N. 1975, *Astrophys. J.*, **198**,383.

Marsh T.R., Horne K.D. 1988, *Mon. Not. R. Astr. Soc.*, **235**, 269.

Marsh T.R., et al., 1990, *ApJ*, **364**, 637.

O'Donoghue D., Koen C., Kilkenny D., Stobie R.S., Koester D., Bessell M.S., Hambly N., MacGillivray H. 2003, *Mon. Not. R. Astr. Soc.*, **345**, 506.

Pinsonneault M.H., Andronov N., Sills A. 2002, ASP Conf. Ser. 261, 208-216

Rappaport S., Verbunt F. & Joss P. 1983, *Astrophys J.*, **275**, 713

Reid I.N., Hawley S.L. 2000, *New Light on Dark Stars: Red Dwarfs, Low-Mass Stars, Brown Dwarfs*, Praxis, Chichester.

Ritter H. 1976, *Mon. Not. R. Astr. Soc.*, **175**, 279.

Ritter H., Schroder R. 1979, *A&A.*, **76**, 168.

Robinson E.L., Barker E.S., Cochran A.L., Cochran W.D. & Nather R. E. 1981, *Astrophys. J.*, **251**, 611.

Savonije G.J. & Papaloizou J.C.B. 1985, in *Interacting Binaries*, eds. P.P.Eggleton &

J.E. Pringle, Reidel, Dordrecht. P.83.
Shara,M.M., Livio M., Moffat A.F.J., & Orio M. 1986, *Astrophys J.*, **311**, 163
Sills A., Pinsonneault M.H., Terndrup D.M. 2000, *ApJ.*, **534**, 335
Schenker K., King A.R. 2002, ASP Conf. Ser. 261, 242-251
Spruit H.C. & Ritter H. 1983, *Astr. Astrophys.*, **124**, 267
Stobie R.S., et al. 1997, *Mon. Not. R. Astr. Soc*, **287**, 848.
Szkody P., Sion E.M., Gansicke B., Howell S.B. 2002a, *The Physics of Cataclysmic Variables and Related Objects*, ASP Conference Series, **261**, 21.
Taam R. E., Ivanova N. 2003, *Astrophys. J.*, 599, 516-521
Tonry J., Davis M. 1979, *AJ*, **84**, 1511.
Uemura M. 2004, RevMexAA (Serie de Conferencias), **20**, 109-110.
Unsold A. 1968 *Physik der Sternnatmospharen*, Springer-Verlag Berlin, Heidelberg, New York, p.508.
Wang Y.-M. 1987, *Astr. Astrophy.*, **183**, 257.
Warner B. 1995, *Cataclysmic Variable Stars*, Cambridge University Press, Cambridge.
Warner B., Peters W.L. 1972, *Mon. Not. R. Astr. Soc*, **160**, 15-20.
Weber E., Davis L. 1967, *Astrophys. J.*, **148**, 217
Webbink R.F. 1979b, *Int. Astr. Union Colloq.*, **53**, 426.
Wood B.E., Muller H-R., Zank G.P., Linsky J.L. 2002, *Astrophys. J.*
Wood M.A. 1995, *Lecture notes in Physics, Vol. 443: White Dwarfs*, 41.
Zahn J.-P. 1966, *Ann. D'Astrophys.*, **29**, 489.

# Appendix A

## Model Calculation of the Velocities in a Trajectory Stream

---

### Value of q = 0.5513 : Value of i = 75.50 : Value of phi = 0.03

See Figure 16 page 43 for a diagram of the trajectory.

Velocities are in km/sec.

M refers to the step number.

X,Y refer to the coordinate positions where the origin is at the centre of the RD secondary.

VX,VY refer to the components of the trajectory velocity, VR, in the binary frame of reference.

R1,R2 are the distances of the particle to the two stars, respectively.

THETA is the angle subtending the line joining the WD centre to the position of the particle and the line joining the two stars.

VR is the radial velocity in the frame of the observer.

VXTOT,VYTOT refer to the components of the trajectory velocity in the frame of the observer.

```
  M    X    Y      VX      VY    R1    R2    THETA      VR     VXTOT  VYTOT
-------------------------------------------------------------------------------
  0 0.44 0.00  12.1    0.0 0.56 0.44
  5 0.44 0.00  12.3   -1.2 0.56 0.44  -179.99    12.36   12.3  -83.4
 10 0.44 0.00  12.9   -2.4 0.56 0.44  -179.97    13.13   13.0  -84.0
 15 0.44 0.00  13.9   -3.7 0.56 0.44  -179.93    14.40   14.2  -84.6
 20 0.45 0.00  15.4   -5.0 0.55 0.45  -179.87    16.19   15.9  -85.2
 25 0.45 0.00  17.4   -6.5 0.55 0.45  -179.80    18.52   18.1  -85.8
 30 0.45 0.00  19.9   -8.0 0.55 0.45  -179.70    21.44   21.0  -86.4
 35 0.45 0.00  23.1   -9.7 0.55 0.45  -179.59    25.05   24.7  -87.0
 40 0.46-0.01  27.1  -11.6 0.54 0.46  -179.45    29.45   29.2  -87.7
 45 0.46-0.01  32.0  -13.7 0.54 0.46  -179.28    34.80   34.7  -88.3
 50 0.46-0.01  38.0  -16.1 0.54 0.46  -179.08    41.28   41.5  -89.0
 55 0.47-0.01  45.3  -19.0 0.53 0.47  -178.83    49.11   49.7  -89.8
 60 0.48-0.01  54.2  -22.3 0.53 0.48  -178.54    58.58   59.6  -90.6
 65 0.48-0.02  64.9  -26.2 0.52 0.48  -178.19    70.01   71.5  -91.6
 70 0.49-0.02  77.9  -30.8 0.51 0.49  -177.76    83.81   86.0  -92.6
 75 0.50-0.02  93.7  -36.3 0.50 0.50  -177.23   100.49  103.4  -93.8
```

```
  M    X    Y       VX      VY    R1    R2    THETA      VR     VXTOT   VYTOT
-----------------------------------------------------------------------------


 80  0.51-0.03  112.8  -42.8  0.49  0.52   -176.58    120.67   124.5   -95.2
 85  0.53-0.03  136.1  -50.5  0.47  0.53   -175.77    145.15   150.1   -96.7
 90  0.55-0.04  164.5  -59.5  0.45  0.55   -174.74    174.95   181.3   -98.2
 95  0.57-0.05  199.6  -69.9  0.43  0.57   -173.41    211.50   219.6   -99.6
100  0.60-0.06  243.5  -81.6  0.41  0.60   -171.65    256.78   267.2  -100.2
105  0.61-0.06  267.5  -87.2  0.39  0.62   -170.64    281.34   293.2   -99.9
110  0.62-0.06  273.1  -88.5  0.39  0.62   -170.40    287.04   299.2   -99.8
115  0.62-0.07  278.8  -89.7  0.39  0.62   -170.15    292.89   305.4   -99.7
120  0.62-0.07  284.7  -90.9  0.38  0.63   -169.90    298.88   311.7   -99.5
125  0.63-0.07  290.8  -92.2  0.38  0.63   -169.64    305.02   318.3   -99.3
130  0.63-0.07  297.0  -93.4  0.38  0.63   -169.36    311.32   324.9   -99.0
135  0.63-0.07  303.4  -94.6  0.37  0.64   -169.08    317.78   331.8   -98.8
140  0.64-0.07  309.9  -95.8  0.37  0.64   -168.79    324.41   338.9   -98.4
145  0.64-0.07  316.7  -97.0  0.37  0.65   -168.49    331.22   346.1   -98.0
150  0.65-0.07  323.7  -98.1  0.36  0.65   -168.17    338.21   353.5   -97.6
155  0.65-0.08  330.8  -99.3  0.36  0.65   -167.85    345.40   361.2   -97.1
160  0.65-0.08  338.2-100.4  0.35  0.66   -167.51    352.78   369.1   -96.6
165  0.66-0.08  345.8-101.5  0.35  0.66   -167.16    360.38   377.2   -95.9
170  0.66-0.08  353.6-102.6  0.35  0.67   -166.80    368.19   385.5   -95.3
175  0.67-0.08  361.7-103.6  0.34  0.67   -166.42    376.24   394.1   -94.5
180  0.67-0.08  370.0-104.5  0.34  0.68   -166.03    384.52   403.0   -93.6
185  0.68-0.08  378.6-105.4  0.33  0.68   -165.62    393.05   412.1   -92.6
190  0.68-0.08  387.5-106.3  0.33  0.69   -165.19    401.85   421.5   -91.6
195  0.69-0.09  396.7-107.0  0.33  0.69   -164.75    410.93   431.3   -90.4
200  0.69-0.09  406.3-107.7  0.32  0.70   -164.28    420.30   441.3   -89.1
205  0.70-0.09  416.1-108.3  0.32  0.70   -163.80    429.98   451.7   -87.6
210  0.70-0.09  426.3-108.8  0.31  0.71   -163.29    439.99   462.5   -86.0
215  0.71-0.09  436.9-109.2  0.31  0.71   -162.77    450.35   473.6   -84.2
220  0.71-0.09  447.9-109.4  0.30  0.72   -162.21    461.07   485.1   -82.2
225  0.72-0.09  459.3-109.4  0.30  0.72   -161.63    472.18   497.1   -80.0
230  0.72-0.10  471.2-109.3  0.29  0.73   -161.02    483.71   509.5   -77.5
235  0.73-0.10  483.5-109.0  0.29  0.74   -160.38    495.68   522.4   -74.8
240  0.74-0.10  496.4-108.5  0.28  0.74   -159.71    508.12   535.8   -71.8
245  0.74-0.10  509.8-107.6  0.28  0.75   -159.00    521.06   549.8   -68.5
250  0.75-0.10  523.8-106.5  0.27  0.75   -158.25    534.55   564.3   -64.8
255  0.75-0.10  538.5-105.1  0.27  0.76   -157.46    548.62   579.5   -60.7
260  0.76-0.10  553.8-103.2  0.26  0.77   -156.63    563.32   595.3   -56.1
265  0.77-0.10  569.8-101.0  0.25  0.78   -155.74    578.70   611.9   -51.0
270  0.78-0.11  586.7  -98.2  0.25  0.78   -154.80    594.82   629.2   -45.3
275  0.78-0.11  604.4  -94.8  0.24  0.79   -153.80    611.74   647.4   -39.0
280  0.79-0.11  623.0  -90.7  0.24  0.80   -152.73    629.53   666.4   -31.8
285  0.80-0.11  642.6  -85.8  0.23  0.81   -151.58    648.28   686.5   -23.8
290  0.81-0.11  663.3  -80.1  0.22  0.81   -150.36    668.08   707.6   -14.8
295  0.82-0.11  685.1  -73.2  0.22  0.82   -149.04    689.04   729.9    -4.6
300  0.82-0.11  708.3  -65.2  0.21  0.83   -147.62    711.28   753.4     7.0
305  0.83-0.11  732.8  -55.6  0.20  0.84   -146.08    734.95   778.2    20.2
310  0.84-0.11  758.9  -44.3  0.19  0.85   -144.40    760.22   804.6    35.2
315  0.85-0.11  786.7  -30.9  0.19  0.86   -142.58    787.28   832.5    52.5
320  0.86-0.11  816.2  -14.9  0.18  0.87   -140.58    816.37   862.2    72.4
325  0.87-0.11  847.7    4.0  0.17  0.88   -138.37    847.74   893.7    95.5
330  0.88-0.11  881.3   26.7  0.16  0.89   -135.92    881.73   927.2   122.5
335  0.89-0.11  917.1   53.9  0.16  0.90   -133.19    918.72   962.8   154.3
340  0.91-0.11  955.2   86.9  0.15  0.91   -130.13    959.16  1000.5   191.9
345  0.92-0.11  995.5  126.9  0.14  0.92   -126.65   1003.58  1040.3   236.8
```

```
 M    X    Y      VX      VY    R1    R2   THETA      VR     VXTOT  VYTOT
-----------------------------------------------------------------------------

350 0.93-0.111037.8 176.0 0.13 0.94   -122.67   1052.63 1081.9   291.0
355 0.94-0.111081.4 236.6 0.12 0.95   -118.08   1107.02 1124.5   356.8
360 0.96-0.101125.1 311.9 0.11 0.96   -112.71   1167.51 1166.7   437.7
365 0.97-0.101166.1 406.2 0.10 0.98   -106.36   1234.84 1206.0   537.7
370 0.99-0.091199.7 524.6 0.09 0.99    -98.76   1309.41 1237.3   662.0
375 1.00-0.091217.3 672.4 0.09 1.00    -89.56   1390.72 1251.9   815.9
380 1.02-0.081204.6 853.3 0.08 1.02    -78.37   1476.19 1235.4  1002.8
385 1.03-0.061140.41063.4 0.07 1.03    -64.82   1559.25 1166.4  1218.8
390 1.04-0.051001.71282.8 0.07 1.04    -48.81   1627.52 1021.8  1443.6
395 1.05-0.03 779.81470.6 0.06 1.06    -30.89   1664.54  793.1  1635.9
400 1.06-0.01 500.61581.0 0.06 1.06    -12.37   1658.34  506.1  1749.5
405 1.07 0.01 217.41596.4 0.07 1.07      5.12   1611.09  214.9  1766.7
410 1.07 0.03 -24.11537.0 0.07 1.07     20.47   1537.18  -34.4  1707.8
415 1.07 0.04-207.31437.6 0.08 1.07     33.34   1452.47 -225.1  1607.8
420 1.06 0.06-337.11325.5 0.09 1.07     43.93   1367.67 -361.7  1494.3
425 1.06 0.08-425.51215.7 0.10 1.06     52.65   1288.02 -456.5  1382.6
430 1.05 0.09-484.31114.7 0.11 1.06     59.87   1215.37 -521.1  1279.3
435 1.05 0.10-522.31024.4 0.11 1.05     65.91   1149.87 -564.4  1186.5
440 1.04 0.12-545.9 944.6 0.12 1.05     71.04   1091.00 -593.0  1104.0
445 1.03 0.13-559.6 874.2 0.13 1.04     75.44   1037.99 -611.2  1030.8
450 1.03 0.14-566.3 812.1 0.14 1.04     79.26    990.09 -622.1   965.9
455 1.02 0.15-568.1 757.2 0.15 1.03     82.61    946.59 -627.8   908.2
460 1.01 0.16-566.3 708.3 0.16 1.02     85.57    906.89 -629.7   856.5
465 1.01 0.17-562.1 664.7 0.17 1.02     88.21    870.49 -628.9   810.0
470 1.00 0.17-556.1 625.5 0.17 1.01     90.58    836.95 -626.2   768.0
475 0.99 0.18-548.8 590.2 0.18 1.01     92.72    805.90 -621.9   729.9
480 0.98 0.19-540.6 558.1 0.19 1.00     94.66    777.04 -616.6   695.1
485 0.98 0.20-531.9 529.0 0.20 1.00     96.43    750.11 -610.5   663.3
490 0.97 0.20-522.6 502.3 0.20 0.99     98.06    724.89 -603.9   634.0
495 0.97 0.21-513.2 477.8 0.21 0.99     99.56    701.19 -596.9   606.9
500 0.96 0.21-503.5 455.3 0.22 0.98    100.95    678.85 -589.6   581.8
505 0.95 0.22-493.8 434.4 0.22 0.98    102.23    657.74 -582.1   558.5
510 0.95 0.22-484.1 415.1 0.23 0.97    103.43    637.73 -574.5   536.7
515 0.94 0.23-474.5 397.1 0.24 0.97    104.54    618.73 -566.9   516.3
520 0.93 0.23-464.9 380.3 0.24 0.96    105.59    600.63 -559.3   497.2
525 0.93 0.24-455.4 364.6 0.25 0.96    106.57    583.36 -551.6   479.2
530 0.92 0.24-446.0 349.8 0.26 0.95    107.49    566.86 -544.0   462.2
535 0.92 0.25-436.8 336.0 0.26 0.95    108.35    551.05 -536.5   446.1
540 0.91 0.25-427.7 322.9 0.27 0.95    109.17    535.89 -529.1   430.8
545 0.91 0.26-418.8 310.5 0.27 0.94    109.95    521.32 -521.7   416.3
550 0.90 0.26-410.0 298.8 0.28 0.94    110.68    507.30 -514.5   402.5
555 0.90 0.26-401.4 287.6 0.28 0.93    111.37    493.79 -507.3   389.4
560 0.89 0.27-392.9 277.0 0.29 0.93    112.03    480.75 -500.3   376.8
565 0.89 0.27-384.6 266.9 0.29 0.93    112.66    468.16 -493.3   364.7
570 0.88 0.27-376.5 257.3 0.30 0.92    113.26    455.98 -486.5   353.2
575 0.88 0.28-368.5 248.0 0.30 0.92    113.83    444.18 -479.8   342.1
580 0.87 0.28-360.7 239.1 0.31 0.92    114.38    432.75 -473.2   331.4
585 0.87 0.28-353.0 230.6 0.31 0.91    114.90    421.67 -466.7   321.1
590 0.86 0.28-345.5 222.4 0.32 0.91    115.40    410.90 -460.3   311.1
595 0.86 0.29-338.1 214.5 0.32 0.91    115.87    400.43 -454.0   301.5
600 0.86 0.29-330.9 206.9 0.32 0.90    116.33    390.25 -447.8   292.3
605 0.85 0.29-323.8 199.6 0.33 0.90    116.77    380.34 -441.8   283.2
610 0.85 0.30-316.8 192.4 0.33 0.90    117.20    370.69 -435.8   274.5
615 0.84 0.30-310.0 185.5 0.34 0.90    117.60    361.28 -429.9   266.0
```

```
 M    X    Y       VX       VY    R1    R2    THETA      VR     VXTOT   VYTOT
-------------------------------------------------------------------------


620 0.84 0.30-303.3 178.8 0.34 0.89    118.00    352.10 -424.1   257.8
625 0.84 0.30-296.8 172.3 0.34 0.89    118.38    343.15 -418.5   249.8
630 0.83 0.30-290.3 165.9 0.35 0.89    118.74    334.40 -412.9   242.0
635 0.83 0.31-284.0 159.8 0.35 0.88    119.09    325.85 -407.4   234.3
640 0.83 0.31-277.8 153.7 0.35 0.88    119.43    317.49 -401.9   226.9
645 0.82 0.31-271.7 147.8 0.36 0.88    119.76    309.32 -396.6   219.6
650 0.82 0.31-265.7 142.0 0.36 0.88    120.08    301.32 -391.4   212.5
655 0.82 0.31-259.9 136.4 0.36 0.87    120.39    293.49 -386.2   205.5
660 0.81 0.32-254.1 130.9 0.37 0.87    120.69    285.83 -381.1   198.7
665 0.81 0.32-248.5 125.4 0.37 0.87    120.98    278.32 -376.1   192.0
670 0.81 0.32-242.9 120.1 0.37 0.87    121.26    270.97 -371.1   185.5
675 0.80 0.32-237.4 114.8 0.38 0.87    121.53    263.76 -366.3   179.0
680 0.80 0.32-232.1 109.7 0.38 0.86    121.80    256.69 -361.5   172.7
685 0.80 0.32-226.8 104.6 0.38 0.86    122.06    249.76 -356.7   166.4
690 0.80 0.32-221.6  99.6 0.38 0.86    122.31    242.97 -352.1   160.3
695 0.79 0.32-216.5  94.6 0.39 0.86    122.56    236.31 -347.5   154.2
700 0.79 0.33-211.5  89.7 0.39 0.85    122.79    229.78 -342.9   148.3


  M    X    Y       VX       VY    R1    R2    THETA      VR     VXTOT   VYTOT
-------------------------------------------------------------------------


705 0.79 0.33-206.6  84.9 0.39 0.85    123.03    223.38 -338.4   142.4
710 0.78 0.33-201.8  80.1 0.39 0.85    123.26    217.10 -334.0   136.6
715 0.78 0.33-197.0  75.4 0.39 0.85    123.48    210.95 -329.6   130.9
720 0.78 0.33-192.3  70.7 0.40 0.85    123.70    204.92 -325.3   125.2
725 0.78 0.33-187.7  66.0 0.40 0.85    123.91    199.01 -321.1   119.6
730 0.78 0.33-183.2  61.4 0.40 0.84    124.12    193.23 -316.8   114.1
735 0.77 0.33-178.8  56.8 0.40 0.84    124.33    187.57 -312.7   108.6
740 0.77 0.33-174.4  52.3 0.40 0.84    124.53    182.04 -308.6   103.1
745 0.77 0.33-170.1  47.8 0.41 0.84    124.73    176.63 -304.5    97.8
750 0.77 0.33-165.8  43.3 0.41 0.84    124.93    171.35 -300.5    92.4
755 0.76 0.33-161.6  38.8 0.41 0.83    125.12    166.21 -296.5    87.1
760 0.76 0.34-157.5  34.3 0.41 0.83    125.31    161.20 -292.6    81.9
765 0.76 0.34-153.4  29.9 0.41 0.83    125.50    156.33 -288.7    76.7
770 0.76 0.34-149.5  25.5 0.41 0.83    125.68    151.60 -284.8    71.5
775 0.76 0.34-145.5  21.0 0.41 0.83    125.86    147.03 -281.0    66.3
780 0.76 0.34-141.6  16.6 0.42 0.83    126.04    142.62 -277.2    61.2
785 0.75 0.34-137.8  12.2 0.42 0.83    126.22    138.37 -273.5    56.1
790 0.75 0.34-134.1   7.9 0.42 0.82    126.40    134.29 -269.8    51.0
795 0.75 0.34-130.4   3.5 0.42 0.82    126.57    130.40 -266.1    46.0
800 0.75 0.34-126.7  -0.9 0.42 0.82    126.74    126.70 -262.4    41.0
805 0.75 0.34-123.1  -5.3 0.42 0.82    126.92    123.21 -258.8    36.0
810 0.75 0.34-119.5  -9.7 0.42 0.82    127.09    119.93 -255.2    31.0
815 0.74 0.34-116.0 -14.1 0.42 0.82    127.26    116.88 -251.7    26.0
820 0.74 0.34-112.6 -18.4 0.42 0.82    127.43    114.08 -248.1    21.0
825 0.74 0.34-109.2 -22.8 0.42 0.81    127.59    111.54 -244.6    16.1
830 0.74 0.34-105.8 -27.2 0.42 0.81    127.76    109.26 -241.1    11.1
835 0.74 0.34-102.5 -31.7 0.43 0.81    127.93    107.27 -237.7     6.2
#5 840 0.74 0.33 -99.2 -36.1 0.43 0.81    128.10    105.57 -234.2     1.3
845 0.74 0.33 -96.0 -40.5 0.43 0.81    128.27    104.17 -230.8    -3.6
850 0.73 0.33 -92.8 -45.0 0.43 0.81    128.43    103.10 -227.4    -8.5
855 0.73 0.33 -89.6 -49.4 0.43 0.81    128.60    102.35 -224.0   -13.5
860 0.73 0.33 -86.5 -53.9 0.43 0.80    128.77    101.92 -220.6   -18.4
```

|  |  |  |  |  |  |  |  |  |  |  |
|---|---|---|---|---|---|---|---|---|---|---|
| 865 | 0.73 | 0.33 | -83.4 | -58.4 | 0.43 | 0.80 | 128.94 | 101.83 | -217.3 | -23.3 |
| 870 | 0.73 | 0.33 | -80.4 | -62.9 | 0.43 | 0.80 | 129.11 | 102.06 | -213.9 | -28.2 |
| 875 | 0.73 | 0.33 | -77.4 | -67.4 | 0.43 | 0.80 | 129.28 | 102.62 | -210.6 | -33.1 |
| 880 | 0.73 | 0.33 | -74.4 | -72.0 | 0.43 | 0.80 | 129.45 | 103.51 | -207.2 | -38.0 |
| 885 | 0.73 | 0.33 | -71.5 | -76.5 | 0.43 | 0.80 | 129.62 | 104.70 | -203.9 | -43.0 |
| 890 | 0.73 | 0.33 | -68.6 | -81.1 | 0.43 | 0.80 | 129.80 | 106.20 | -200.6 | -47.9 |
| 895 | 0.73 | 0.33 | -65.7 | -85.7 | 0.43 | 0.80 | 129.97 | 107.99 | -197.3 | -52.9 |
| 900 | 0.73 | 0.33 | -62.8 | -90.4 | 0.43 | 0.80 | 130.15 | 110.05 | -194.0 | -57.8 |
| 905 | 0.72 | 0.32 | -60.0 | -95.0 | 0.43 | 0.79 | 130.33 | 112.38 | -190.7 | -62.8 |
| 910 | 0.72 | 0.32 | -57.2 | -99.7 | 0.43 | 0.79 | 130.51 | 114.95 | -187.5 | -67.8 |
| 915 | 0.72 | 0.32 | -54.4 | -104.4 | 0.42 | 0.79 | 130.69 | 117.76 | -184.2 | -72.8 |
| 920 | 0.72 | 0.32 | -51.6 | -109.2 | 0.42 | 0.79 | 130.87 | 120.79 | -180.9 | -77.8 |
| 925 | 0.72 | 0.32 | -48.9 | -114.0 | 0.42 | 0.79 | 131.06 | 124.02 | -177.6 | -82.8 |
| 930 | 0.72 | 0.32 | -46.2 | -118.8 | 0.42 | 0.79 | 131.25 | 127.45 | -174.3 | -87.9 |
| 935 | 0.72 | 0.32 | -43.5 | -123.6 | 0.42 | 0.79 | 131.44 | 131.06 | -171.0 | -93.0 |
| 940 | 0.72 | 0.31 | -40.8 | -128.5 | 0.42 | 0.79 | 131.63 | 134.83 | -167.7 | -98.0 |
| 945 | 0.72 | 0.31 | -38.2 | -133.4 | 0.42 | 0.78 | 131.83 | 138.77 | -164.4 | -103.2 |
| 950 | 0.72 | 0.31 | -35.5 | -138.4 | 0.42 | 0.78 | 132.03 | 142.85 | -161.0 | -108.3 |
| 955 | 0.72 | 0.31 | -32.9 | -143.4 | 0.42 | 0.78 | 132.23 | 147.07 | -157.7 | -113.4 |
| 960 | 0.72 | 0.31 | -30.2 | -148.4 | 0.42 | 0.78 | 132.44 | 151.43 | -154.3 | -118.6 |
| 965 | 0.72 | 0.31 | -27.6 | -153.4 | 0.42 | 0.78 | 132.65 | 155.91 | -151.0 | -123.8 |
| 970 | 0.72 | 0.30 | -25.0 | -158.6 | 0.41 | 0.78 | 132.86 | 160.51 | -147.6 | -129.1 |
| 975 | 0.72 | 0.30 | -22.4 | -163.7 | 0.41 | 0.78 | 133.08 | 165.23 | -144.1 | -134.3 |
| 980 | 0.72 | 0.30 | -19.8 | -168.9 | 0.41 | 0.78 | 133.31 | 170.05 | -140.7 | -139.6 |
| 985 | 0.72 | 0.30 | -17.2 | -174.1 | 0.41 | 0.78 | 133.53 | 174.98 | -137.2 | -145.0 |
| 990 | 0.72 | 0.30 | -14.6 | -179.4 | 0.41 | 0.78 | 133.76 | 180.01 | -133.8 | -150.3 |
| 995 | 0.72 | 0.29 | -12.0 | -184.7 | 0.41 | 0.77 | 134.00 | 185.14 | -130.2 | -155.7 |
| 1000 | 0.72 | 0.29 | -9.4 | -190.1 | 0.41 | 0.77 | 134.24 | 190.36 | -126.7 | -161.2 |
| 1005 | 0.72 | 0.29 | -6.7 | -195.6 | 0.40 | 0.77 | 134.49 | 195.68 | -123.1 | -166.6 |
| 1010 | 0.72 | 0.29 | -4.1 | -201.0 | 0.40 | 0.77 | 134.74 | 201.09 | -119.5 | -172.2 |
| 1015 | 0.72 | 0.28 | -1.4 | -206.6 | 0.40 | 0.77 | 135.00 | 206.59 | -115.8 | -177.7 |
| 1020 | 0.72 | 0.28 | 1.2 | -212.2 | 0.40 | 0.77 | 135.26 | 212.18 | -112.1 | -183.3 |
| 1025 | 0.72 | 0.28 | 3.9 | -217.8 | 0.40 | 0.77 | 135.53 | 217.85 | -108.3 | -188.9 |
| 1030 | 0.72 | 0.28 | 6.6 | -223.5 | 0.40 | 0.77 | 135.81 | 223.62 | -104.5 | -194.6 |
| 1035 | 0.72 | 0.27 | 9.4 | -229.3 | 0.39 | 0.77 | 136.09 | 229.48 | -100.6 | -200.3 |
| 1040 | 0.72 | 0.27 | 12.2 | -235.1 | 0.39 | 0.77 | 136.38 | 235.43 | -96.7 | -206.1 |
| 1045 | 0.72 | 0.27 | 15.0 | -241.0 | 0.39 | 0.76 | 136.68 | 241.46 | -92.7 | -211.9 |
| 1050 | 0.72 | 0.26 | 17.8 | -247.0 | 0.39 | 0.76 | 136.98 | 247.59 | -88.6 | -217.8 |
| 1055 | 0.72 | 0.26 | 20.7 | -253.0 | 0.38 | 0.76 | 137.30 | 253.81 | -84.5 | -223.7 |
| 1060 | 0.72 | 0.26 | 23.6 | -259.1 | 0.38 | 0.76 | 137.62 | 260.13 | -80.3 | -229.7 |
| 1065 | 0.72 | 0.25 | 26.6 | -265.2 | 0.38 | 0.76 | 137.95 | 266.54 | -76.0 | -235.7 |
| 1070 | 0.72 | 0.25 | 29.6 | -271.4 | 0.38 | 0.76 | 138.29 | 273.05 | -71.6 | -241.8 |
| 1075 | 0.72 | 0.25 | 32.7 | -277.7 | 0.37 | 0.76 | 138.64 | 279.66 | -67.1 | -247.9 |
| 1080 | 0.72 | 0.24 | 35.9 | -284.1 | 0.37 | 0.76 | 139.00 | 286.37 | -62.5 | -254.1 |
| 1085 | 0.72 | 0.24 | 39.2 | -290.6 | 0.37 | 0.76 | 139.37 | 293.19 | -57.9 | -260.4 |
| 1090 | 0.72 | 0.24 | 42.5 | -297.1 | 0.37 | 0.76 | 139.75 | 300.11 | -53.1 | -266.7 |
| 1095 | 0.72 | 0.23 | 45.9 | -303.7 | 0.36 | 0.76 | 140.14 | 307.15 | -48.2 | -273.1 |
| 1100 | 0.72 | 0.23 | 49.4 | -310.4 | 0.36 | 0.76 | 140.54 | 314.30 | -43.1 | -279.6 |
| 1105 | 0.72 | 0.23 | 53.0 | -317.2 | 0.36 | 0.76 | 140.96 | 321.57 | -38.0 | -286.1 |
| 1110 | 0.72 | 0.22 | 56.7 | -324.0 | 0.36 | 0.76 | 141.39 | 328.96 | -32.7 | -292.7 |
| 1115 | 0.72 | 0.22 | 60.5 | -331.0 | 0.35 | 0.76 | 141.83 | 336.48 | -27.2 | -299.4 |
| 1120 | 0.72 | 0.21 | 64.4 | -338.0 | 0.35 | 0.75 | 142.29 | 344.13 | -21.6 | -306.1 |
| 1125 | 0.72 | 0.21 | 68.5 | -345.2 | 0.35 | 0.75 | 142.76 | 351.91 | -15.8 | -312.9 |
| 1130 | 0.73 | 0.20 | 72.7 | -352.4 | 0.34 | 0.75 | 143.25 | 359.84 | -9.9 | -319.8 |
| 1135 | 0.73 | 0.20 | 77.1 | -359.7 | 0.34 | 0.75 | 143.75 | 367.92 | -3.7 | -326.7 |
| 1140 | 0.73 | 0.20 | 81.7 | -367.2 | 0.34 | 0.75 | 144.27 | 376.15 | 2.7 | -333.8 |
| 1145 | 0.73 | 0.19 | 86.4 | -374.7 | 0.33 | 0.75 | 144.81 | 384.54 | 9.3 | -340.9 |

```
   M    X    Y       VX      VY    R1    R2    THETA      VR     VXTOT  VYTOT
 ----------------------------------------------------------------------------

1150 0.73 0.19  91.3-382.4 0.33 0.75    145.37    393.10    16.1 -348.1
1155 0.73 0.18  96.5-390.1 0.32 0.75    145.95    401.84    23.1 -355.4
1160 0.73 0.18 101.8-397.9 0.32 0.75    146.55    410.76    30.5 -362.7
1165 0.73 0.17 107.4-405.9 0.32 0.75    147.17    419.87    38.1 -370.1
1170 0.73 0.17 113.3-414.0 0.31 0.75    147.82    429.18    46.0 -377.6
1175 0.74 0.16 119.4-422.1 0.31 0.75    148.49    438.70    54.2 -385.2
1180 0.74 0.16 125.9-430.4 0.31 0.75    149.18    448.44    62.8 -392.9
1185 0.74 0.15 132.7-438.8 0.30 0.75    149.91    458.42    71.8 -400.7
1190 0.74 0.15 139.8-447.3 0.30 0.76    150.66    468.64    81.1 -408.5
1195 0.74 0.14 147.3-455.9 0.29 0.76    151.45    479.12    90.9 -416.4
1200 0.74 0.13 155.2-464.6 0.29 0.76    152.27    489.87   101.1 -424.3
1205 0.75 0.13 163.6-473.4 0.28 0.76    153.12    500.91   111.8 -432.3
1210 0.75 0.12 172.4-482.4 0.28 0.76    154.01    512.25   123.0 -440.4
1215 0.75 0.12 181.8-491.4 0.27 0.76    154.94    523.91   134.8 -448.5
1220 0.75 0.11 191.7-500.5 0.27 0.76    155.91    535.92   147.2 -456.7
1225 0.76 0.10 202.2-509.6 0.27 0.76    156.93    548.28   160.3 -464.9
1230 0.76 0.10 213.4-518.8 0.26 0.76    158.00    561.02   174.1 -473.1
1235 0.76 0.09 225.3-528.1 0.26 0.77    159.12    574.18   188.6 -481.2
1240 0.76 0.08 238.0-537.4 0.25 0.77    160.30    587.76   203.9 -489.4
1245 0.77 0.08 251.5-546.7 0.25 0.77    161.54    601.80   220.2 -497.4
1250 0.77 0.07 266.0-556.0 0.24 0.77    162.84    616.33   237.4 -505.4
1255 0.77 0.06 281.4-565.2 0.24 0.78    164.21    631.38   255.6 -513.3
1260 0.78 0.06 298.0-574.3 0.23 0.78    165.66    646.99   275.0 -520.9
1265 0.78 0.05 315.7-583.2 0.22 0.78    167.20    663.18   295.6 -528.3
1270 0.78 0.04 334.7-591.9 0.22 0.79    168.82    680.01   317.6 -535.4
1275 0.79 0.04 355.2-600.3 0.21 0.79    170.54    697.51   341.0 -542.1
1280 0.79 0.03 377.2-608.3 0.21 0.79    172.37    715.73   366.0 -548.2
1285 0.80 0.02 400.8-615.7 0.20 0.80    174.32    734.71   392.8 -553.7
1290 0.80 0.01 426.3-622.5 0.20 0.80    176.40    754.50   421.4 -558.4
1295 0.81 0.00 453.9-628.4 0.19 0.81    178.63    775.16   452.0 -562.1
1300 0.81 0.00 483.6-633.2 0.19 0.81   -178.99    796.72   484.9 -564.6
1305 0.82-0.01 515.6-636.6 0.18 0.82   -176.44    819.25   520.1 -565.5
1310 0.83-0.02 550.2-638.4 0.17 0.83   -173.69    842.77   557.9 -564.6
1315 0.83-0.03 587.5-638.0 0.17 0.84   -170.73    867.33   598.4 -561.4
1320 0.84-0.03 627.7-635.1 0.16 0.84   -167.53    892.94   641.8 -555.4
1325 0.85-0.04 670.9-628.9 0.16 0.85   -164.07    919.61   688.2 -546.0
1330 0.86-0.05 717.2-618.8 0.15 0.86   -160.31    947.29   737.6 -532.4
1335 0.87-0.06 766.5-604.0 0.14 0.87   -156.23    975.91   789.9 -513.9
1340 0.88-0.07 818.7-583.4 0.14 0.88   -151.79   1005.32   845.1 -489.4
1345 0.89-0.07 873.3-556.0 0.13 0.89   -146.96   1035.29   902.5 -457.7
1350 0.90-0.08 929.7-520.5 0.13 0.90   -141.71   1065.46   961.6 -417.7
1355 0.91-0.09 986.6-475.8 0.12 0.92   -136.00   1095.35  1021.0 -368.2
1360 0.92-0.091042.6-420.6 0.12 0.93   -129.82   1124.28  1079.3 -308.0
1365 0.94-0.101095.6-354.3 0.11 0.94   -123.15   1151.42  1134.2 -236.3
1370 0.95-0.101142.8-276.5 0.11 0.96   -116.01   1175.75  1182.9 -152.9
1375 0.97-0.101181.3-188.0 0.11 0.97   -108.45   1196.16  1222.6  -58.6
1380 0.98-0.101208.2 -90.4 0.11 0.99   -100.53   1211.54  1250.2   45.0
1385 1.00-0.101220.8  13.3 0.10 1.00    -92.35   1220.91  1263.1  154.8
1390 1.01-0.101217.8 119.5 0.10 1.02    -84.05   1223.64  1259.7  267.1
1395 1.03-0.101198.8 223.7 0.11 1.03    -75.76   1219.54  1239.9  377.4
1400 1.04-0.101165.2 322.1 0.11 1.05    -67.62   1208.88  1204.9  481.6
1405 1.05-0.091119.2 411.2 0.11 1.06    -59.77   1192.40  1157.1  576.5
1410 1.07-0.091064.1 489.0 0.11 1.07    -52.29   1171.08  1099.7  659.7
1415 1.08-0.081003.0 554.6 0.12 1.08    -45.25   1146.06  1035.9  730.5
```

```
   M    X    Y       VX      VY    R1    R2    THETA      VR     VXTOT  VYTOT
 ------------------------------------------------------------------

1420 1.09-0.07 938.8 607.9 0.12 1.10    -38.68   1118.44   968.8   788.7
1425 1.10-0.07 874.0 650.0 0.12 1.11    -32.60   1089.19   900.9   835.3
1430 1.11-0.06 810.4 681.9 0.13 1.12    -26.99   1059.13   834.0   871.4
1435 1.12-0.05 749.3 705.1 0.13 1.13    -21.83   1028.88   769.4   898.4
1440 1.13-0.04 691.5 720.9 0.14 1.13    -17.09    998.91   708.0   917.9
1445 1.14-0.03 637.3 730.7 0.15 1.14    -12.73    969.54   650.2   931.0
1450 1.15-0.02 586.9 735.5 0.15 1.15     -8.73    940.99   596.1   938.9
1455 1.16-0.01 540.3 736.4 0.16 1.16     -5.04    913.40   545.9   942.6
1460 1.16 0.00 497.4 734.2 0.16 1.16     -1.64    886.83   499.3   943.0
1465 1.17 0.00 457.9 729.5 0.17 1.17      1.51    861.31   456.1   940.7
1470 1.17 0.01 421.7 722.8 0.17 1.17      4.42    836.84   416.3   936.2
1475 1.18 0.02 388.4 714.7 0.18 1.18      7.12    813.40   379.4   930.0
1480 1.18 0.03 357.9 705.3 0.19 1.18      9.63    790.95   345.3   922.6
1485 1.19 0.04 329.8 695.2 0.19 1.19     11.97    769.46   313.8   914.1
1490 1.19 0.05 304.1 684.4 0.20 1.19     14.16    748.87   284.6   904.9
1495 1.20 0.06 280.4 673.1 0.20 1.20     16.21    729.13   257.5   895.1
1500 1.20 0.07 258.5 661.5 0.21 1.20     18.13    710.21   232.3   884.8
1505 1.20 0.07 238.4 649.7 0.21 1.20     19.94    692.05   208.9   874.3
1510 1.20 0.08 219.8 637.8 0.22 1.21     21.64    674.61   187.1   863.5
1515 1.21 0.09 202.7 625.8 0.23 1.21     23.24    657.83   166.8   852.6
1520 1.21 0.10 186.8 613.9 0.23 1.21     24.76    641.69   147.8   841.7
1525 1.21 0.10 172.0 602.1 0.24 1.22     26.19    626.15   130.0   830.7
1530 1.21 0.11 158.3 590.3 0.24 1.22     27.55    611.16   113.3   819.8
1535 1.22 0.12 145.6 578.7 0.25 1.22     28.84    596.70    97.7   808.9
1540 1.22 0.13 133.8 567.2 0.25 1.22     30.07    582.73    83.0   798.1
1545 1.22 0.13 122.8 555.8 0.26 1.23     31.24    569.23    69.2   787.4
1550 1.22 0.14 112.5 544.7 0.26 1.23     32.35    556.17    56.2   776.9
1555 1.22 0.15 102.9 533.7 0.27 1.23     33.42    543.51    43.9   766.4
1560 1.22 0.15  93.9 522.9 0.27 1.23     34.43    531.25    32.2   756.1
1565 1.22 0.16  85.5 512.3 0.28 1.23     35.40    519.36    21.2   745.9
1570 1.23 0.17  77.7 501.8 0.28 1.24     36.33    507.81    10.8   735.9
1575 1.23 0.17  70.3 491.6 0.28 1.24     37.22    496.60     0.9   726.0
1580 1.23 0.18  63.3 481.6 0.29 1.24     38.08    485.70    -8.4   716.3
1585 1.23 0.18  56.8 471.7 0.29 1.24     38.90    475.09   -17.4   706.8
1590 1.23 0.19  50.6 462.0 0.30 1.24     39.69    464.77   -25.9   697.4
1595 1.23 0.20  44.8 452.5 0.30 1.24     40.45    454.71   -34.0   688.1
1600 1.23 0.20  39.3 443.2 0.31 1.25     41.18    444.91   -41.7   679.0
1605 1.23 0.21  34.1 434.0 0.31 1.25     41.88    435.35   -49.1   670.0
1610 1.23 0.21  29.2 425.0 0.31 1.25     42.56    426.02   -56.2   661.2
1615 1.23 0.22  24.5 416.2 0.32 1.25     43.21    416.92   -62.9   652.5
1620 1.23 0.22  20.1 407.5 0.32 1.25     43.85    408.02   -69.4   643.9
1625 1.23 0.23  15.9 399.0 0.32 1.25     44.46    399.33   -75.6   635.5
1630 1.23 0.23  11.9 390.6 0.33 1.25     45.05    390.83   -81.6   627.2
1635 1.23 0.24   8.1 382.4 0.33 1.25     45.62    382.51   -87.3   619.0
1640 1.23 0.24   4.4 374.3 0.33 1.26     46.17    374.37   -92.9   611.0
1645 1.23 0.25   1.0 366.4 0.34 1.26     46.71    366.40   -98.2   603.0
1650 1.23 0.25  -2.4 358.6 0.34 1.26     47.22    358.60  -103.3   595.2
1655 1.23 0.25  -5.5 350.9 0.34 1.26     47.73    350.95  -108.3   587.5
1660 1.23 0.26  -8.6 343.3 0.35 1.26     48.22    343.46  -113.1   579.9
1665 1.23 0.26 -11.5 335.9 0.35 1.26     48.69    336.11  -117.7   572.4
1670 1.23 0.27 -14.3 328.6 0.35 1.26     49.15    328.90  -122.2   565.0
1675 1.23 0.27 -17.0 321.4 0.36 1.26     49.60    321.83  -126.5   557.8
1680 1.23 0.28 -19.6 314.3 0.36 1.26     50.03    314.89  -130.7   550.6
1685 1.23 0.28 -22.2 307.3 0.36 1.26     50.45    308.08  -134.8   543.5
```

```
   M    X    Y      VX      VY    R1    R2    THETA      VR     VXTOT  VYTOT
 ------------------------------------------------------------------------


1690 1.23 0.28 -24.6 300.4 0.37 1.26     50.87    301.40 -138.7   536.5
1695 1.23 0.29 -27.0 293.6 0.37 1.26     51.27    294.83 -142.6   529.5
1700 1.23 0.29 -29.3 286.9 0.37 1.26     51.66    288.38 -146.3   522.7
1705 1.23 0.29 -31.5 280.3 0.37 1.26     52.04    282.05 -150.0   515.9
1710 1.23 0.30 -33.7 273.8 0.38 1.26     52.41    275.83 -153.5   509.2
1715 1.23 0.30 -35.8 267.3 0.38 1.26     52.77    269.72 -157.0   502.6
1720 1.23 0.30 -37.9 261.0 0.38 1.27     53.13    263.72 -160.4   496.1
1725 1.23 0.31 -39.9 254.7 0.38 1.27     53.47    257.82 -163.7   489.6
1730 1.23 0.31 -41.9 248.5 0.38 1.27     53.81    252.03 -167.0   483.2
1735 1.23 0.31 -43.8 242.4 0.39 1.27     54.14    246.34 -170.1   476.9
1740 1.23 0.32 -45.7 236.4 0.39 1.27     54.46    240.74 -173.2   470.7
1745 1.23 0.32 -47.6 230.4 0.39 1.27     54.78    235.25 -176.3   464.4
1750 1.22 0.32 -49.5 224.5 0.39 1.27     55.09    229.86 -179.3   458.3
1755 1.22 0.32 -51.3 218.6 0.39 1.27     55.39    224.57 -182.2   452.2
1760 1.22 0.33 -53.1 212.9 0.40 1.27     55.69    219.38 -185.1   446.2
1765 1.22 0.33 -54.9 207.1 0.40 1.27     55.98    214.29 -187.9   440.2
1770 1.22 0.33 -56.6 201.5 0.40 1.27     56.26    209.29 -190.7   434.2
1775 1.22 0.34 -58.4 195.9 0.40 1.27     56.54    204.40 -193.4   428.3
1780 1.22 0.34 -60.1 190.3 0.40 1.27     56.82    199.61 -196.2   422.5
1785 1.22 0.34 -61.9 184.8 0.40 1.27     57.09    194.92 -198.8   416.7
1790 1.22 0.34 -63.6 179.4 0.41 1.27     57.35    190.33 -201.5   410.9
1795 1.22 0.34 -65.3 174.0 0.41 1.27     57.61    185.85 -204.1   405.2
1800 1.22 0.35 -67.0 168.6 0.41 1.27     57.87    181.48 -206.6   399.5
1805 1.22 0.35 -68.7 163.3 0.41 1.27     58.12    177.22 -209.2   393.9
1810 1.22 0.35 -70.5 158.1 0.41 1.27     58.37    173.07 -211.7   388.3
1815 1.21 0.35 -72.2 152.9 0.41 1.27     58.62    169.04 -214.2   382.7
1820 1.21 0.35 -73.9 147.7 0.41 1.26     58.86    165.14 -216.7   377.2
1825 1.21 0.36 -75.6 142.5 0.42 1.26     59.10    161.36 -219.1   371.7
1830 1.21 0.36 -77.4 137.4 0.42 1.26     59.33    157.71 -221.6   366.2
1835 1.21 0.36 -79.1 132.4 0.42 1.26     59.56    154.20 -224.0   360.7
1840 1.21 0.36 -80.9 127.3 0.42 1.26     59.79    150.83 -226.4   355.3
1845 1.21 0.36 -82.6 122.3 0.42 1.26     60.02    147.61 -228.8   349.8
1850 1.21 0.36 -84.4 117.3 0.42 1.26     60.24    144.55 -231.2   344.5
1855 1.21 0.37 -86.2 112.4 0.42 1.26     60.46    141.65 -233.5   339.1
1860 1.21 0.37 -88.0 107.5 0.42 1.26     60.68    138.91 -235.9   333.7
1865 1.20 0.37 -89.8 102.6 0.42 1.26     60.90    136.36 -238.2   328.4
1870 1.20 0.37 -91.7  97.7 0.42 1.26     61.12    133.99 -240.6   323.1
1875 1.20 0.37 -93.5  92.9 0.42 1.26     61.33    131.81 -242.9   317.8
1880 1.20 0.37 -95.4  88.0 0.42 1.26     61.54    129.83 -245.2   312.5
1885 1.20 0.37 -97.3  83.2 0.42 1.26     61.75    128.06 -247.6   307.2
1890 1.20 0.37 -99.2  78.4 0.42 1.26     61.96    126.50 -249.9   301.9
1895 1.20 0.37-101.2  73.7 0.42 1.26     62.17    125.17 -252.2   296.6
1900 1.20 0.38-103.2  68.9 0.42 1.25     62.38    124.06 -254.6   291.3
1905 1.20 0.38-105.2  64.2 0.42 1.25     62.59    123.19 -256.9   286.1
1910 1.19 0.38-107.2  59.4 0.42 1.25     62.79    122.56 -259.2   280.8
1915 1.19 0.38-109.2  54.7 0.42 1.25     63.00    122.17 -261.6   275.6
1920 1.19 0.38-111.3  50.0 0.42 1.25     63.20    122.02 -263.9   270.3
1925 1.19 0.38-113.4  45.3 0.42 1.25     63.41    122.12 -266.2   265.0
1930 1.19 0.38-115.5  40.6 0.42 1.25     63.61    122.47 -268.6   259.8
1935 1.19 0.38-117.7  35.9 0.42 1.25     63.81    123.06 -270.9   254.5
1940 1.19 0.38-119.9  31.2 0.42 1.25     64.02    123.90 -273.3   249.2
1945 1.18 0.38-122.1  26.5 0.42 1.24     64.22    124.98 -275.7   243.9
1950 1.18 0.38-124.4  21.9 0.42 1.24     64.43    126.30 -278.1   238.6
```

```
     M    X    Y      VX      VY    R1    R2    THETA      VR     VXTOT  VYTOT
   -----------------------------------------------------------------------


   1955 1.18 0.38-126.7  17.2 0.42 1.24     64.63    127.84 -280.4  233.3
   1960 1.18 0.38-129.0  12.5 0.42 1.24     64.84    129.62 -282.8  228.0
   1965 1.18 0.38-131.4   7.8 0.42 1.24     65.04    131.61 -285.3  222.6
#6 1970 1.18 0.38-133.8   3.1 0.42 1.24     65.25    133.81 -287.7  217.2
   1975 1.17 0.38-136.2  -1.6 0.42 1.23     65.46    136.23 -290.1  211.9
   1980 1.17 0.38-138.7  -6.4 0.42 1.23     65.67    138.84 -292.6  206.5
   1985 1.17 0.38-141.2 -11.1 0.42 1.23     65.88    141.64 -295.1  201.0
   1990 1.17 0.38-143.8 -15.8 0.42 1.23     66.09    144.63 -297.5  195.6
   1995 1.17 0.38-146.4 -20.6 0.42 1.23     66.30    147.79 -300.0  190.1
```

```
mass ratio =                    0.55128
inclination angle =            75.50000
white dwarf radius =            0.01100
Roche limit =                   0.56087
rear of secondary =             1.35388
Roche potential =               2.97314
xmax of lobe =                  1.35388
ymax of lobe =                  0.32129
zmax of lobe =                  0.30759
```